SDL/06-182

Revision: A

SOFIE GROUND CALIBRATION REPORT

Revised:
June 2006

Prepared by:

Space Dynamics Laboratory
1695 North Research Park Way
North Logan UT 84341-1947

TABLE OF CONTENTS

LIST OF FIGURES

LIST OF TABLES

1. INTRODUCTION

SOFIE (Solar Occultation for Ice Experiment) is the primary infrared sensor in the AIM suite of instruments. The SOFIE instrument design is based on the highly successful UARS HALOE instrument. SOFIE will perform satellite solar occultation measurements to obtain limb-path broadband transmission profiles, which will be used to determine profiles of temperature/pressure, mixing ratio profiles of five gaseous species (O3, H2O, CO2, CH4, and NO), and polar mesospheric cloud (PMC) particle extinction.

The instrument will use the differential absorption radiometry approach, with eight channel pairs covering wavelengths (λ) from 0.29 to 5.32 μm. In this technique, specific gases are targeted by measuring solar intensity in two wavelength regions, one where the gas is strongly absorbing and an adjacent region where the gas is weakly absorbing. Measuring the difference between the strong and weak band signals has numerous advantages, including the reduction of undesired instrumental effects, and the reduction of atmospheric interference. Six SOFIE channels are designed to measure gaseous signals, and two are dedicated to particle measurements. Measurements in two CO_2 bands will be used to simultaneously retrieve temperature and CO_2 mixing ratio. In addition to the main science channels, SOFIE includes an imaging sun sensor for pointing control.

This document presents results from ground calibration of the SOFIE instrument, to characterize instrument performance and verify instrument requirements. The instrument requirements verified during calibration testing are described in the next section. Later sections describe the parameters to be derived from calibration data, and the equipment used during calibration. Finally, SOFIE calibration data analysis results are described.

2. SOFIE INSTRUMENT REQUIREMENTS

SOFIE instrument requirements describe the performance required to achieve the program science objectives. Ground calibration and characterization of the SOFIE instrument ensures that these levels of performance are achieved, and provides a chance to understand and gain experience with the instrument, before the sensor is placed in orbit. While many SOFIE calibration parameters are planned to be determined from on-orbit measurements, preliminary measurements on the ground were conducted to verify that the instrument requirements are met.

2.1. INSTRUMENT REQUIREMENTS DRIVING CALIBRATION

An important goal of detailed calibration planning is identification of the instrument requirements that drive calibration measurements. A matrix relating planned calibration experiments to relevant instrument requirements is shown in Table 1. The matrix shows a number of instrument requirements identified by paragraph number in the SOFIE Specification and Verification Database [1]. The reader is referred to this document for details of the specific instrument requirements.

Table 1. Calibration Measurements Versus Requirements

		Requirement						
Configuration	**Test Name**	SOF 174, 183, 299 (Spectral Response)	SOF 176, 178, 181 (Scan Capability)	SOF 179, 180, 295, 298 (FOV)	SOF 184, 185 (linearity)	SOF 299 (Stability)	SOF 186, 267 (Dynamic Range)	SOF 203, 231, 233 (Detector Co-Alignment)
MIC1 + FTS	In-Band Relative Spectral Response (RSR)	X				X		
	Out-of-Band RSR	X						
MIC1 + Solar Simulator	Linearity / Sensitivity				X		X	
	Field of view (FOV)		X	X				
	Knife edge			X				X
	Scan Algorithm		X					
	Stability / Repeatability					X		
Direct Solar Observation	Linearity / Sensitivity				X		X	
	Knife edge (detector coalignment)							X
	Stability / Repeatability					X		
	Scan Algorithm		X					

Table 2 shows a similar table relating sun sensor requirements to planned test and qualification plans. A large part of sun sensor requirements verification was accomplished in bench testing

under nitrogen purge during instrument integration. Details can be found in the SOFIE Integration and Test Plan [2]. These tests are indicated in Table 2 by the block of testing labeled Bench Testing (Outside Chamber). Remaining sun sensor testing indicated in Table 2 was accomplished on the assembled and complete system under vacuum during instrument calibration.

Table 2. Sun Sensor Test Plans Versus Requirements

		Requirement		
Configuration	**Test Name**	SOF 176, 178, 181 (Scan Capability)	SOF 233, 300 (Pointing Uncertainty)	SOF 310 (Solar Search Algorithm)
Bench Testing (Outside Chamber)	Preliminary System Pointing Control Test	X	X	X
	System Pointing Control Test	X	X	X
MIC1 + Solar Simulator	Field of view (FOV)		X	
	Knife edge		X	
	Scan Algorithm	X		X
Direct Solar Observation	Knife edge (detector coalignment)		X	
	Scan Algorithm	X		X

For the SOFIE main instrument, the most critical requirement verified during ground calibration is the sensor spectral response. While many other calibration parameters may be determined on orbit, spectral response characterization can only be carried out during ground measurements. The SOFIE spectral bandpass requirements are shown in Table 3 for reference. The SOFIE spectral response is designed to develop 99% of the instrument response within 1.5 filter widths of the filter band center (SOF 174). The filter width is defined as the wavelength separation between 50% transmission points, while the band center wavelength is defined as the average of the 50% points.

Table 3. SOFIE Spectral Band Specifications and Channel S/N Requirements

Band	Center λ (μm)	Band Limits, μm	Band Limits, cm^{-1}	S/N*
O_3 strong	0.290	0.2857 - 0.2941	34000 - 35000	1.0×10^4
O_3 weak	0.328	0.3226 – 0.3333	30000 - 31000	1.0×10^4
particle strong	0.862	0.8475 – 0.8772	11400 - 11800	1.0×10^6
particle weak	1.03	1.0101 – 1.0526	9500 - 9900	1.0×10^6
H_2O weak	2.45	2.427 – 2.475	4040 - 4120	2.5×10^4
H_2O strong	2.60	2.577 – 2.632	3800 - 3880	2.5×10^4
CO_2 strong	2.77	2.740 – 2.794	3580 - 3650	3.0×10^5
CO_2 weak	2.94	2.907 – 2.967	3370 - 3440	3.0×10^5
particle strong	3.06	3.030 – 3.091	3235 - 3300	1.0×10^5
particle weak	3.19	3.160 – 3.226	3100 - 3165	1.0×10^5
CH_4 strong	3.37	3.333 – 3.401	2940 - 3000	4.0×10^5
CH_4 weak	3.51	3.472 – 3.546	2820 - 2880	4.0×10^5
CO_2 strong	4.25	4.255 – 4.444	2250 - 2350	4.0×10^5
CO_2 weak	4.63	4.630 – 4.740	2110 - 2160	4.0×10^5
NO weak	4.98	4.951 – 5.051	1980 - 2020	3.0×10^5
NO strong	5.32	5.263 – 5.376	1860 - 1900	3.0×10^5

The requirement that 99% of the instrument response be developed within 1.5 filter band widths of the band center wavelength places a requirement on the out-of-band response. In order to limit integrated out-of-band response to 1% or less of the in-band response, an average out-of-band relative spectral response (RSR) of 0.01% is required. A requirement has been placed on the SOFIE filters that peak out-of-band transmission be 1% or less. The out-of-band response between out-of-band peaks is expected to be less, resulting in an average out-of-band response of 0.01% or less. Data were collected to characterize in-band and out-of-band RSR during final calibration. RSR data were acquired at nominal, warm, and cold science temperature conditions.

A second critical ground calibration measurement, given the detector non-linearity discovered during preliminary testing, is linearity characterization, including determination of a linearity correction function. Based on preliminary testing results, SOFIE linearity requirements (SOF 184) will only be met after application of a linearity correction function during data processing. Linearity characterization was accomplished using a small attenuator approach that measured the transmittance of an optical window at multiple points in the dynamic range. Changes in the measured transmittance as a function of dynamic range were used to determine a linearity correction.

The remaining instrument parameters listed in Table 1 were also the subject of ground calibration experiments, although on-orbit characterization is planned as well. Ground characterization of these parameters ensures that the sensor performs as designed, and reduces the risk of unex-

pected problems after launch. It is the standard practice of SDL to perform as much ground characterization and testing of a sensor as possible before delivery to the customer. Ground calibration experiments included characterization of spatial, temporal, and absolute radiometric response, in addition to the spectral and linearity response characterization already discussed.

SOFIE instrument spatial response characterization included field-of-view (FOV) characterization over a range of 32 arcmin, or ±16 arcmin from the vertical FOV center (SOF 298). In addition, detector co-alignment was verified. FOV characterization tests were performed using the MIC1 collimator steering mirror to move a point source across the focal plane. Detector co-alignment verification was accomplished using a knife edge source moved across the instrument focal plane, while observing the MIC1 collimator.

Temporal characterization must demonstrate instrument stability within the time frame of a solar occultation measurement. This time is specified as 30 seconds in the SOFIE requirements (SOF 299). These tests were performed while observing a high temperature blackbody. Scan algorithm functionality was verified during direct solar observations are planned as well.

Absolute radiometric response characterization demonstrated the SOFIE dynamic range and sensitivity requirements (SOF 186, 267). Absolute radiometric response characterization was performed using the MIC1 collimator, in combination with a solar emulator blackbody at a number of blackbody temperatures.

Summary test plans for each calibration experiment are included in the SOFIE Ground Calibration Plan [3]. Complete detailed test plans are developed in separate documents identified in the calibration plan.

3. SOFIE CALIBRATION PARAMETERS AND UNCERTAINTY

A necessary step in the calibration process is to identify those parameters which completely characterize the sensor. These equations and associated parameters can be conveniently grouped into two categories: calibration equation parameters and radiometric model parameters. The calibration equation contains parameters that are needed to relate sensor output to measured flux in engineering units such as watts/cm^2·sr. The measured flux is related to the true scene flux using calibration parameters from the radiometric model. The radiometric model contains those calibration parameters that are not part of the calibration equation, but that are needed to completely characterize the sensor. Together, the calibration equation and radiometric model parameters describe the responsivity of the sensor, including spatial, spectral, and temporal response characteristics.

3.1. CALIBRATION PARAMETERS

SOFIE is designed to measure atmospheric transmission profiles using differential absorption radiometry. The differential absorption technique is a relative measurement and as such, no absolute radiometric calibration is required. However, absolute radiometric calibration was essentially performed to verify instrument design and performance. This design approach is reflected in the calibration equation and radiometric model parameters.

3.1.1. Calibration Equation

The SOFIE instrument operates by processing the signal from each band in a differential absorption pair to yield a direct signal from each band, and a difference signal for the pair. These signals are converted to digital outputs proportional to volts for further processing. The direct signal output from a given detector will be used for most ground calibration measurements. For a given detector, the calibration equation for the direct signal output is given by

$$N_d = \ell\left(\mathbb{C}_{ADC}\left(G_d\left(r_d\right)\right)\right) \tag{1}$$

where the parameters are as identified in Table 4.

Table 4. Direct Response Calibration Equation Parameters

Parameter	Symbol
Digitized detector response [counts]	N_d
Linearity correction function	ℓ
ADC coefficient [counts per volt]	$\mathbb{C}_{ADC}$
Electronics gain [unitless]	G_d
Detector response [volts]	r_d
Detector index - parameter is unique to each detector	d

The calibration equation for the difference signal from a differential absorption detector pair is given by

$$N_{diff} = \mathbb{C}_{ADC} G_{diff} \left(G_w \left(r_w \right) - G_s \left(r_s \right) \right) \tag{2}$$

where the parameters are as identified in Table 5.

Table 5. Differential Response Calibration Equation Parameters

Parameter	Symbol
Digitized differential response [counts]	N_{diff}
ADC coefficient [counts per volt]	$\mathbb{C}_{ADC}$
Differential gain [unitless]	G_{diff}
Weakly absorbing channel adjustable gain [unitless]	G_w
Weakly absorbing preamplified response [volts]	r_w
Strongly absorbing channel adjustable gain [unitless]	G_s
Strongly absorbing preamplified response [volts]	r_s

The difference signal described by Equation (2) is produced in the instrument itself, eliminating the possibility of linearity correction, and as such no linearity correction function is shown in the equation. Analysis of the system performance, including expected non-linearity remaining in the modified instrument, predicts acceptable difference signal performance [4]. Difference signal

analysis using linearity corrected data may be performed in data processing following data collection, using the corrected data described in Equation (1).

3.1.2. Radiometric Model

The SOFIE radiometric model characterizes the spectral, spatial, and temporal responsivity domains of the sensor. The spectral domain will be characterized by the in-band and out-of-band relative spectral response. The spatial domain will be characterized by the detector field of view and detector co-alignment. The temporal domain will be characterized by the sensor response stability and repeatability. The calibration parameters included in the radiometric model are listed in Table 6.

Table 6. Radiometer Radiometric Model Calibration Parameters

Parameter	Symbol
Relative spectral responsivity	$RSR(\lambda_d)$
Effective field of view	Ωeff_d
Detector coalignment	$\Delta\theta_d$
Illuminated short-term repeatability (noise)	σ_{st}
Illuminated short-term stability (drift)	σ_{mt}

3.2. MEASUREMENT UNCERTAINTIES

A complete calibration includes estimates of measurement uncertainties. The approach is to generate a list of uncertainties and descriptions of their applicability to a particular measurement objective.

When possible, the recommended terminology and practices of the National Institute of Standards (NIST) will be followed in expressing uncertainties [5]. These recommendations include reporting all uncertainties as standard uncertainties (i.e. one standard deviation) and combining uncorrelated uncertainties using the square root of the sum of the squares (RSS) of the individual standard uncertainties.

4. SOFIE CALIBRATION EQUIPMENT

SOFIE calibration source configurations were described in detail in the SOFIE calibration plan [3]. Information from this document is reproduced and summarized here for reference.

4.1. CALIBRATION CHAMBER

The SOFIE instrument was operated in a vacuum chamber to simulate the space environment during calibration. A photograph of the SOFIE calibration chamber is shown in Figure 1. A conceptual drawing of the SOFIE instrument installed in the test chamber is shown in Figure 2. Important thermal control features are identified in this drawing as well.

Figure 1. SOFIE Test Chamber

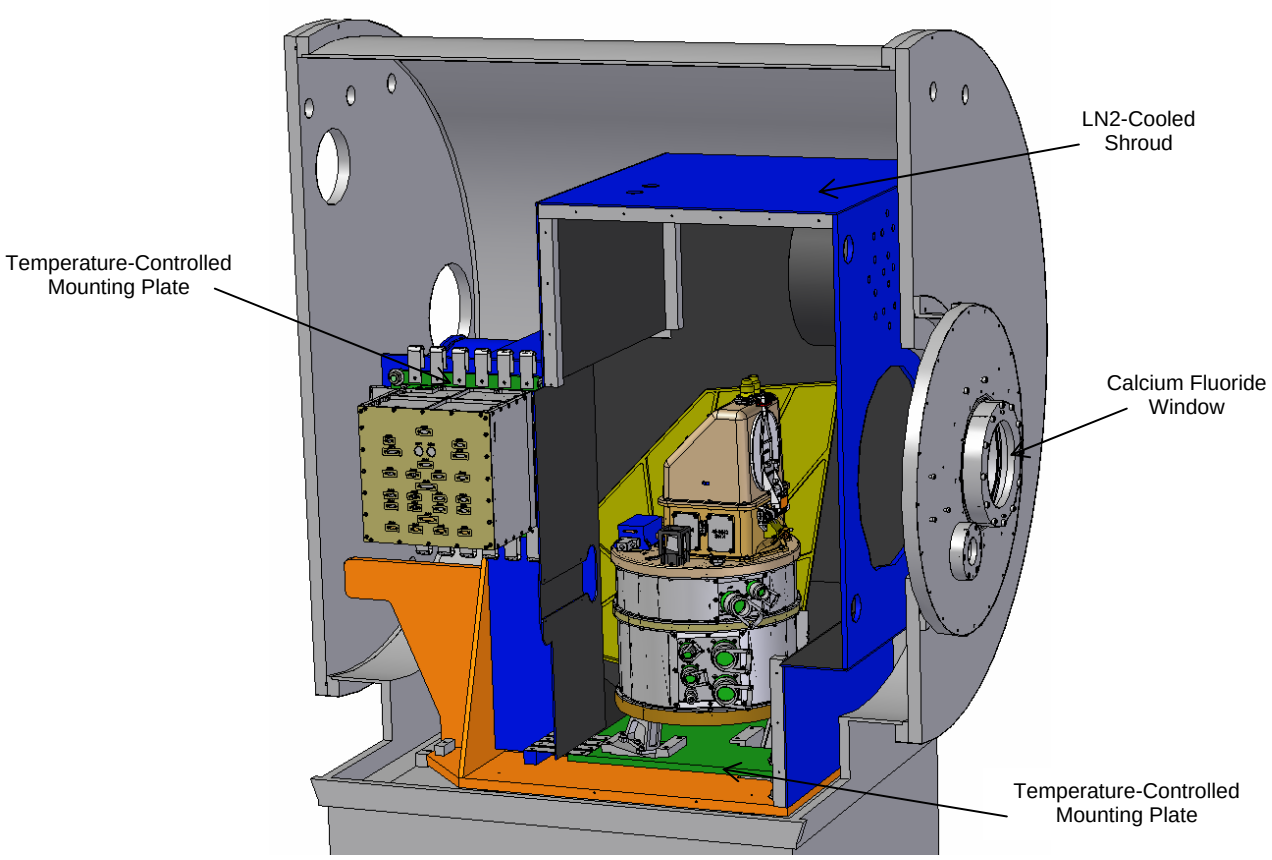

Figure 2. SOFIE Calibration Thermal Environment

The drawing also shows the CaF_2 window through which calibration measurements were performed.

4.2. HELIOSTAT

A Meade LX200 telescope tracking mount was used to maintain sun alignment during direct solar observations. Custom software written by SDL controls the tracking stage. A 12" diameter commercial grade front surface mirror was placed on the mount, and a second mirror relayed the reflection from the first mirror into the SOFIE test chamber. A conceptual drawing of the heliostat system is shown in Figure 3. A photograph of the heliostat system in operation during SOFIE calibration is shown in Figure 4.

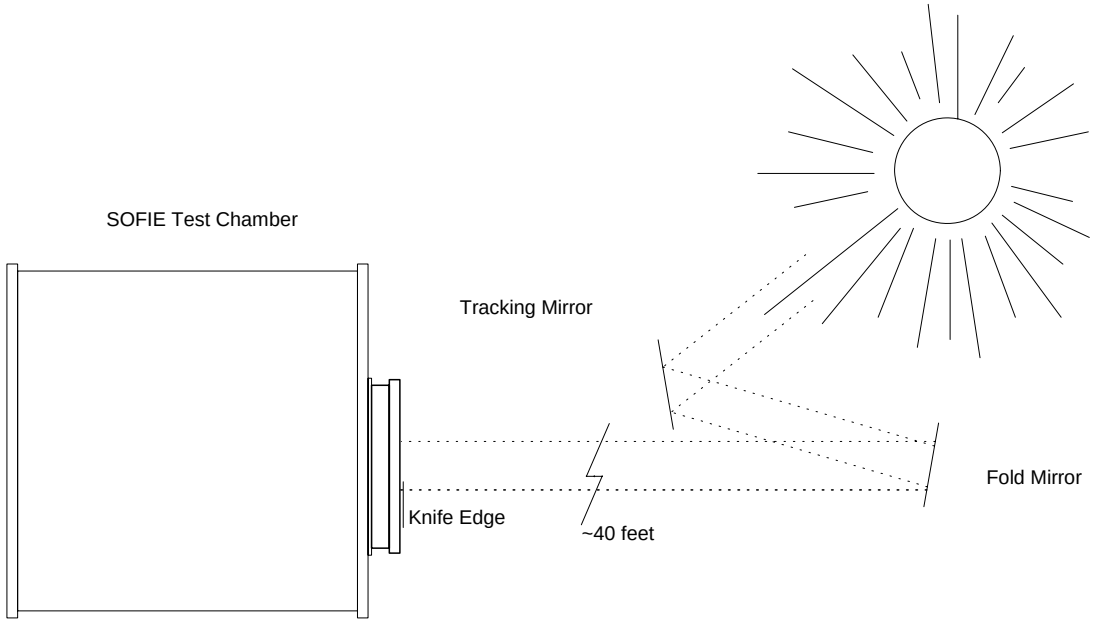

Figure 3. Heliostat Concept

Figure 4. Heliostat in Operation

4.3. MULTIFUNCTION CALIBRATOR

For all spectral testing, and for most radiometric, spatial and temporal domain testing, the SOFIE instrument observed the MIC1 collimator. This collimator provides a 100 inch long focal length collimator with interchangeable apertures. A flat pointing mirror provides beam steering capability over 10 degrees in two axes. External sources are focused into the collimator to generate the output beam. These sources include a high temperature blackbody and Fourier Transform Spectrometer (FTS).

A photograph of the MIC1 collimator is shown in Figure 5. Important MIC1 specifications are compiled in Table 7. MIC1 collimator apertures are described in Table 8.

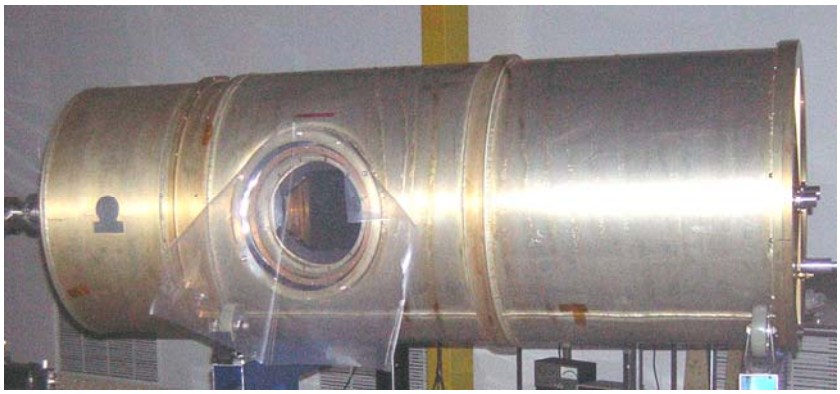

Figure 5. MIC1 Collimator

Table 7. MIC1 Collimator Specifications

Focal Length	100 inches
Exit Aperture Geometry	6 inches diameter, circular
Pointing Mirror Full-scale travel (2 dimensions) Resolution Accuracy	 10 degrees 4.1 μrad (0.9 arcsec) ±20.5 μrad (4.23 arcsec)

Table 8. MIC1 Collimator Apertures

Position	Diameter	Divergence
0	Open	Open
1	0.0079 in.	0.079 mrad (0.27 arcmin)
2	0.0111 in.	0.111 mrad (0.38 arcmin)
3	0.0158 in.	0.158 mrad (0.54 arcmin)
4	0.0224 in.	0.224 mrad (0.77 arcmin)
5	0.0316 in.	0.316 mrad (1.08 arcmin)
6	0.0447 in.	0.447 mrad (1.54 arcmin)
7	0.0633 in.	0.633 mrad (2.18 arcmin)
8	0.0895 in.	0.895 mrad (3.08 arcmin)
9	0.127 in.	1.27 mrad (4.37 arcmin)
10	0.179 in.	1.79 mrad (6.15 arcmin)
11	0.253 in.	2.53 mrad (8.70 arcmin)
12	Open	Open
13	Rectangle	0.265 in. X 0.175 in. (9.11 amin X 6.02 amin)

4.3.1. Fourier Transform Spectrometer

A Fourier Transform Spectrometer (FTS) was used with MIC1 to provide a source for SOFIE spectral calibration. A photograph of this instrument is shown in Figure 6. The FTS was placed at the MIC1 input, and a CaF_2 lens was used to focus the FTS output onto the MIC1 aperture. A conceptual drawing of this configuration is shown in Figure 7.

The MIC1 spectral calibration configuration was characterized separately from SOFIE calibration to determine the relative spectral content of the MIC1 output. This measurement is based on spectral calibration of large-area spectral reference detectors and forms the basis for SOFIE relative spectral response calibration.

Figure 6. Digilab FTS6000 Fourier Transform Spectrometer

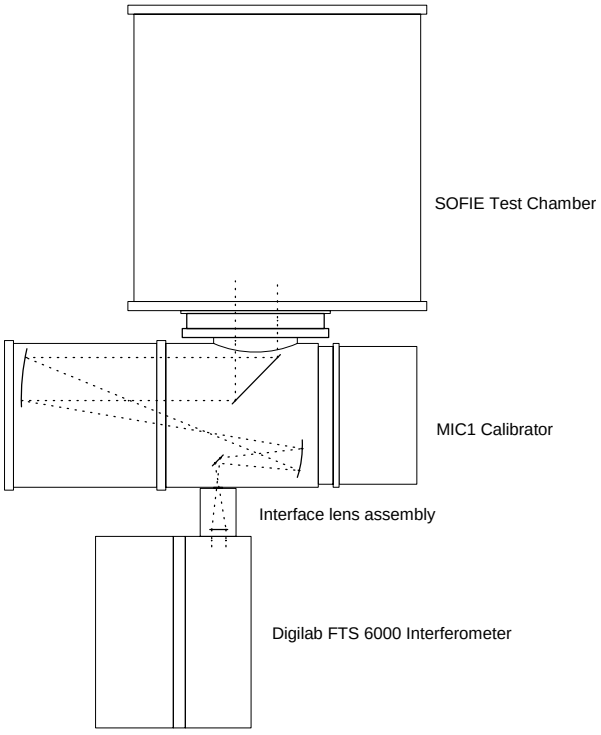

Figure 7. Relative Spectral Response Characterization Concept

4.3.1.1. Spectral Reference Detectors

Relative Spectral Response characterization requires knowledge of the relative spectral content of the MIC1 output when the FTS source is used. This knowledge is obtained from detectors

having a known relative spectral response. For IR wavelengths longer than approximately 1 micron, a large (0.5 inch square) pyroelectric detector is used. The pyroelectric element of this detector has been painted with Z306 black paint to achieve a highly absorbing and stable surface. A photograph of the detector element is shown in Figure 8.

The relative spectral response of the IR spectral reference detector (SRD) is determined from witness sample reflectance measurements, performed by Surface Optics Corporation. These measurements were first performed in 1998, and have been repeated with consistent results as recently as August 2004.

For wavelengths shorter than approximately 1.1 micron, a silicon photodiode is used. A photograph of this detector is shown in Figure 9. Spectral response information for this detector was provided by calibration at the NIST. Specifications for both spectral reference detectors are listed in Table 9.

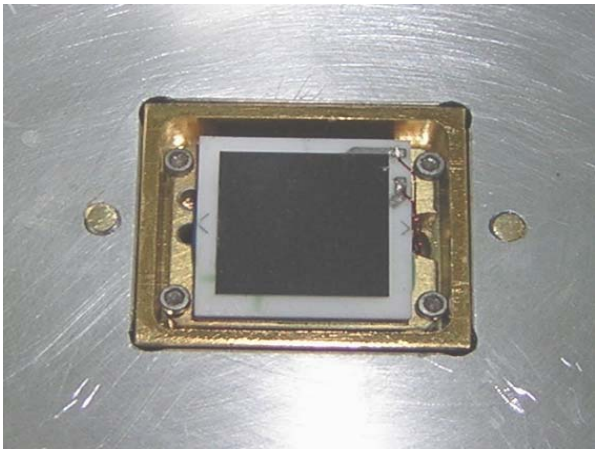

Figure 8. IR Spectral Reference Detector

Figure 9. UV-Visible Spectral Reference Detector

Table 9. Spectral Reference Detectors

Detector	Wavelength Range	Model	Dimensions	Spectral Calibration
IR	0.7 – 25 μm	Servo Corp. 1550	0.5 inch square	Witness sample directional reflectance, SOC 2004 [6]
UV-Visible	0.2 – 1.1 μm	Hamamatsu S2881	11.3 mm round	Comparison to working standards, NIST 2004 [7]

4.3.2. Solar Simulator Blackbody

For radiometric, spatial and temporal domain test during SOFIE calibration, a high temperature blackbody was placed at the input to MIC1, and a CaF_2 lens focused the blackbody output onto the MIC1 aperture. The MIC1 steering mirror provided movement of the source throughout the SOFIE field of view. The solar simulator blackbody provided temperatures up to 3000 K.

A photograph of the solar simulator blackbody is shown in Figure 10. A conceptual drawing of the MIC1 with SEBB configuration is shown in

Figure 11.

Figure 10. Electro-Optical Industries 156A Blackbody

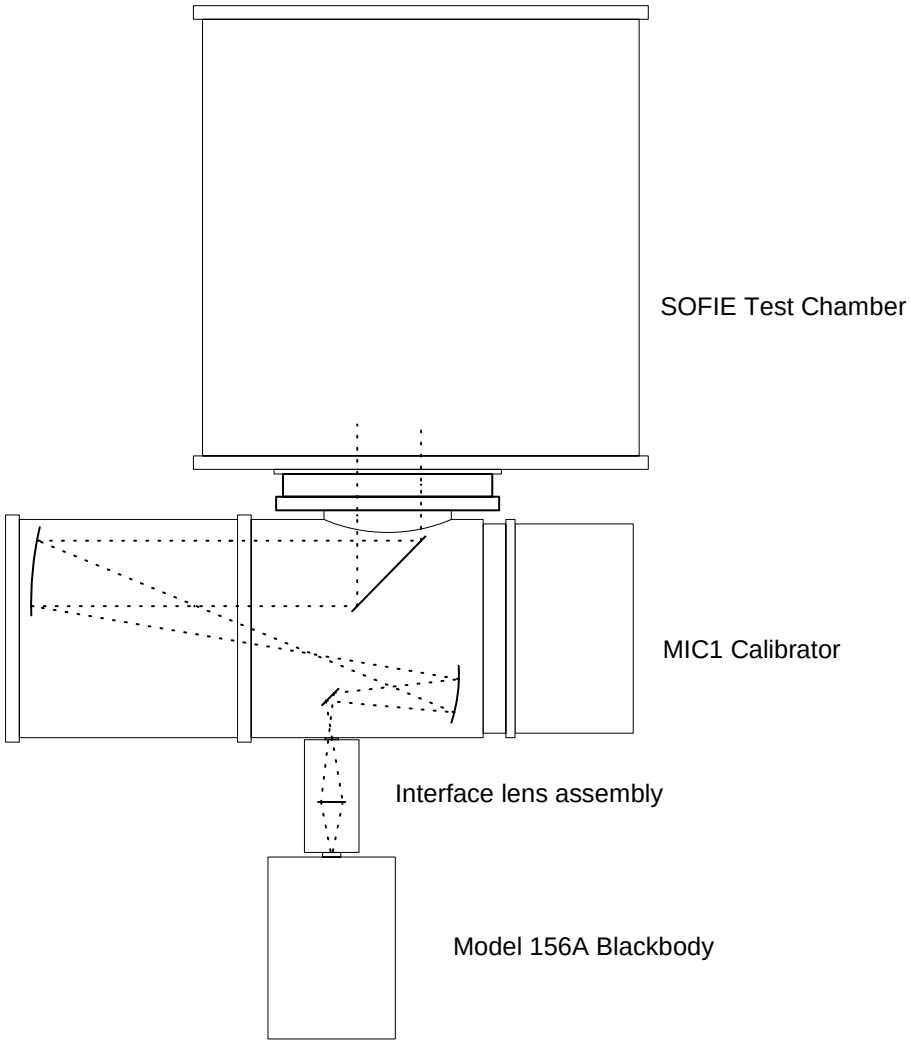

Figure 11. MIC1 with SEBB configuration

5. SOFIE CALIBRATION DATA ANALYSIS RESULTS

Calibration experiments were conducted to provide data needed for calculation of the parameters included in the calibration equation and radiometric model described in Section **3**. These tests were performed at different temperature conditions to cover the expected on-orbit operational envelope [2].

5.1.1. Relative Spectral Response Characterization

The relative spectral responsivity (RSR) of a sensor is the peak-normalized responsivity at different wavelengths both inside and outside the passband of nominal response. The RSR is used to calculate passband dependant radiance and to verify the spectral response instrument requirement.

SOFIE RSR measurements were made using a Digilab model FTS6000 step-scan Fourier Transform Spectrometer (FTS). For SOFIE bands at wavelengths longer than 0.63 μm, the output of the FTS was focused into the MIC1 entrance aperture using a CaF_2 lens. A conceptual drawing of the MIC1 RSR calibration configuration is shown in Figure 7. The FTS was placed on an adjustable mechanical table and positioned at the entrance port of the MIC1 collimator. The mechanical table supporting the FTS was translated horizontally and vertically to maximize the signal on the detector. This adjustment was followed by angular adjustments of the FTS table to center the signal on the detector. These steps were iterated until no further improvement in signal could be achieved. This FTS position alignment procedure is intended to establish a repeatable and consistent configuration to prevent errors in FTS spectral flux caused by FTS beam spatial non-uniformity, as well as avoid spectral wavelength scale errors, which occur when the observed radiation passes through the interferometer at an angle to the optical axis. No MIC1 aperture was used. For SOFIE bands at wavelengths shorter than 0.63 μm, the FTS output was introduced directly into the SOFIE instrument, to avoid the attenuation introduced by the gold mirrors in MIC1.

The FTS provided an interference-modulated source at the MIC1 output that was sampled by the sensor to generate interferograms from which spectral information was derived. A glowbar source and KBr beamsplitter were used in the FTS to provide wavelength coverage from 2 to 6 μm, while a tungsten-halogen lamp and quartz beamsplitter were used for wavelengths between 0.63 and 2 μm. A Xenon arc lamp was and quartz beamsplitter were used for wavelengths below 0.63 μm. A nitrogen gas purge was maintained in the FTS and MIC1 during all RSR measurements.

The FTS was operated in 1 Hz step scan mode (1 step/second) for all RSR measurements. The FTS spectral resolution used for in-band RSR measurements was 4 cm^{-1} for wavelengths between 2 and 6 μm, 8 cm^{-1} for wavelengths between 0.63 and 2 μm, and 32 cm^{-1} for wavelengths less than 0.63 μm. For out-of-band RSR measurements, FTS spectral resolution was 16 cm^{-1} for wavelengths between 2 and 6 μm, and 32 cm^{-1} for wavelengths less than 2 μm. For wavelengths less than 0.63 μm, out-of-band blocking measurements were limited by low signal to 1% of in-band peak, therefore out-of-band data in these regions was based on filter vendor component measurements.

SOFIE in-band RSR measurements were made for each individual spectral band at cold, nominal, and warm science operating temperature cases. The SOFIE pointing mirror was fixed at nominal orientation. Out-of-band RSR data were collected at nominal operating temperature only. RSR data were collected simultaneously on all bands under test.

Interferograms recorded during RSR tests were converted into spectra using SDL FTS software. This processing included offset correction of the interferogram, multiplication by a Kaiser-Bessel apodization function that gives a spectral sidelobe attenuation of 1e-5, zero padding to give a power-of-2 number of data points, Fourier transformation into real spectra, normalization by the sample interval in cm, and position rotation. These spectra were then divided by the relative spectral output of the FTS and MIC1 system to give the relative spectral responsivity of the sensor. The output spectrum of MIC1 using the FTS input source was measured using a separate optical system and pyroelectric spectral reference detector mounted in a vacuum chamber attached to the exit port of MIC1 (see Section 4.3.1.1 and SDL/05-049). This measurement was performed in June 2005. Results of these measurements are described in the following section.

5.1.1.1. MIC1 Exit Beam Spectral Intensity

The relative spectral intensity of the MIC1 exit beam for wavelengths longer than 1 μm was measured using an infrared spectral reference detector (SRD). This detector uses a large (0.5 in. X 0.5 in.) square pyroelectric element coated with Z306 diffuse black paint as a spectral standard. The RSR of the IR spectral reference detector is given by the detector element absorptance, which was determined from total hemispherical reflectance measurements of two detector element witness samples performed in August 1998 and again in August 2004 by Surface Optics Corp. (SOC) (see SOC-R6001-066-001-1098 and SOC-R1446MP-001-0904). For wavelengths below 1.1 μm, a NIST-calibrated Silicon photodiode (Hamamatsu S2281) was used [7].

The output spectrum of the FTS and MIC1 system (MIC1 only for wavelengths below 0.63 μ) measured using the spectral reference detector was divided by the reference detector relative spectral responsivity and reference detector optical system reflectance, to calculate the spectral intensity of the output beam. The calculation to determine the relative spectral intensity of the output beam is shown in Equation (3):

$$S(\bar{\upsilon}) = \frac{S_{FTS}(\bar{\upsilon})}{\tau_{FM}(\bar{\upsilon}) RSR_{RD}(\bar{\upsilon})} \tag{3}$$

where

$S(\bar{\upsilon})$ = relative spectral intensity of the MIC1 exit beam

$S_{FTS}(\bar{\upsilon})$ = mean reference detector measured FTS output spectrum

$\tau_{FM}(\bar{\upsilon})$ = reference detector optical system reflectance

$RSR_{RD}(\bar{\upsilon})$ = reference detector relative spectral responsivity

$\bar{\upsilon}$ = wavenumber (cm^{-1})

The SRD relative spectral responsivity, $RSR_{RD}(\bar{\upsilon})$, was determined from the SOC measurement of the single witness sample that was the best match to the actual reference detector element. This match was determined from separate single-angle reflectance measurements made at SDL

in June 1997, on both witness samples and the reference detector itself. In these measurements, one witness sample showed better agreement with the actual detector element than the other sample. The differences observed in the witness samples in these measurements were of the same qualitative nature as differences observed in subsequent SOC measurements, therefore only data for this witness sample were used in calculations of the reference detector RSR. Data from both witness samples were used in estimating the uncertainty of the reference detector RSR.

The mean spectral quantities on the right side of Equation (3) were obtained from multiple raw spectra that were normalized to the mean within a limited band before averaging. This operation was performed to eliminate offset errors between measurements and leave only relative uncertainties within each passband.

The standard uncertainty of the MIC1 output beam spectral intensity is based on NIST guidelines [5] as given in Equation (4):

$$\sigma_S(\bar{\upsilon}) = \sqrt{{\sigma_{S_{FTS}}}^2(\bar{\upsilon}) + {\sigma_{\tau_{FM}}}^2(\bar{\upsilon}) + {\sigma_{RSR_{RD}}}^2(\bar{\upsilon})} \tag{4}$$

where

$\sigma_S(\bar{\upsilon})$ = standard uncertainty of the output beam relative spectral intensity (%)

$\sigma_{S_{FTS}}(\bar{\upsilon})$ = FTS output spectrum measurement uncertainty (%)

$\sigma_{\tau_{FM}}(\bar{\upsilon})$ = reference detector optical system reflectance uncertainty (%)

$\sigma_{RSR_{RD}}(\bar{\upsilon})$ = spectral reference detector relative spectral response uncertainty (%)

$\bar{\upsilon}$ = wavenumber (cm^{-1})

The spectral reference detector relative spectral response uncertainty, $\sigma_{RSR_{RD}}(\bar{\upsilon})$, was determined by taking the standard deviation of the reference detector RSR estimates determined separately from each reference detector element witness sample reflectance measurement. These individual SRD RSR estimates were normalized to the combined mean within the radiometer response band as previously explained, before calculation of the standard deviation. The other uncertainties in Equation (4) are given by the standard error in the mean of the individual mean-normalized spectra. The uncertainty analysis described in Equation (4) was performed in the spectral domain.

The FTS output beam spectral intensity for wavelengths between 200 and 800 nm is shown in Figure 12. MIC1 output spectra for wavelengths between 1 and 10 μm are shown in Figure 13 and Figure 14. Corresponding uncertainty curves (TBR) are shown as well.

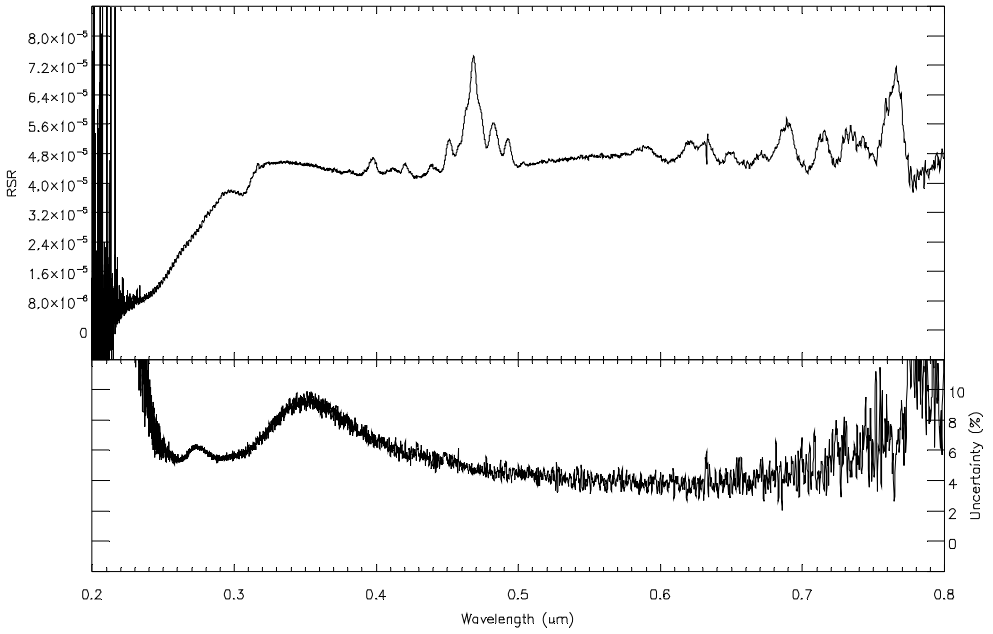

Figure 12. FTS Output Spectrum (Quartz Beamsplitter & Xe Lamp Source)

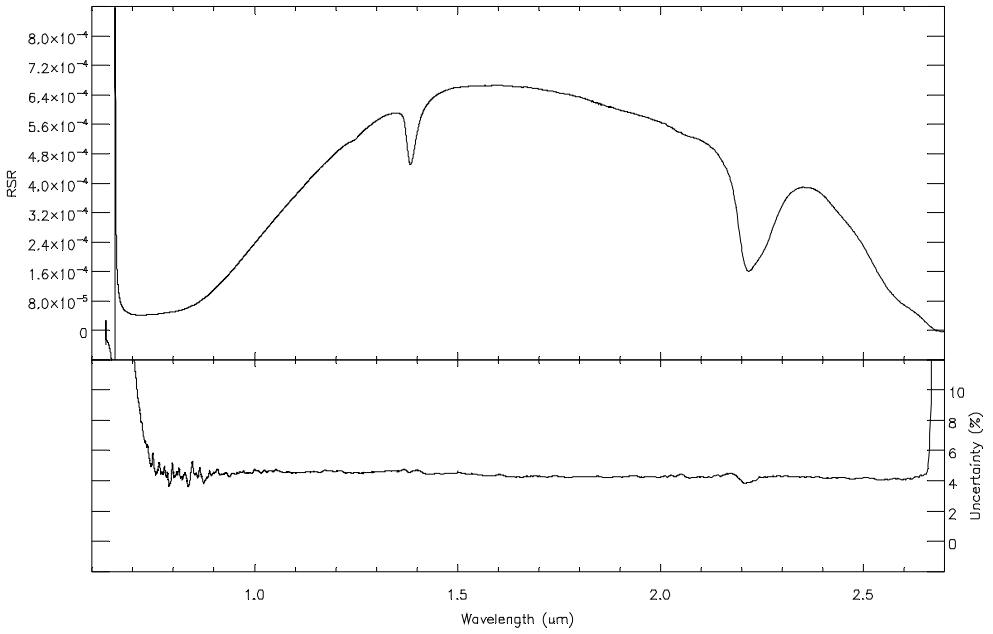

Figure 13. MIC1 Output Spectrum (Quartz Beamsplitter & Tungsten-Halogen Source)

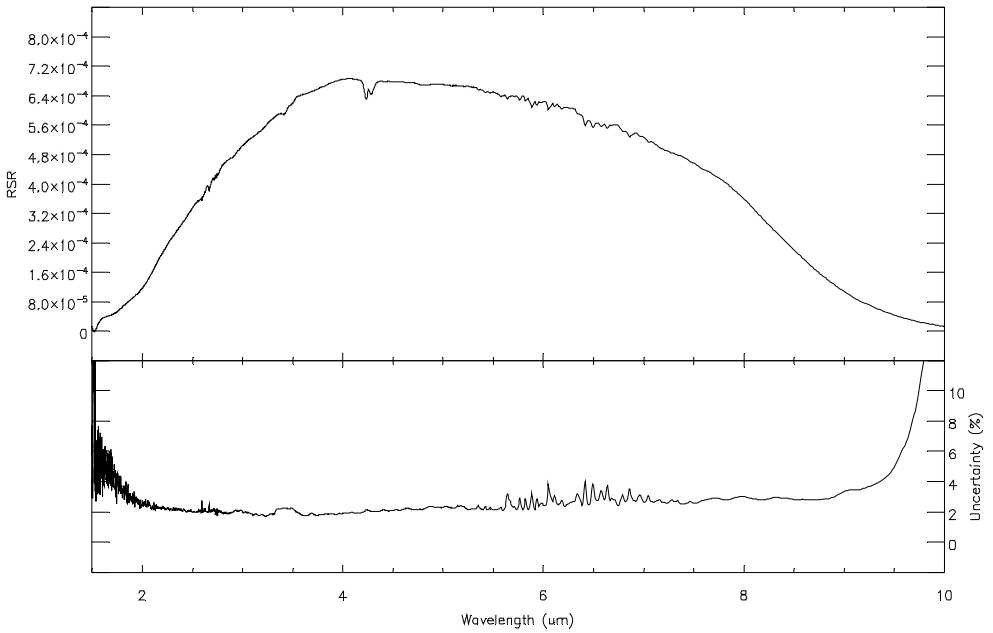

Figure 14. MIC1 Output Spectrum (KBr Beamsplitter & Glowbar Source)

5.1.1.2. In-Band Relative Spectral Response

During RSR calibration measurements and SRD measurements, source tracking spectra were collected using the FTS internal detector to monitor the spectral output of the FTS. Tracking spectra from both data collection periods were used to generate a correction factor to compensate for FTS source temperature drift or beamsplitter alignment changes during calibration data collection relative to SRD measurements. The output spectrum of the FTS and MIC1 system measured using the spectral reference detector was corrected using the appropriate tracking spectra, and the raw RSR measurement was divided by the result, to calculate the SOFIE in-band system RSR. The equation used to calculate in-band RSR, $RSR(\bar{\upsilon})$, is

$$RSR(\bar{\upsilon}) = \frac{S_{Raw}(\bar{\upsilon})}{S(\bar{\upsilon})}\left(\frac{ST_{SRD}(\bar{\upsilon})}{ST_{IC}(\bar{\upsilon})}\right)\left(\frac{1}{K_{Norm}}\right) \tag{5}$$

where

$RSR(\bar{\upsilon})$ = measured in-band RSR spectrum

$S_{Raw}(\bar{\upsilon})$ = in-band raw response spectrum

$S(\bar{\upsilon})$ = relative spectral intensity of exit beam from Equation (3)

$ST_{SRD}(\bar{\upsilon})$ = benchmark spectrum during reference detector measurement

$ST_{IC}(\bar{\upsilon})$ = benchmark spectrum during instrument calibration

K_{Norm} = in-band RSR peak normalization factor

$\bar{\upsilon}$ = wavenumber (cm^{-1})

The standard uncertainty of the in-band RSR is based on NIST guidelines [5] as given in Equation (6):

$$\sigma_{RSR}(\bar{\upsilon}) = \sqrt{{\sigma_{S_{Raw}}}^2(\bar{\upsilon}) + {\sigma_S}^2(\bar{\upsilon}) + {\sigma_{ST_{SRD}}}^2(\bar{\upsilon}) + {\sigma_{ST_{IC}}}^2(\bar{\upsilon})} \quad (6)$$

where

$\sigma_{RSR}(\bar{\upsilon})$ = standard uncertainty of the in-band RSR (%)

$\sigma_{S_{Raw}}(\bar{\upsilon})$ = measurement repeatability uncertainty (%)

$\sigma_S(\bar{\upsilon})$ = uncertainty of MIC1 exit beam from Equation (4) (%)

$\sigma_{ST_{SRD}}(\bar{\upsilon})$ = benchmark spectrum uncertainty during reference detector measurement

$\sigma_{ST_{IC}}(\bar{\upsilon})$ = benchmark spectrum uncertainty during instrument calibration

$\bar{\upsilon}$ = wavenumber (cm^{-1})

The measurement repeatability uncertainty, $\sigma_{S_M}(\bar{\upsilon})$, is taken to be 0.5% for cases where only a single spectrum is available. This value is a worst case number consistent with other RSR measurements and the measurement signal-to-noise ratio. The uncertainty of the incident beam relative spectral intensity, $\sigma_S(\bar{\upsilon})$, is given by Equation (4).

Plots of in-band RSR for all bands are shown in Figure 15 through Figure 30, for cold, nominal, and warm science operating conditions. Instrument specifications for 50%-of-peak band limits are indicated by vertical red dotted lines. Measured 50%-of-peak limits for each SOFIE band are listed in Table 10. Average in-band uncertainty through for each SOFIE spectral band is listed in Table 11, for cold, nominal, and warm temperatures.

All in-band uncertainties are on the order of 1% or less, with the exception of bands 1 & 2, where the FTS was introduced directly into the SOFIE instrument, rather than through MIC1, to avoid loss of signal due to the gold mirrors in MIC1. Because the FTS output beam does not fill the SOFIE aperture, four measurements were made with the FTS beam positioned in different parts of the SOFIE aperture. It is the repeatability of these four measurements, as given by the standard deviation, which dominates the uncertainty for bands 1 & 2.

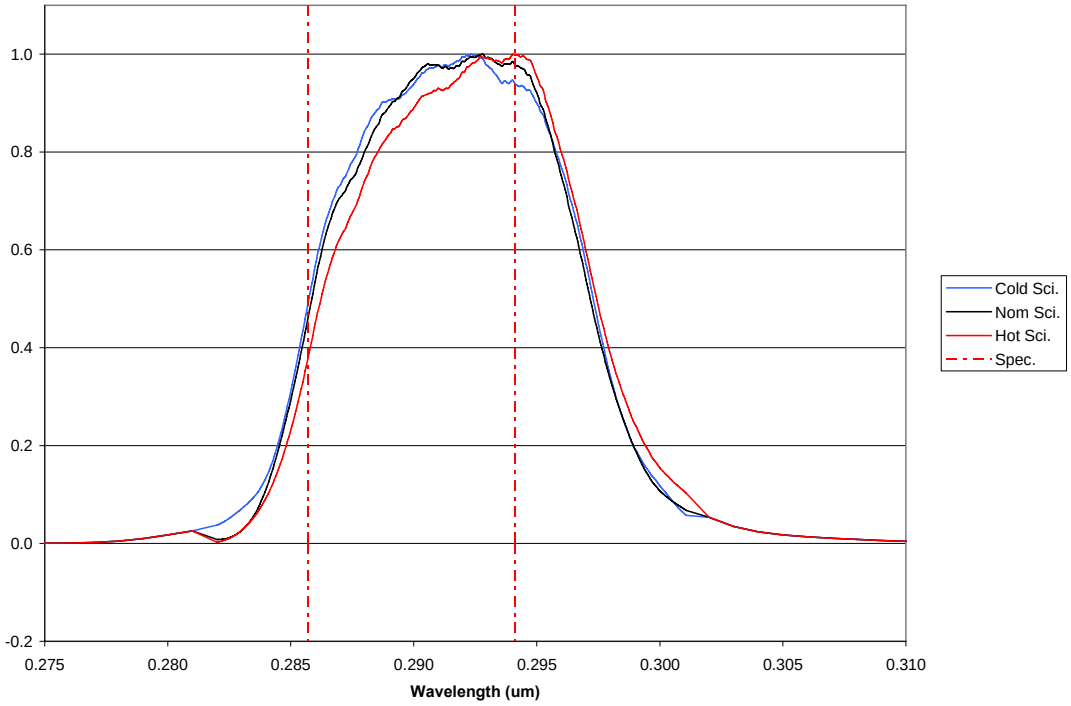

Figure 15. Band 1 RSR (In-Band)

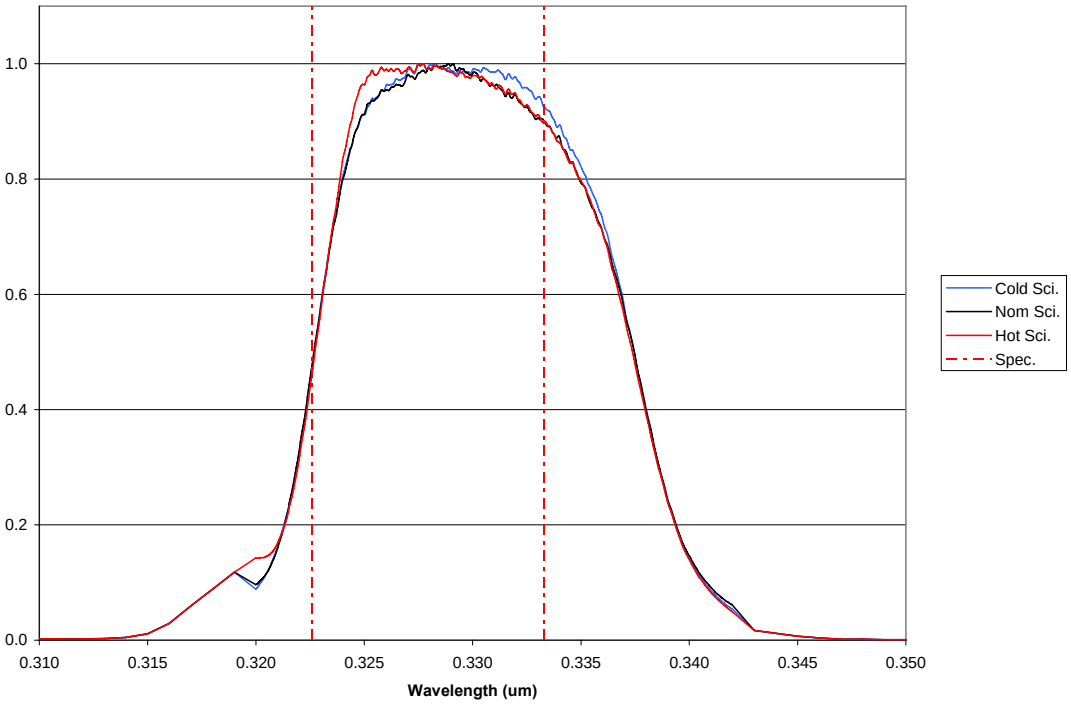

Figure 16. Band 2 RSR (In-Band)

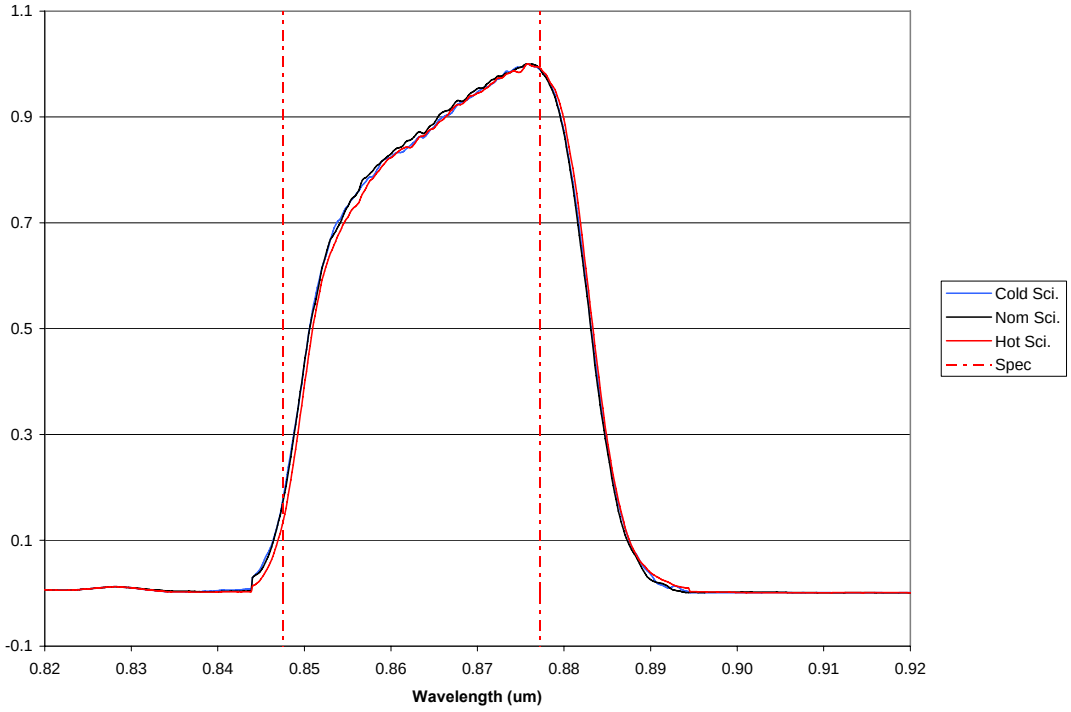

Figure 17. Band 3 RSR (In-Band)

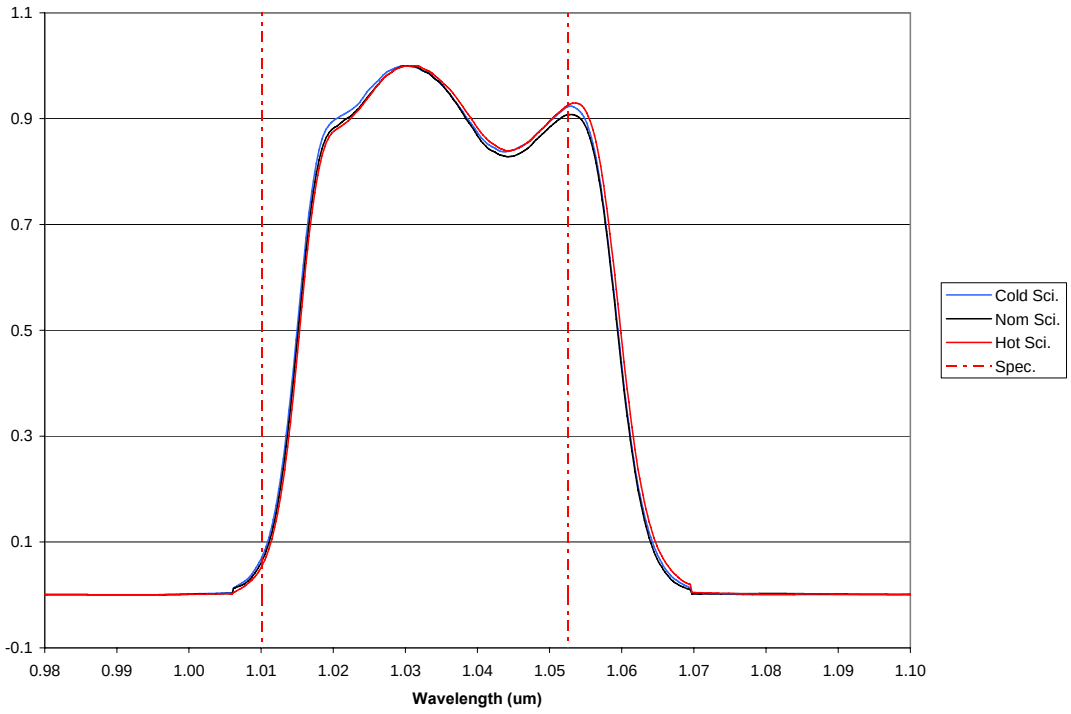

Figure 18. Band 4 RSR (In-Band)

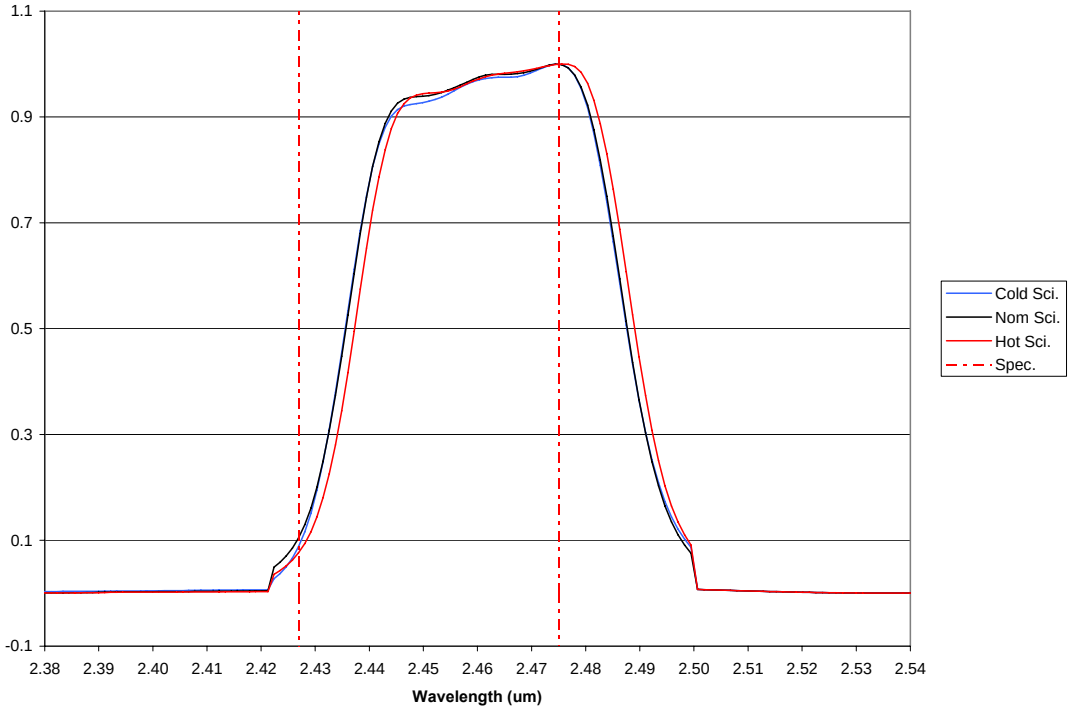

Figure 19. Band 5 RSR (In-Band)

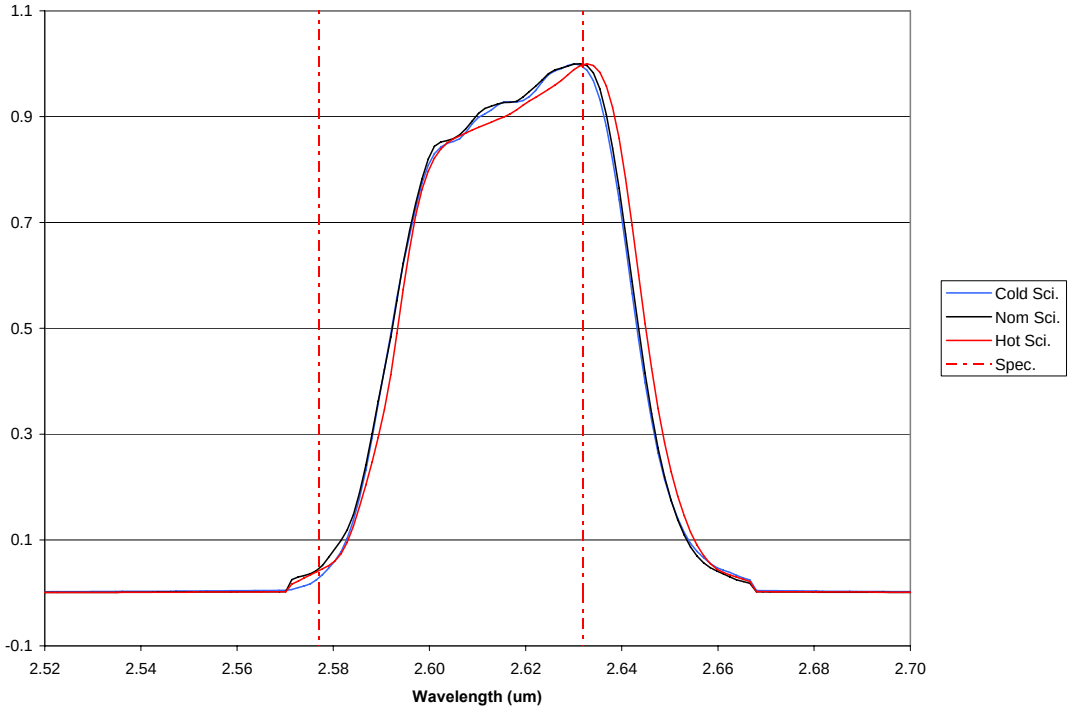

Figure 20. Band 6 RSR (In-Band)

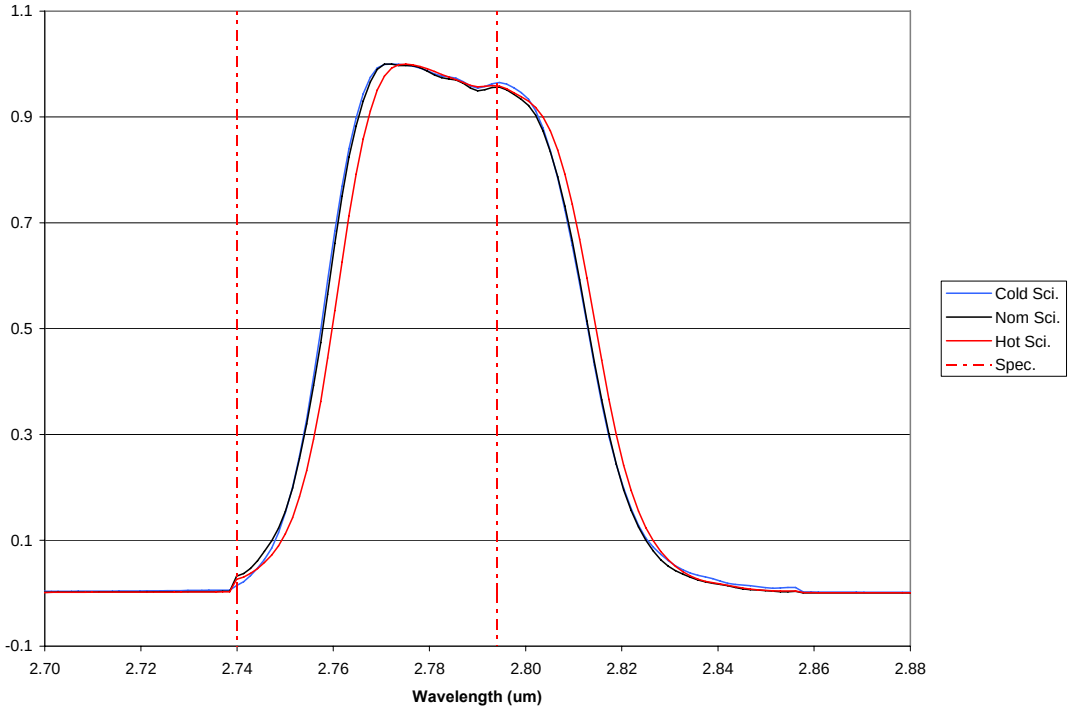

Figure 21. Band 7 RSR (In-Band)

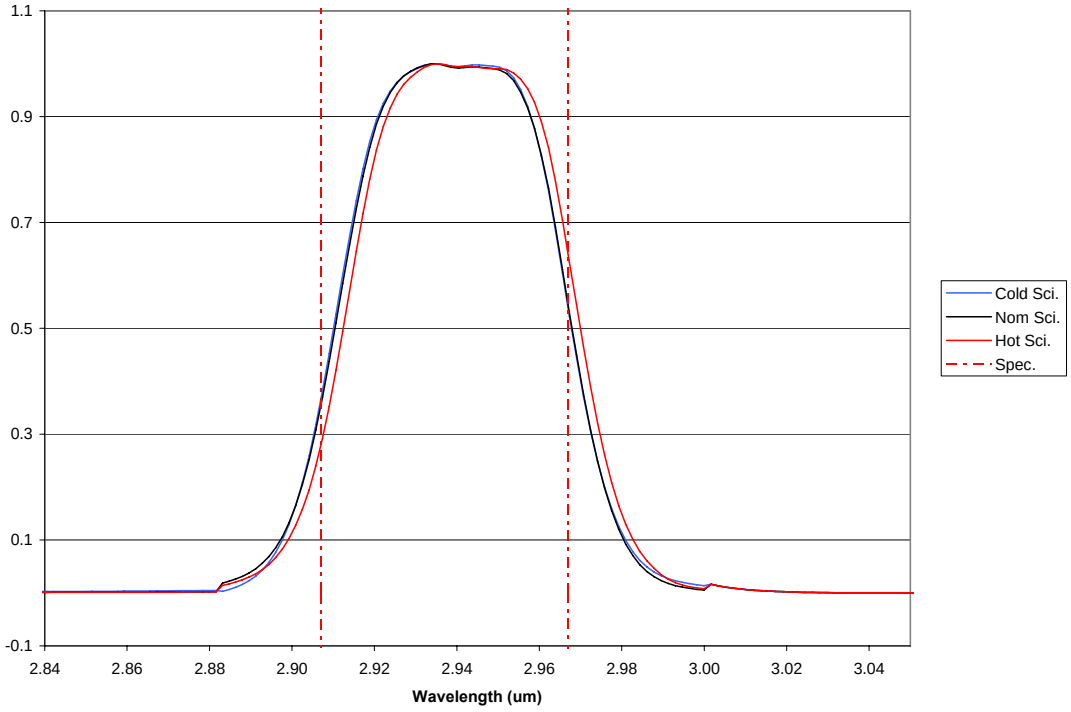

Figure 22. Band 8 RSR (In-Band)

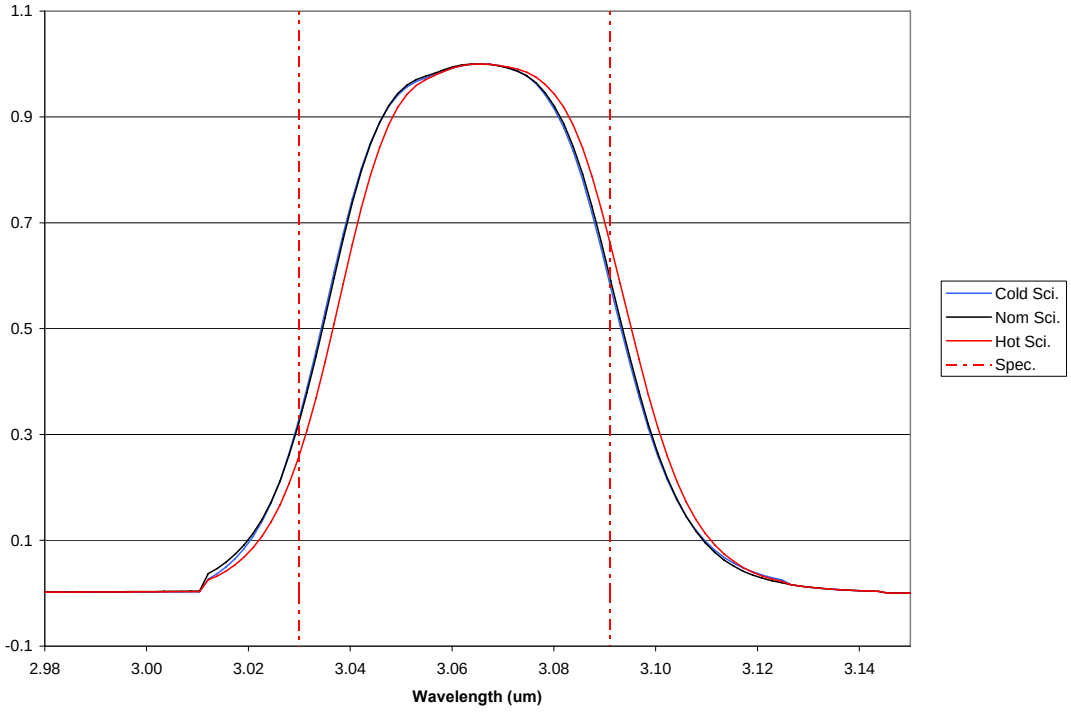

Figure 23. Band 9 RSR (In-Band)

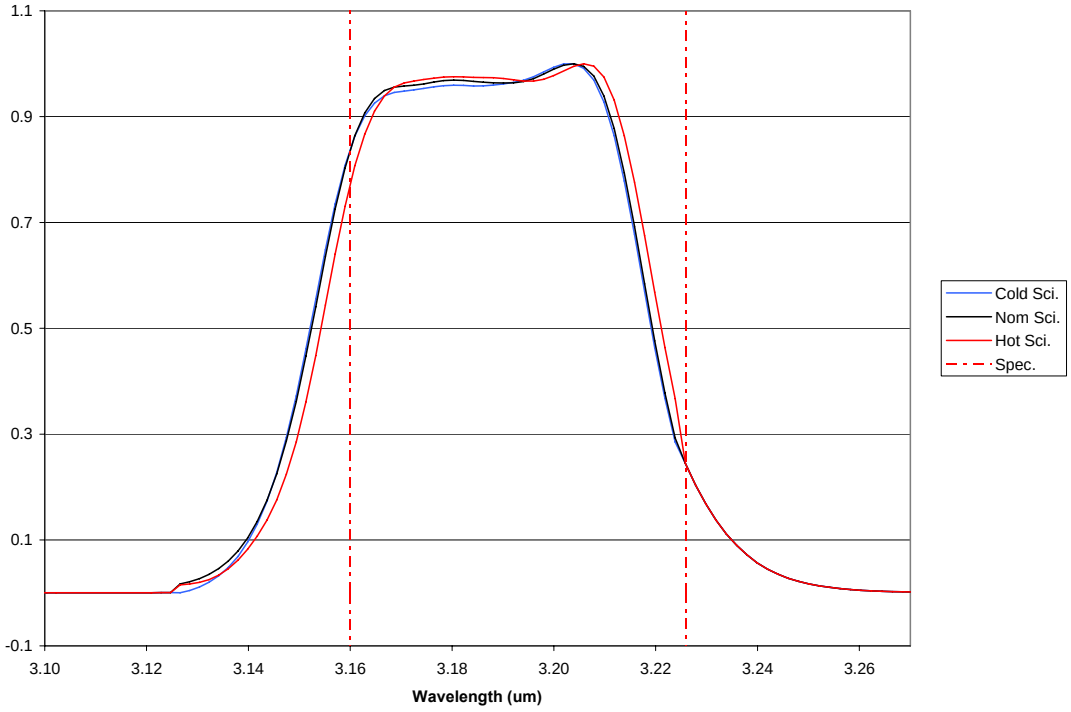

Figure 24. Band 10 RSR (In-Band)

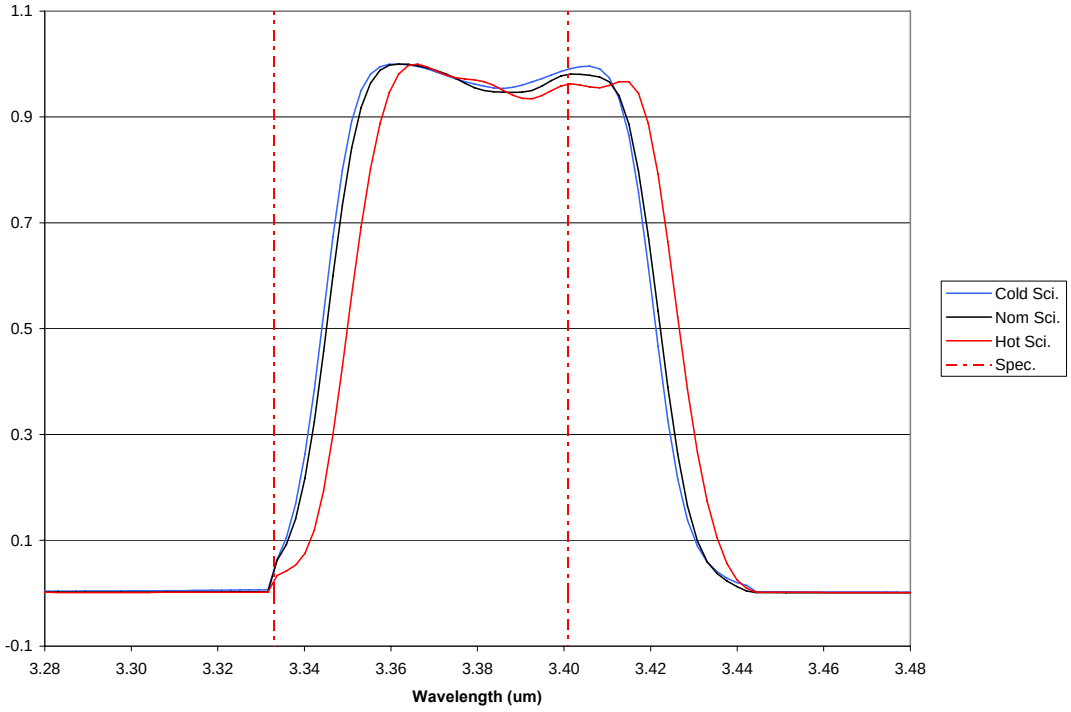

Figure 25. Band 11 RSR (In-Band)

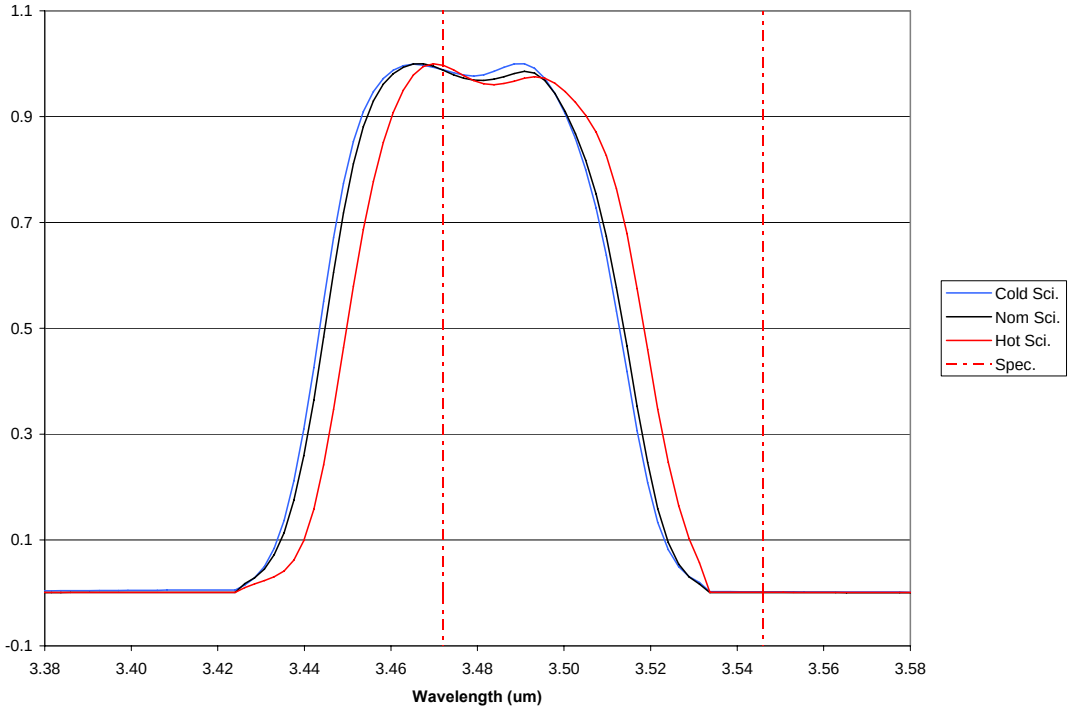

Figure 26. Band 12 RSR (In-Band)

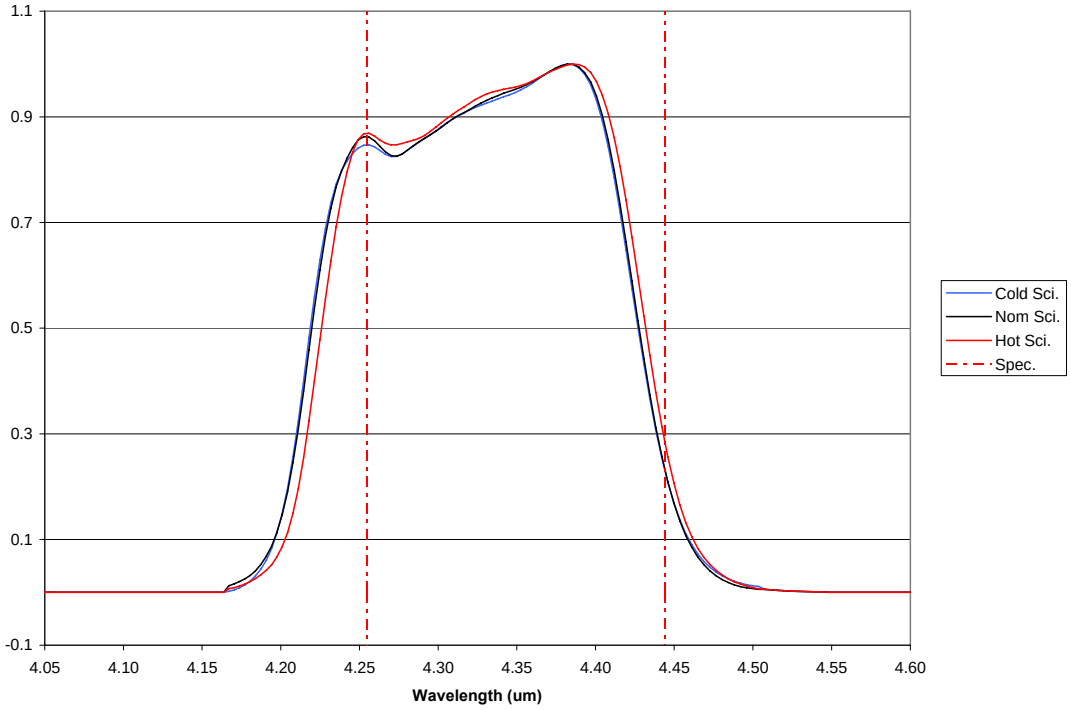

Figure 27. Band 13 RSR (In-Band)

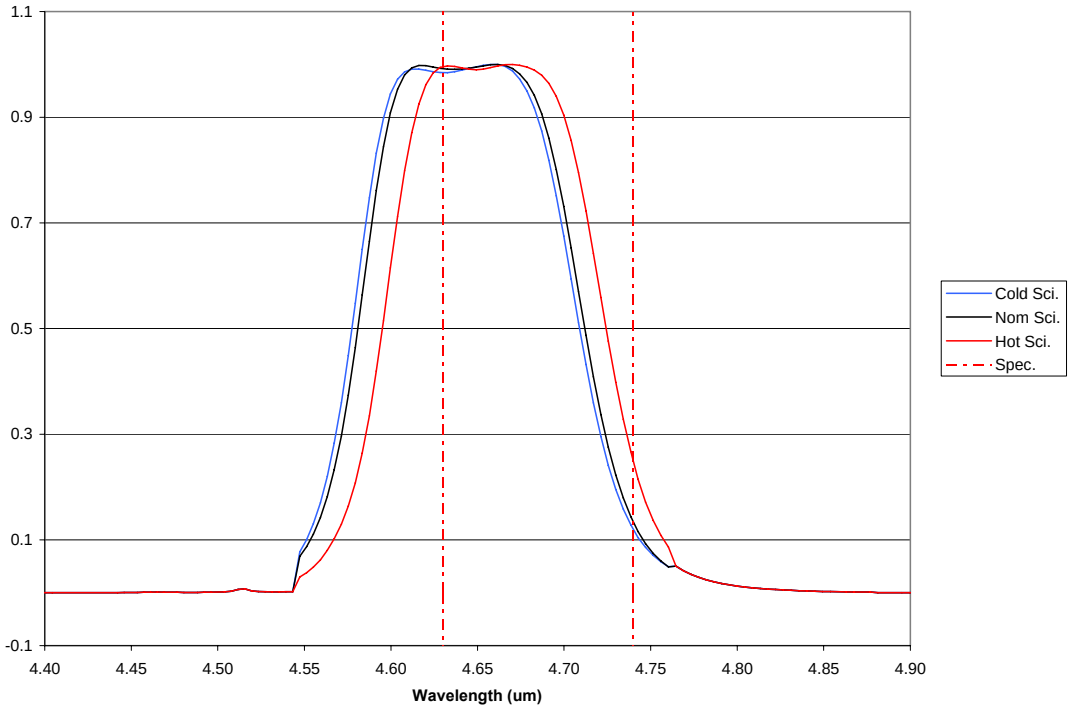

Figure 28. Band 14 RSR (In-Band)

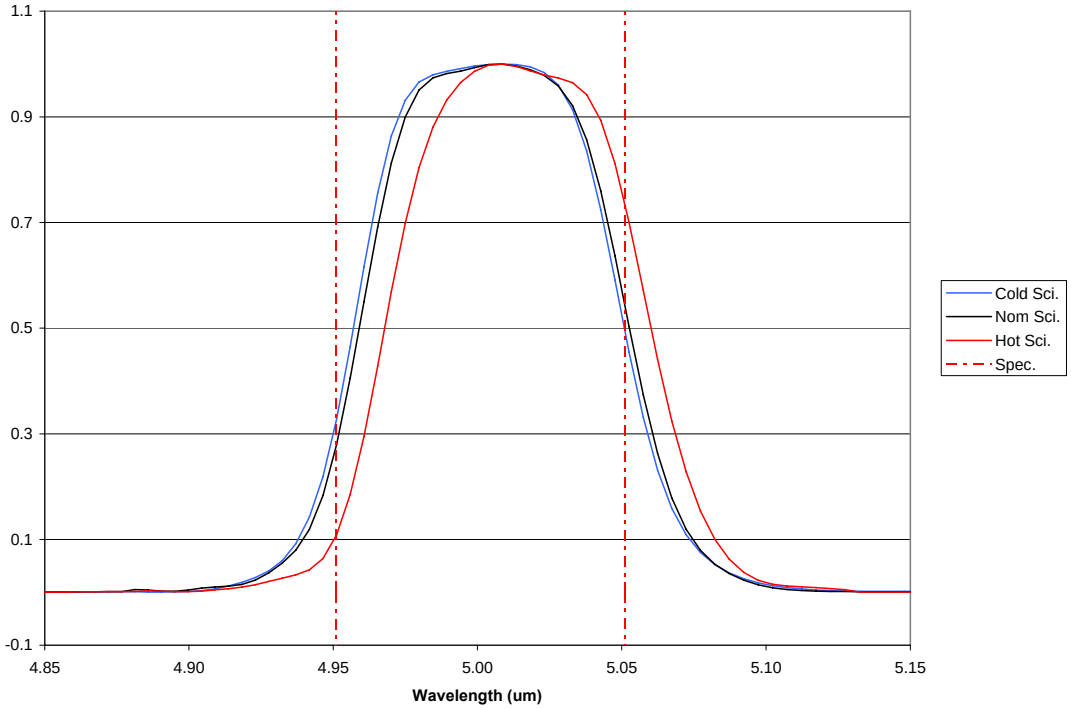

Figure 29. Band 15 RSR (In-Band)

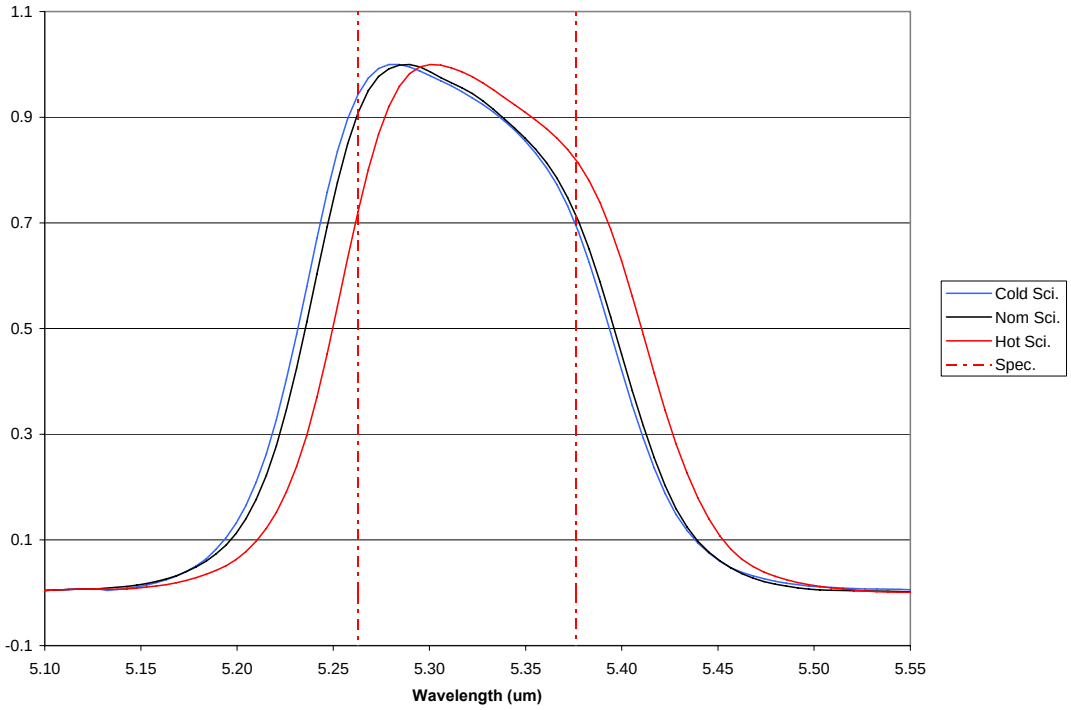

Figure 30. Band 16 RSR (In-Band)

Table 10. SOFIE Band Limits

Band	Specification	Cold Science	Nominal Science		Warm Science
	Cuton - Cutoff (μm)	Cuton-Cutoff (μm)	Cuton-Cutoff (μm)	Cuton-Cutoff Δ from spec. (μm)	Cuton-Cutoff (μm)
1	0.2857 – 0.2941	0.2857 – 0.2973	0.2859 – 0.2972	0.0002– 0.0031	0.2862 – 0.2974
2	0.3226 – 0.3333	0.3227 – 0.3374	0.3227 – 0.3375	0.0001 – 0.0042	0.3227 – 0.3374
3	0.8475 – 0.8772	0.8506 – 0.8831	0.8506 – 0.8831	0.0031 – 0.0059	0.8510 – 0.8833
4	1.0101 – 1.0526	1.015 – 1.060	1.015 – 1.059	0.0051 – 0.0068	1.015 – 1.060
5	2.427 – 2.475	2.436 – 2.488	2.436 – 2.488	0.0087 – 0.0127	2.437 – 2.489
6	2.577 – 2.632	2.592 – 2.643	2.592 – 2.643	0.0153 – 0.0115	2.593 – 2.645
7	2.740 – 2.794	2.757 – 2.813	2.758 – 2.813	0.0178 – 0.0190	2.760 – 2.815
8	2.907 – 2.967	2.910 – 2.968	2.910 – 2.968	0.0034 – 0.0009	2.912 – 2.970
9	3.030 – 3.091	3.034 – 3.093	3.035 – 3.093	0.0046 – 0.0025	3.037 – 3.095
10	3.160 – 3.226	3.152 – 3.219	3.152 – 3.219	-0.0076 – -0.0066	3.154 – 3.221
11	3.333 – 3.401	3.344 – 3.421	3.345 – 3.422	0.0121 – 0.0212	3.350 – 3.427
12	3.472 – 3.546	3.444 – 3.513	3.445 – 3.514	-0.0272 – -0.0322	3.450 – 3.518
13	4.255 – 4.444	4.219 – 4.427	4.220 – 4.428	-0.0352 – -0.0163	4.226 – 4.432
14	4.630 – 4.740	4.577 – 4.709	4.581 – 4.712	-0.0491 – -0.0280	4.595 – 4.724
15	4.951 – 5.051	4.957 – 5.051	4.959 – 5.053	0.0080 – 0.0016	4.968 – 5.060
16	5.263 – 5.376	5.232 – 5.394	5.236 – 5.396	-0.0275 – 0.0200	5.250 – 5.410

Table 11. SOFIE In-Band Uncertainty (%)

Band	Cold Science	Nominal Science	Warm Science
1	6.26569	4.87281	5.16396
2	6.19524	5.35885	8.36763
3	1.14205	1.08671	1.14152
4	0.947297	0.878171	0.947697
5	0.881406	0.879039	0.912816
6	1.26946	1.00954	1.00286
7	1.04521	0.929245	0.933752
8	0.879378	0.877856	0.88246
9	0.881433	0.881352	0.885619
10	0.870331	0.870538	0.875114
11	0.873662	0.873866	0.87804
12	0.876227	0.876564	0.878495
13	1.15053	1.08375	0.960708
14	0.872072	0.872195	0.875031
15	0.875005	0.872074	0.872889
16	0.936165	0.894523	0.893113

5.1.1.3. Out-of-Band Relative Spectral Response

SOFIE out-of-band RSR measurements were made using the Cascaded Filter Fourier Transform Spectrometer (CFFTS) method [**8**]. The CFFTS method employs a bandpass filter to eliminate in-band flux and characterize different spectral regions of out-of-band blocking. Bandpass filters inserted in the FTS itself were used during out-of-band RSR measurements. Based on the filter substrate used for SOFIE bands 5 - 16, out-of-band RSR measurements were not made for these bands for wavelengths shorter than 1.1 μm [**9**]. For bands 1 & 2, out of-band RSR measurements were made between 0.2 and 0.4 μm, and for bands 3 & 4 between 0.7 and 2.0 μm, based on detector response limits. Out-of-band relative spectral response (RSR) measurements used the same configuration as for in-band RSR measurements, with the addition of blocking filters in the FTS.

The measured out-of-band RSR spectra were corrected for the relative spectral intensity of the calibration chamber exit beam and normalized to the in-band RSR to give a composite in-band and out-of-band RSR curve. The calculation used to compute out-of-band RSR and scale it to in-band RSR is:

$$RSR_{XB}(\bar{\upsilon}) = \frac{S_{RawXB}(\bar{\upsilon})}{S(\bar{\upsilon})\tau_{BF}(\bar{\upsilon})}\left(\frac{ST_{SRD}(\bar{\upsilon})}{ST_{IC}(\bar{\upsilon})}\right)\left(\frac{1}{K_{Norm}}\right) \tag{7}$$

where

$RSR_{XB}(\bar{\upsilon})$ = measured out-of-band RSR spectrum

$S_{RawXB}(\bar{\upsilon})$ = out-of-band raw response spectrum

$S(\bar{\upsilon})$ = relative spectral intensity of exit beam from Equation (3)

$\tau_{BF}(\bar{\upsilon})$ = blocking filter transmittance

$ST_{SRD}(\bar{\upsilon})$ = benchmark spectrum during reference detector measurement

$ST_{IC}(\bar{\upsilon})$ = benchmark spectrum during instrument calibration

K_{Norm} = in-band RSR peak normalization factor

$\bar{\upsilon}$ = wavenumber (cm^{-1})

For most out-of-band regions, the true SOFIE response is below the noise floor of the measurement, and the measurement therefore represents an upper limit on the true out-of-band response. Assuming that the true response lies with equal probability anywhere between this noise limit and zero, NIST guidelines [5] dictate that the best estimate of the response is given by the average of the limits, which evaluates to one-half the noise floor. The corresponding uncertainty is given by one-half the range divided by the square root of 3, which evaluates to 57.7%. This is the dominant out-of-band uncertainty, although the total uncertainty is given by the root of the sum of the squares (RSS) of this component with the standard uncertainty of the out-of-band RSR, computed using NIST guidelines in the same way as the in-band RSR uncertainty.

Composite RSR plots were generated by combining in-band RSR data with out-of-band data where appropriate. Composite RSR plots for each band are shown in Figure 31 through Figure 46.

The product of solar flux and SOFIE RSR was integrated over the range shown in the out-of-band RSR plots, to calculate out-of-band response as a fraction of in-band response. These results are shown in Table 12.

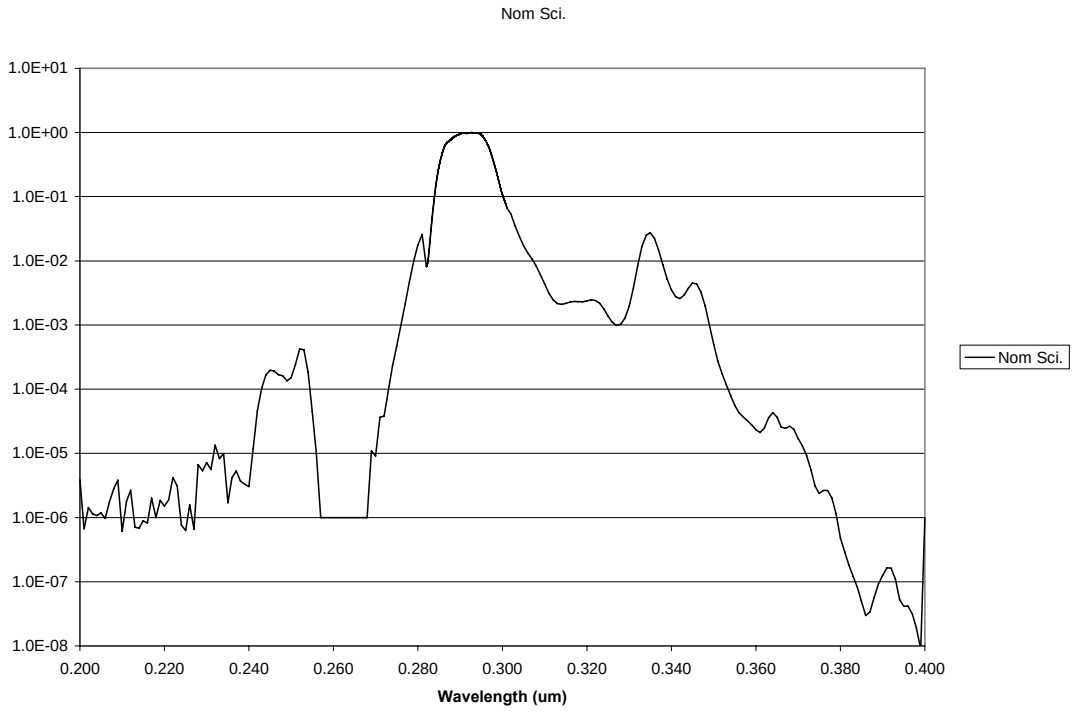

Figure 31. Band 1 RSR (Out-Of-Band)

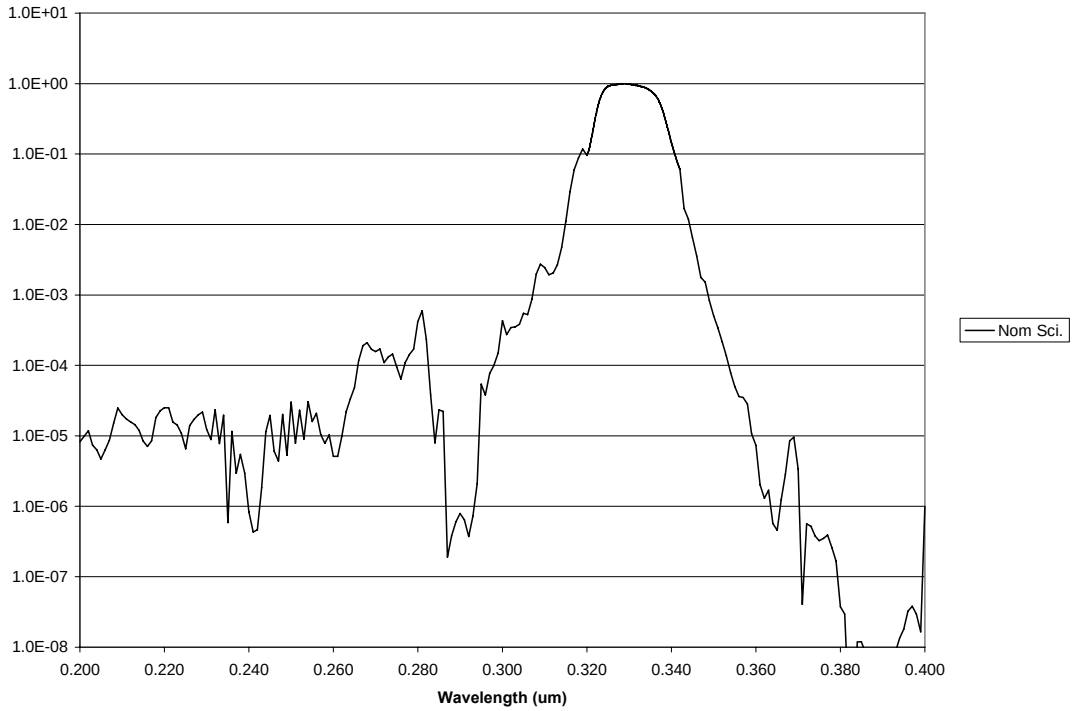

Figure 32. Band 2 RSR (Out-Of-Band)

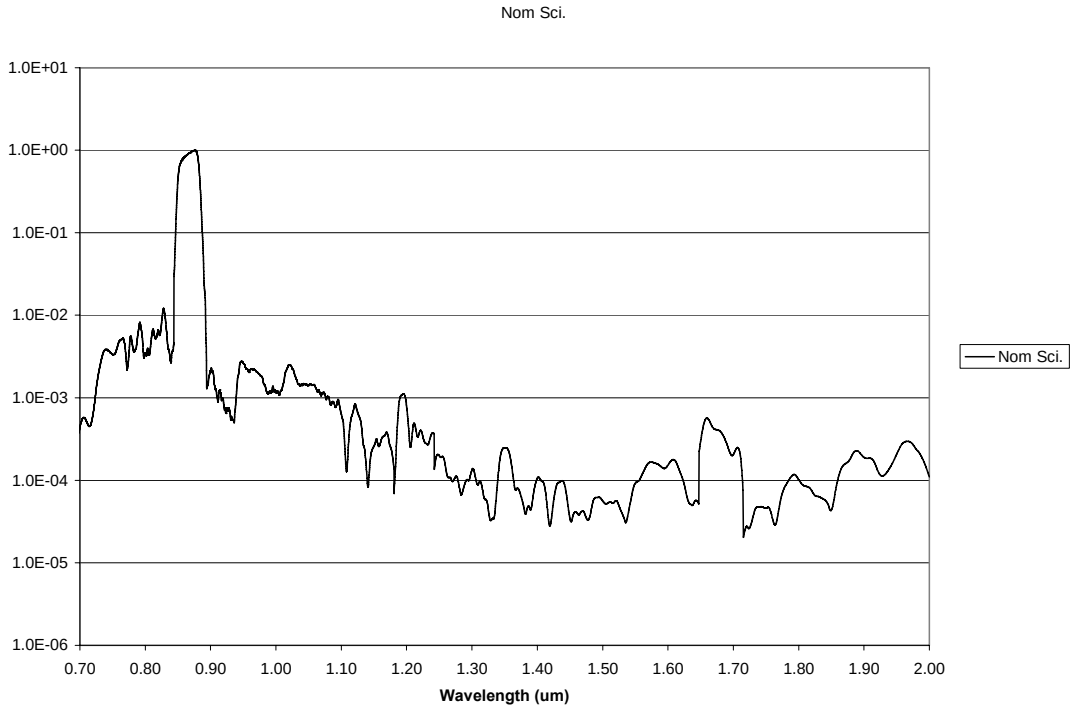

Figure 33. Band 3 RSR (Out-Of-Band)

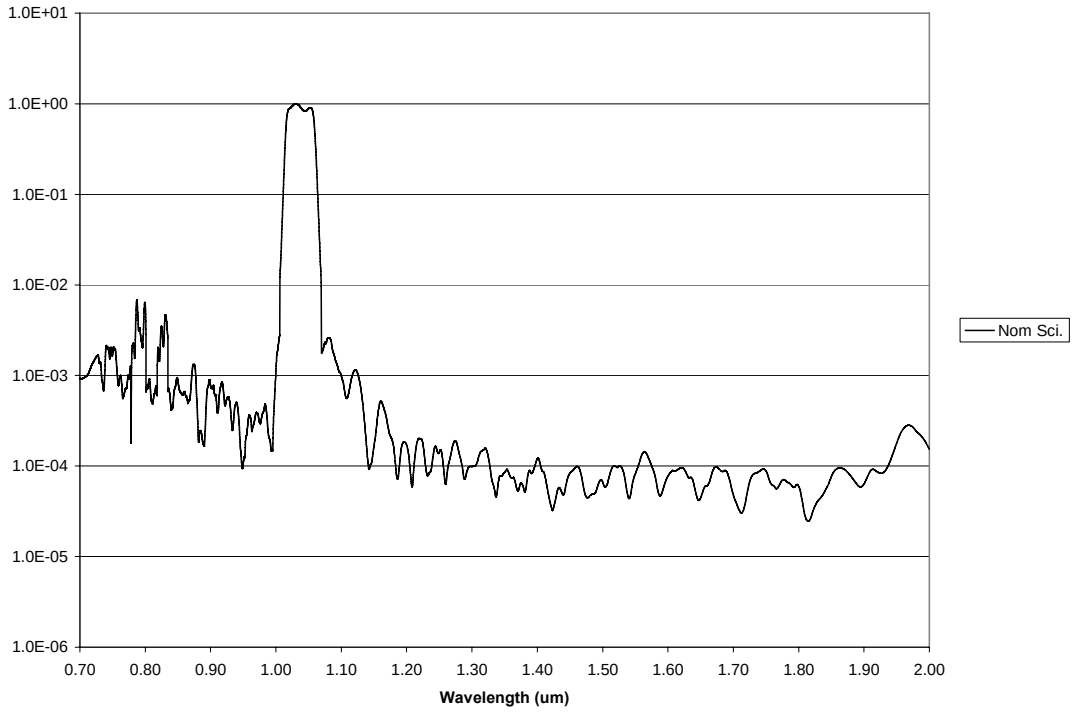

Figure 34. Band 4 RSR (Out-Of-Band)

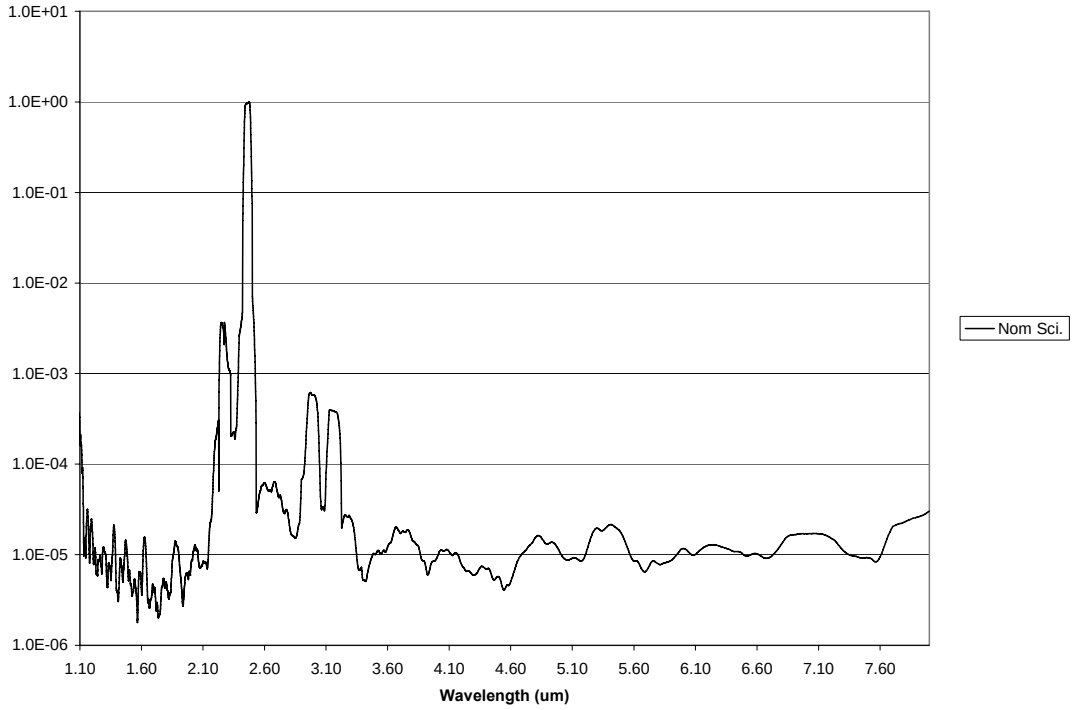

Figure 35. Band 5 RSR (Out-Of-Band)

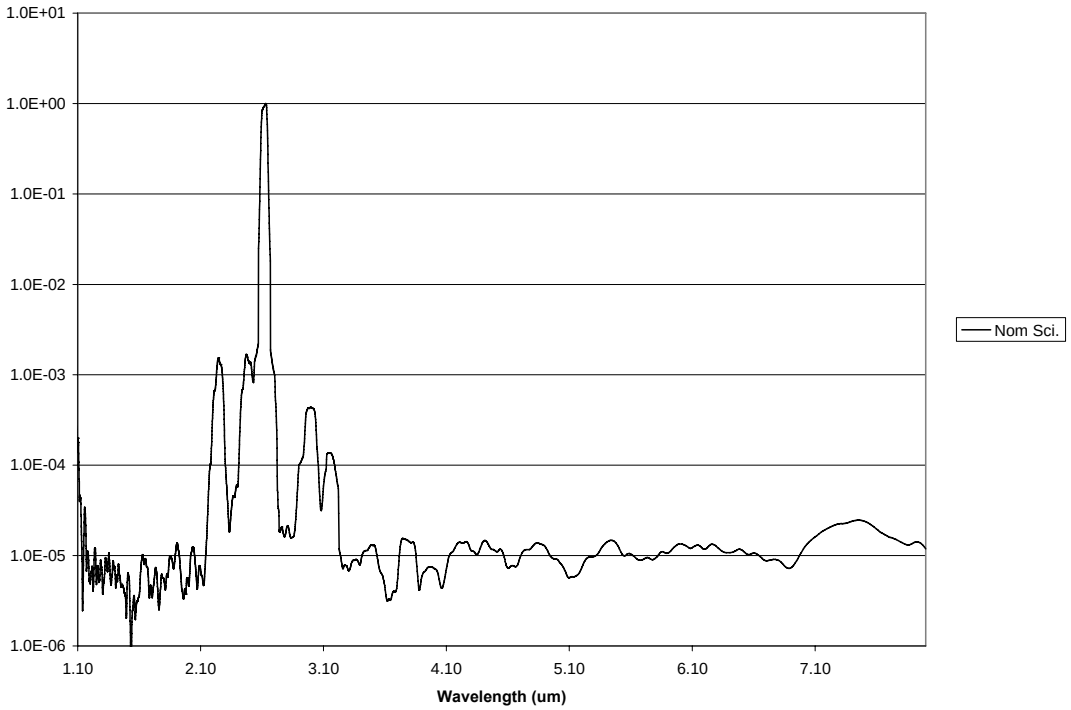

Figure 36. Band 6 RSR (Out-Of-Band)

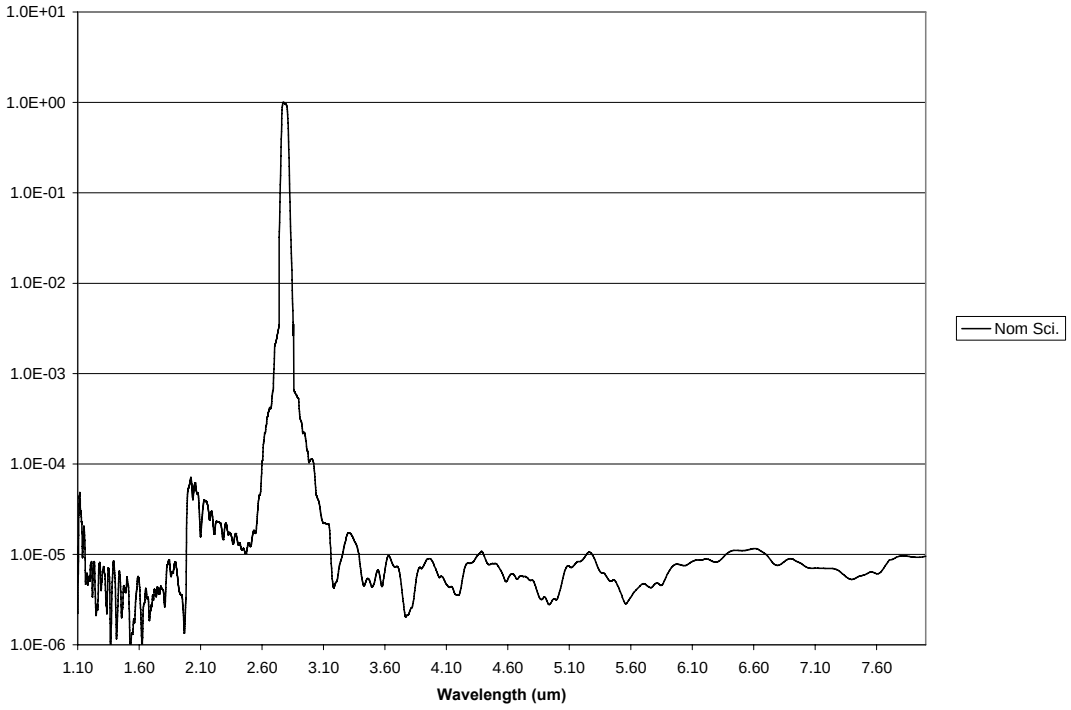

Figure 37. Band 7 RSR (Out-Of-Band)

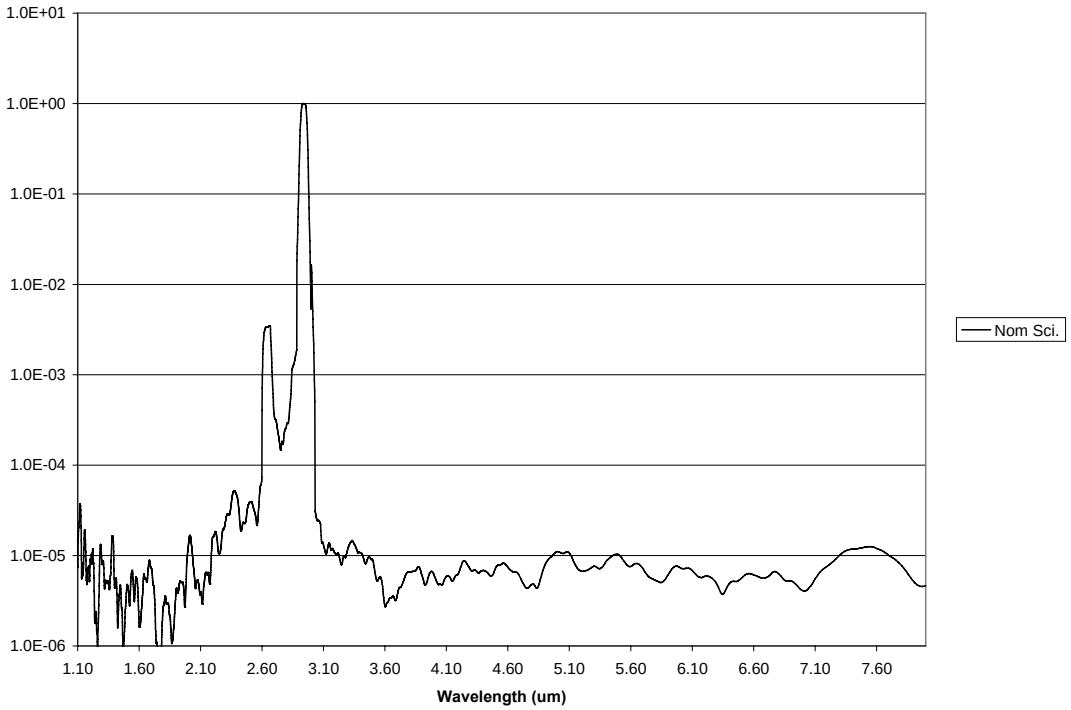

Figure 38. Band 8 RSR (Out-Of-Band)

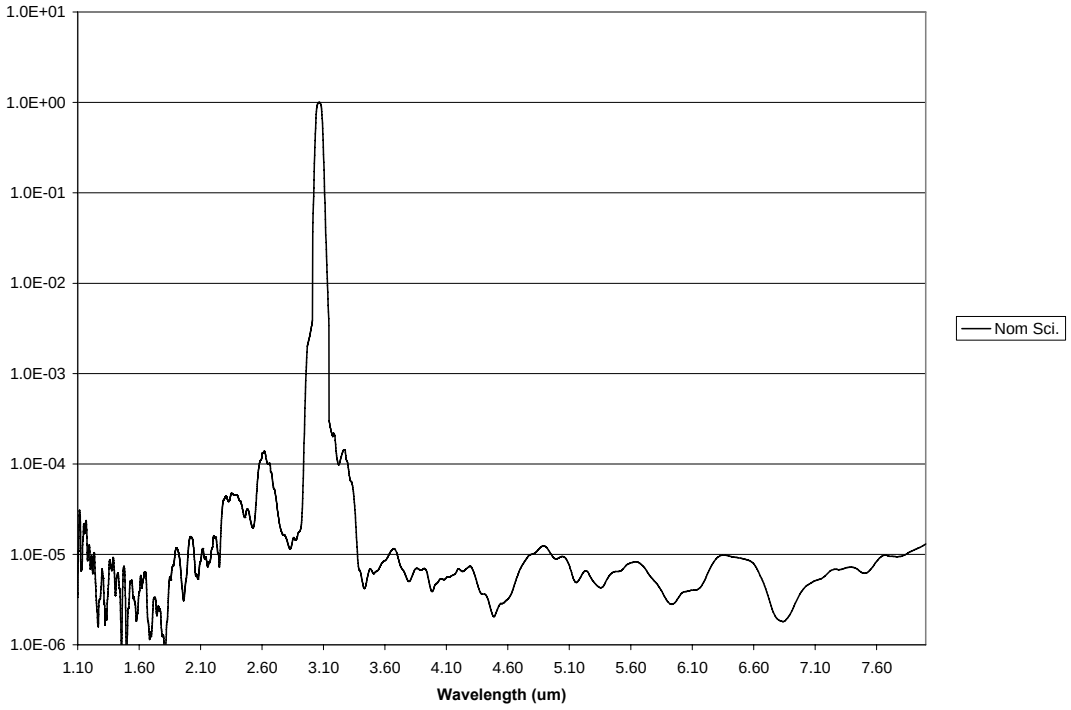

Figure 39. Band 9 RSR (Out-Of-Band)

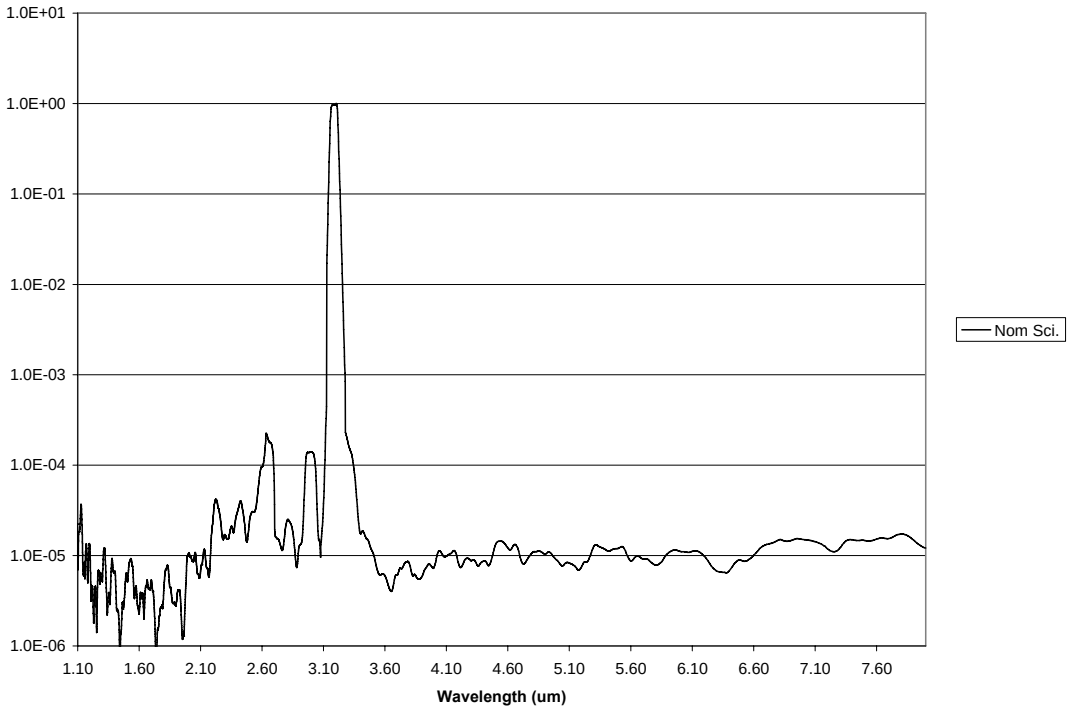

Figure 40. Band 10 RSR (Out-Of-Band)

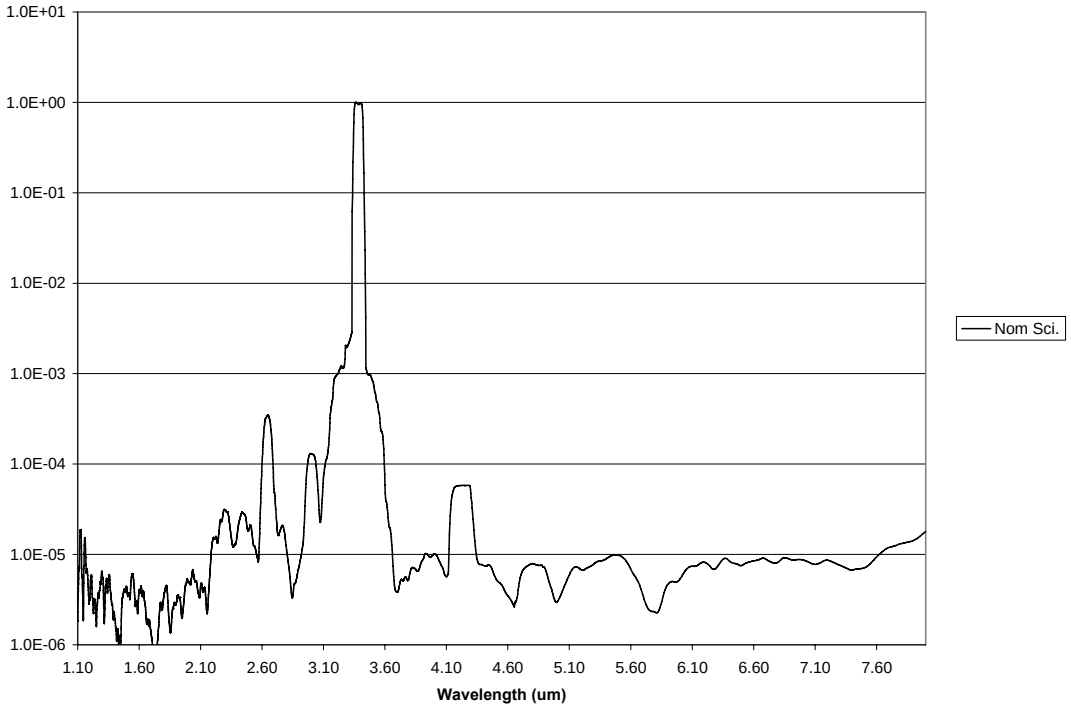

Figure 41. Band 11 RSR (Out-Of-Band)

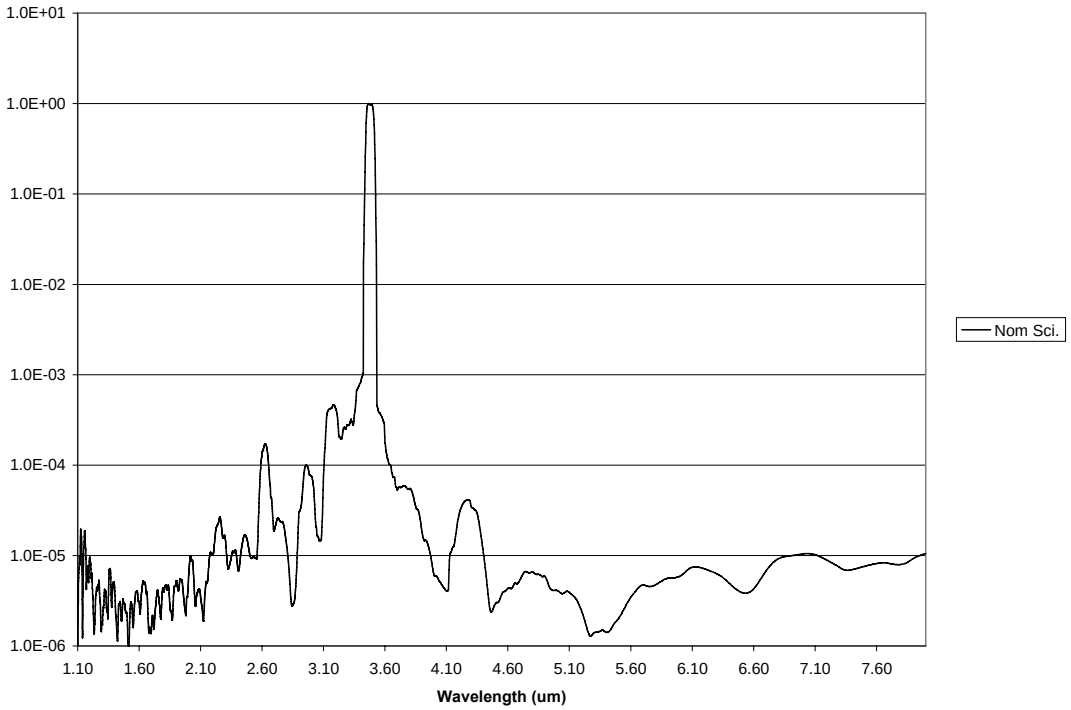

Figure 42. Band 12 RSR (Out-Of-Band)

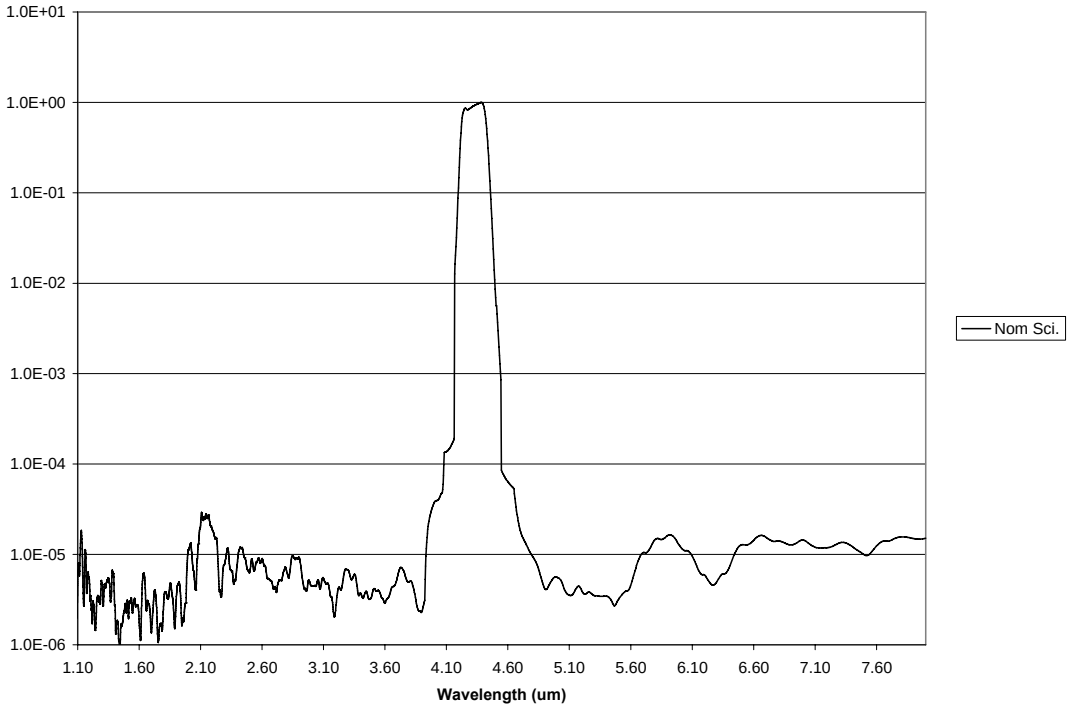

Figure 43. Band 13 RSR (Out-Of-Band)

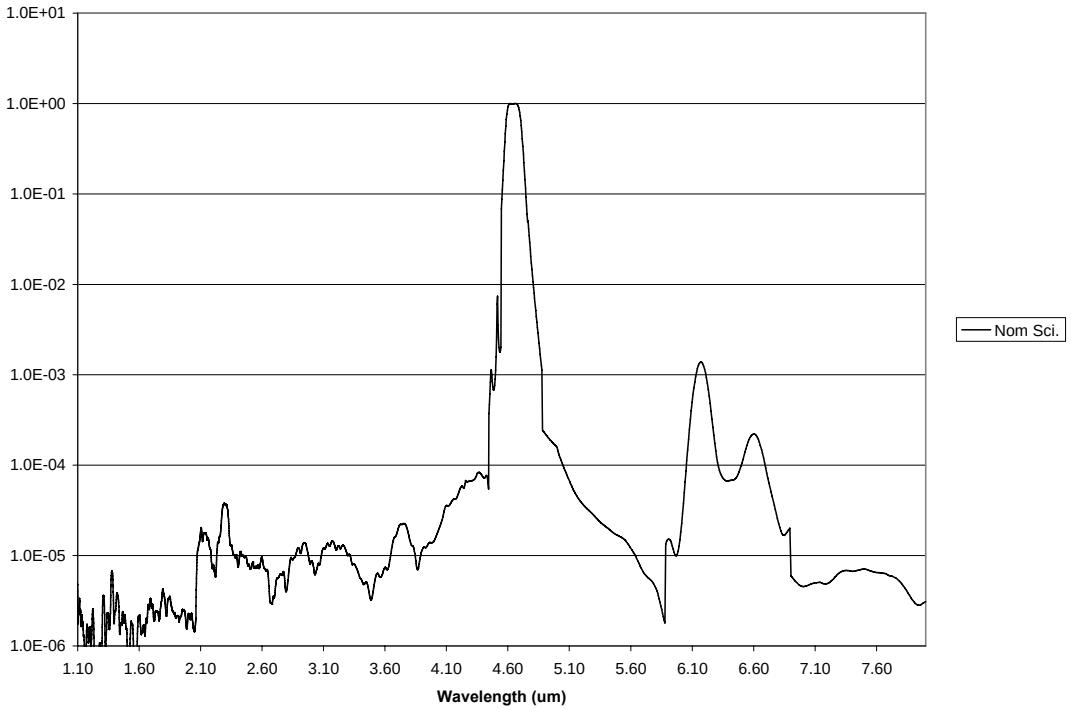

Figure 44. Band 14 RSR (Out-Of-Band)

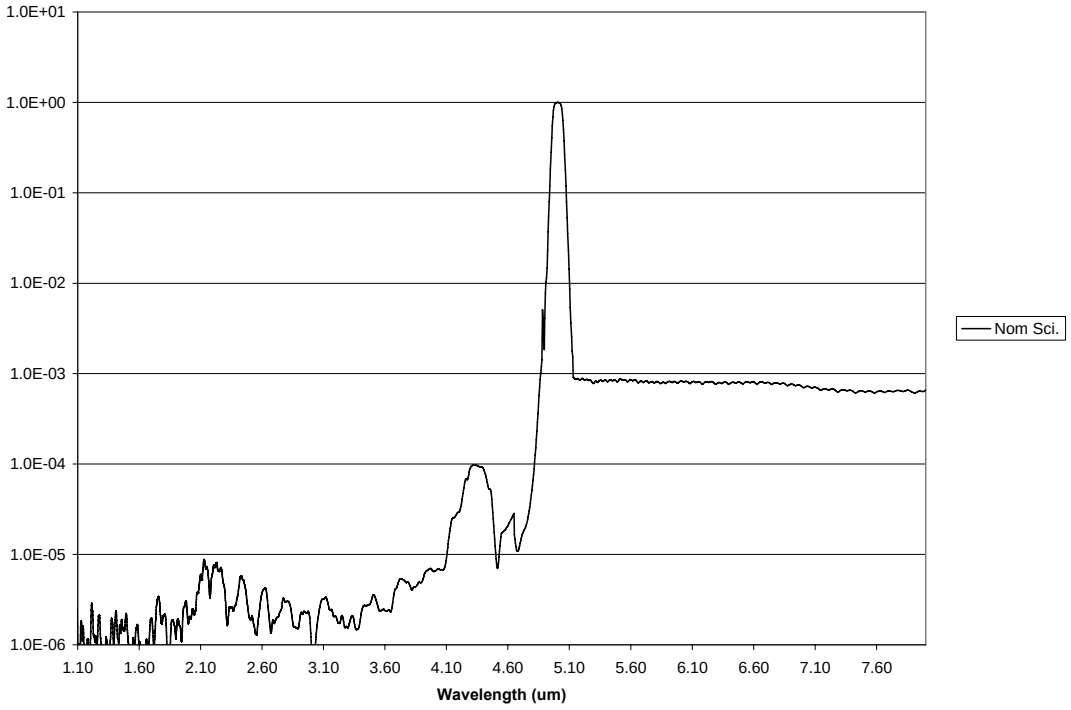

Figure 45. Band 15 RSR (Out-Of-Band)

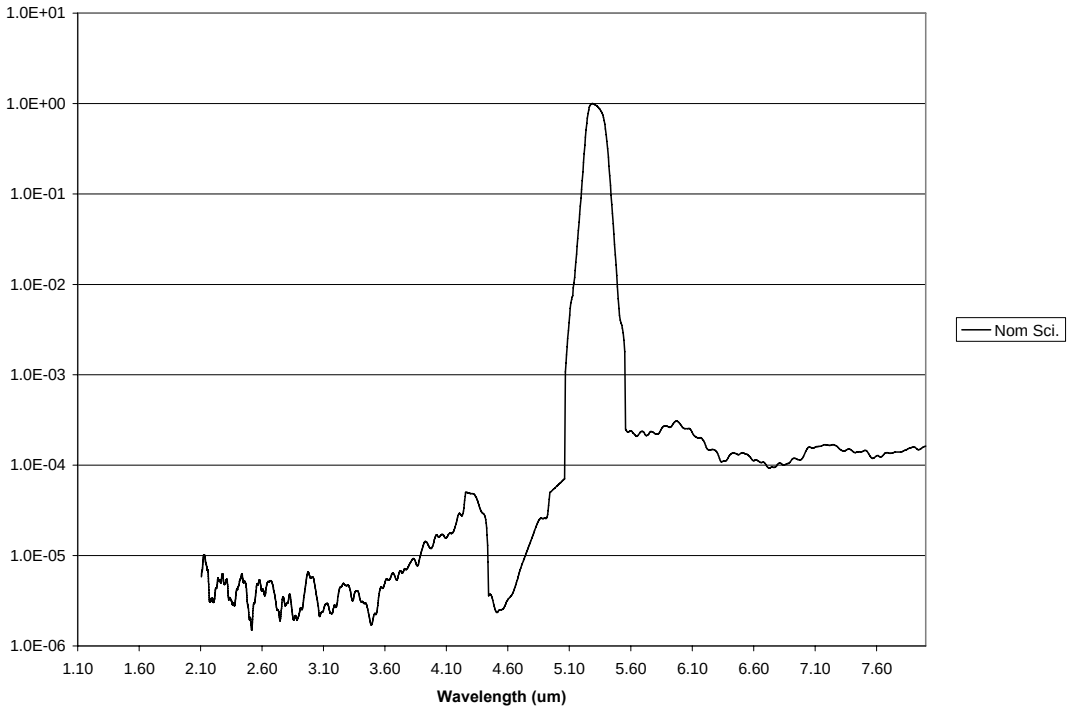

Figure 46. Band 16 RSR (Out-Of-Band)

Table 12. SOFIE Out-of-Band Response

Band	Out-of-Band Response (%)
1	2.6
2	0.03
3	2.1
4	1.6
5	1.0
6	1.1
7	0.5
8	1.0
9	0.3
10	0.3
11	0.6
12	0.7
13	0.1
14	0.4
15	1.1
16	0.5

5.1.2. Point Source FOV

SOFIE field of view (FOV) characterization measurements were made following final instrument assembly, including ND filter installation. SOFIE was installed in the test chamber and operated under vacuum. On-axis FOV measurements were made for each individual spectral band at cold, nominal, and warm instrument operating temperatures, while off-axis FOV tests were made at nominal temperatures only. The SOFIE pointing mirror was fixed at nominal orientation. FOV characterization data were collected using point source and knife-edge scan methods.

Point source FOV data was collected in the MIC1 collimator with SEBB configuration (see

Figure 11) using the MIC1 pointing mirror to steer a point source in a grid pattern across the SOFIE detectors. Detailed point source FOV data collection procedures were followed [10], [11]. Data collected during this test were used to generate the calibration parameters shown in Table 13.

Table 13. Field-Of-View Calibration Parameters

Calibration Parameter	Symbol	Calibration Plan (SDL/04-052a) Para-
Effective field of view	Ωeff_d	3.1.2
Detector coalignment	$\Delta\theta_d$	3.1.2

The SEBB was heated to 2608 K and observed through 0.022-inch and 0.044-inch diameter MIC1 apertures for on-axis and off-axis FOV measurements, respectively. These apertures were selected to under-fill the SOFIE FOV, while providing acceptable SNR.

Point source FOV data collection grids are described in Table 14. Scans were made at fine resolution (0.1 mrad) in the vertical or elevation direction (across the FOV long axis), repeated at multiple horizontal locations giving a coarse resolution (0.5 mrad) azimuth measurement. An additional fine resolution (0.2 mrad) line of azimuth data was collected at one value of vertical displacement centered on the boresight.

Table 14. Point Source Field-Of-View Data Collection Grid Description

FOV Type	Aperture Diameter	Collection Axis	Grid Steps	Grid Dimensions arcmin (mrad)	Step Size arcmin (mrad)
On-Axis FOV	0.0224”	Elevation	7 X 17	10.31 x 5.5 (3.0 x 1.6)	1.72 x 0.344 (0.5 x 0.1)
		Fine Azimuth	21 X 1	13.75 (4.0)	0.688 (0.2)
Off-Axis FOV	0.0447”	Elevation	6 X 15	17.2 x 51.6 (5.0 x 15)	3.44 x 3.44 (1.0 x 1.0)

Each measurement consisted of an approximate 1200 count (60 sec) sample average at a unique horizontal and vertical position. Background measurements were taken periodically during the grid collection by collecting a 1200 count sample with the MIC1 aperture closed.

5.1.2.1. Point Source FOV Map

Data processing consisted of background subtraction and peak normalization to 1.0 for each band. Spectral bands 3 through 16 all showed significant response to the SEBB. Field-of-view for the UV channel consisting of bands 1 and 2 will be reported separately (refer to section TBD). For illustratioin, point source FOV contour plots are shown for band 3 at cold, nominal, and warm science operating temperature in Figure 47 to Figure 49. Contour values are listed in each plot (data are peak normalized to 1).

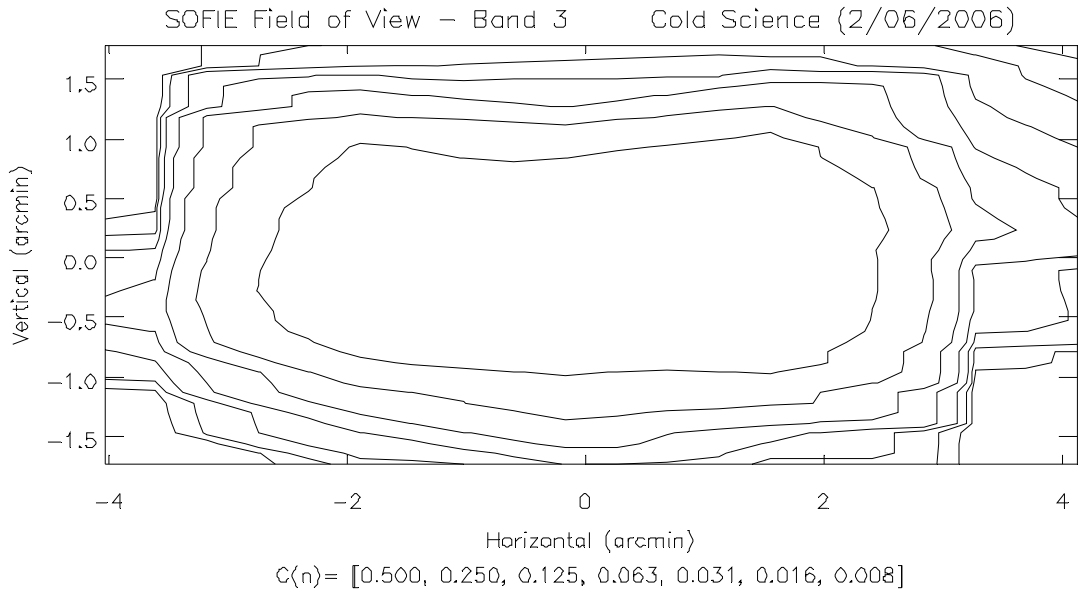

Figure 47. Band 3 FOV (Cold Science)

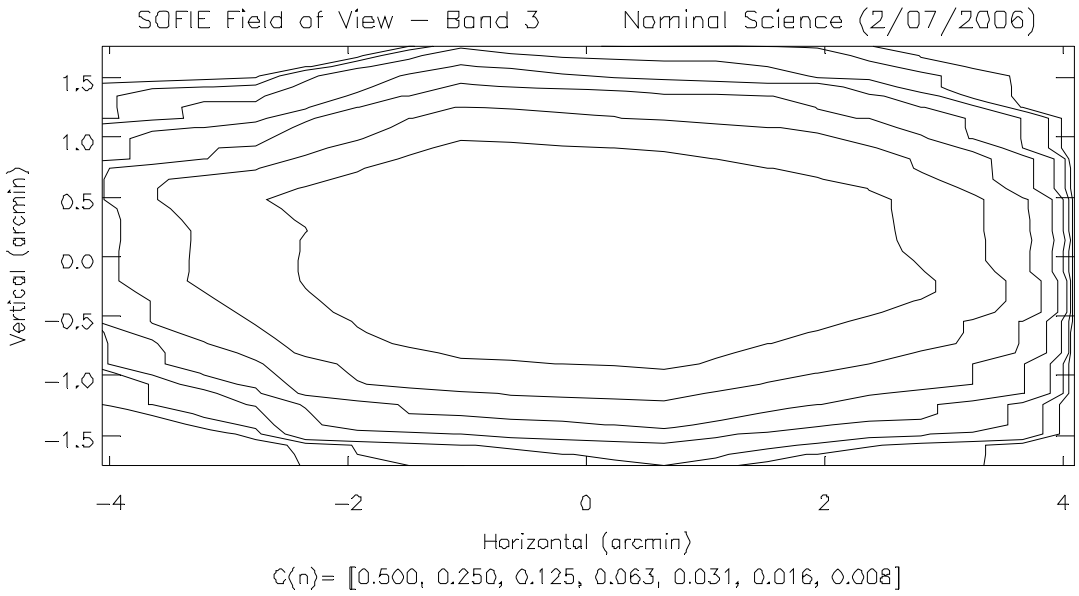

Figure 48. Band 3 FOV (Nominal Science)

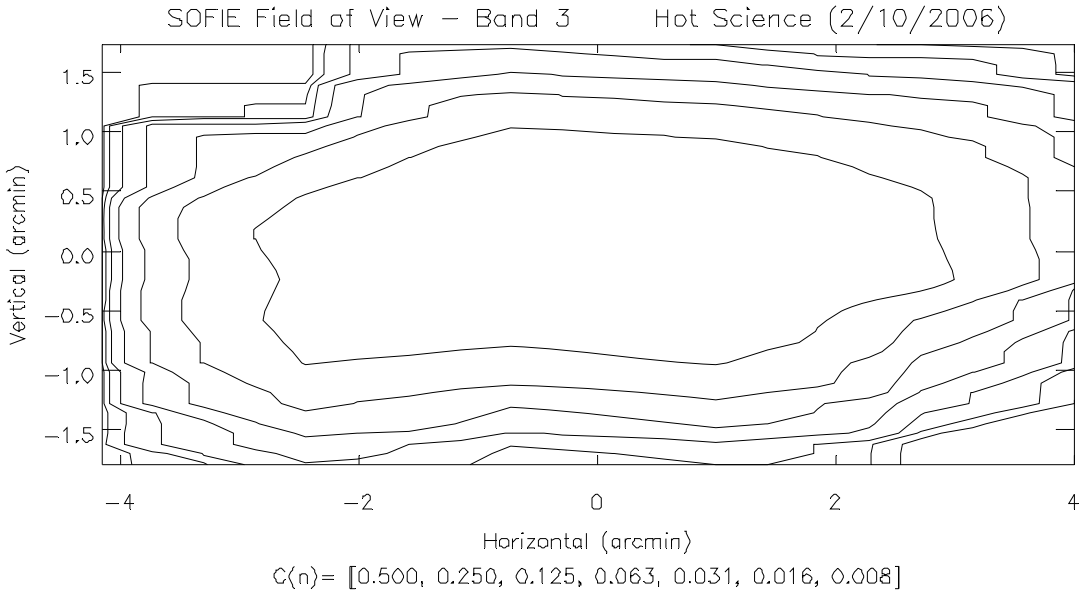

Figure 49. Band 3 FOV (Warm Science)

Instrument operating temperature was not observed to have any measurable effect on FOV shape or position. Any change in FOV for different temperatures appeared to be random, or could be attributed to GSE configuration.

Figure 50 to Figure 52 show the respective cold, nominal, and warm science temperature vertical FOV from horizontally averaged data. Figure 53 to Figure 55 plot the fine step horizontal data.

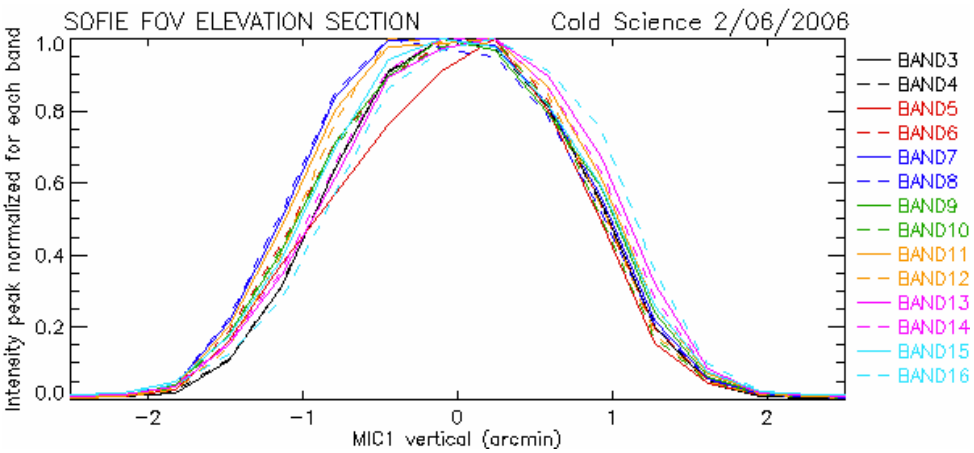

Figure 50. Cold Science FOV Vertical Profile (Bands 3-16)

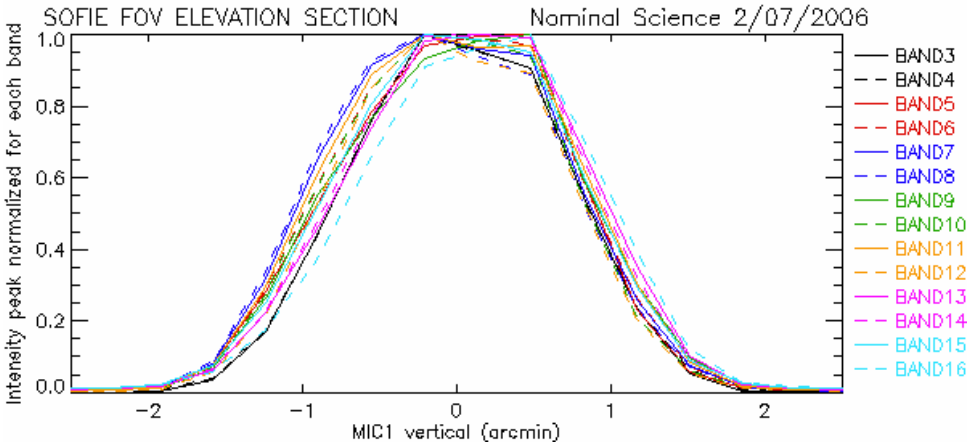

Figure 51. Nominal Science FOV Vertical Profile (Bands 3-16)

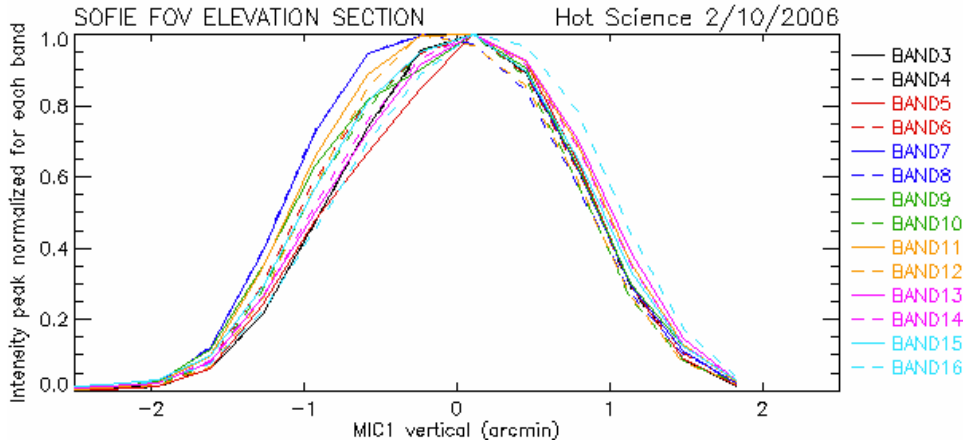

Figure 52. Warm Science FOV Vertical Profile (Bands 3-16)

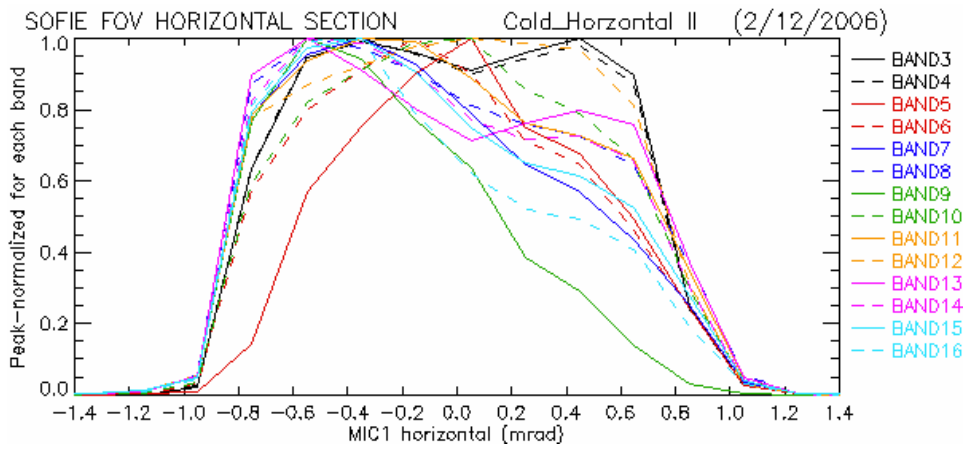

Figure 53. FOV Horizontal Profile (Cold Science)

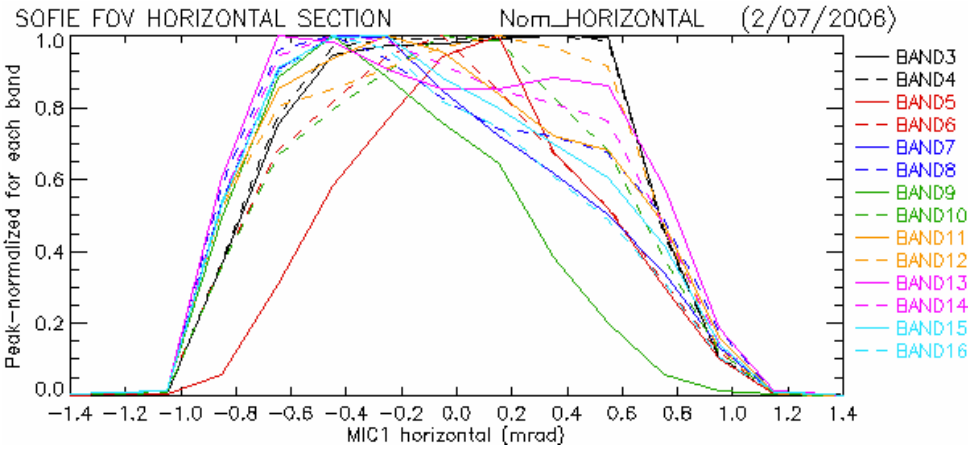

Figure 54. FOV Horizontal Profile (Nominal Science)

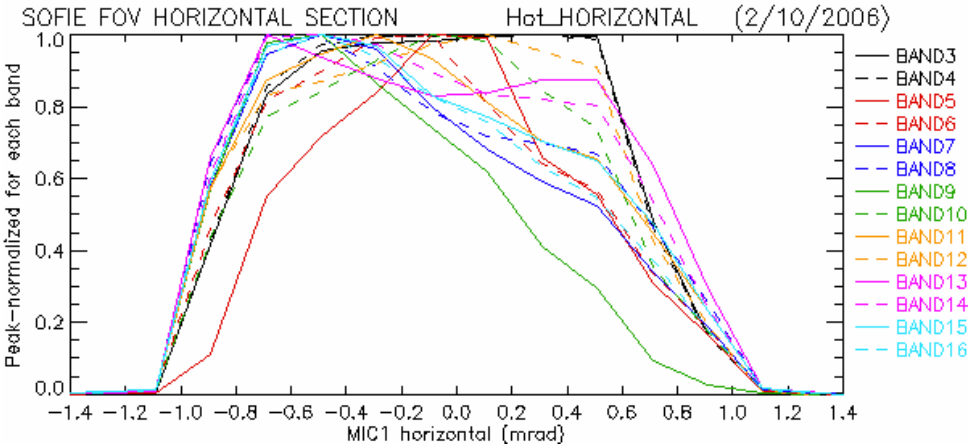

Figure 55. FOV Horizontal Profile (Warm Science)

5.1.2.2. Point Source FOV Summary

For convenience, the Band 3 FOV centroid was used as a point of reference for all bands. The offset from the FOV centroid for the other bands to the band 3 FOV centroid is summarized in Table 15.

Table 15. SOFIE FOV Centroid Offset (Band 3 Reference)

Chan.	Band / Target	Vertical Centroid Offset (arcmin)			Horizontal Centroid Offset (arcmin)		
		Cold	Nom	Warm	Cold	Nom	Warm
1	1 / O_3 s						
	2 / O_3 w						
2	3 / PMC	N/A	N/A	N/A	N/A	N/A	N/A
	4 / PMC	0.00	0.00	0.01	-0.02	-0.04	-0.01
3	5 / H_2O w	-0.02	-0.03	0.02	0.07	0.18	0.25
	6 / H_2O s	-0.05	-0.05	-0.04	-0.15	-0.22	-0.15
4	7 / CO_2 s	-0.08	-0.08	-0.09	-0.36	-0.44	-0.37
	8 / CO_2 w	-0.10	-0.10	-0.12	-0.22	-0.27	-0.21
5	9 / PMC	-0.03	0.00	-0.05	-0.77	-0.85	-0.81
	10 / PMC	-0.05	-0.06	-0.05	-0.02	-0.06	0.01
6	11 / CH_4 s	-0.04	-0.04	-0.04	-0.16	-0.21	-0.13
	12 / CH_4 w	-0.05	-0.05	-0.05	0.00	-0.09	-0.01
7	13 / CO_2 s	0.05	0.04	0.04	-0.09	-0.12	-0.04
	14 / CO_2 w	0.02	0.02	0.01	-0.19	-0.21	-0.11
8	15 / NO w	-0.02	-0.02	-0.03	-0.26	-0.29	-0.21
	16 / NO s	0.10	0.10	0.08	-0.38	-0.42	-0.36

The mean FOV centroid offset for cold, nominal, and warm science operating temperatures is shown in Table 16, with uncertainty given by the standard deviation of the three measurements.

Table 16. SOFIE FOV Centroid Mean Offset and Uncertainty (Band 3 Reference)

Chan.	Band / Target	Elevation		Azimuth	
		Mean Centroid Offset (arcmin)	Uncertainty (arcmin)	Mean Centroid Offset (arcmin)	Uncertainty (arcmin)
1	1 / O_3 s				
	2 / O_3 w				
2	3 / PMC	N/A	N/A	N/A	N/A
	4 / PMC	0.00	0.01	-0.02	0.02
3	5 / H_2O w	-0.01	0.03	0.17	0.09
	6 / H_2O s	-0.05	0.01	-0.17	0.04
4	7 / CO_2 s	-0.08	0.01	-0.39	0.04
	8 / CO_2 w	-0.11	0.01	-0.23	0.03
5	9 / PMC	-0.03	0.03	-0.81	0.04

	10 / PMC	-0.05	0.01	-0.02	0.04
6	11 / CH_4 s	-0.04	0.00	-0.17	0.04
	12 / CH_4 w	-0.05	0.00	-0.03	0.05
7	13 / CO_2 s	0.04	0.01	-0.08	0.04
	14 / CO_2 w	0.02	0.01	-0.17	0.05
8	15 / NO w	-0.02	0.01	-0.25	0.04
	16 / NO s	0.09	0.01	-0.39	0.03

On-axis point source FOV data were used to calculate field-of-view width for each band. The reported vertical FOV dimensions are based on averages of multiple vertical scans within the horizontal half-width of these data. The full width at half maximum (FWHM) of the point source FOV for each channel was determined by calculating the mean FOV response for up and down scans, and determining the width of the central lobe at half the peak value. The resulting FWHM FOV for each channel at each of the three operating temperatures is listed in Table 17.

Table 17. Field-Of-View Width

Chan.	Band / Target	FWHM Vertical (arcmin) Required: 1.8			FWHM Horizontal (arcmin) Required: 6.0		
		Cold	Nom	Warm	Cold	Nom	Warm
1	1 / O_3 s						
	2 / O_3 w						
2	3 / PMC	1.92	1.75	1.81	5.65	4.80	5.60
	4 / PMC	1.91	1.74	1.81	5.64	4.81	5.61
3	5 / H_2O w	1.88	1.87	1.97	4.42	3.42	4.58
	6 / H_2O s	2.05	1.92	1.97	5.00	4.24	5.18
4	7 / CO_2 s	2.16	1.98	2.11	4.99	4.49	5.25
	8 / CO_2 w	2.17	1.93	2.04	5.76	5.14	5.81
5	9 / PMC	2.05	1.92	2.01	3.55	3.51	4.12
	10 / PMC	2.00	1.85	1.88	5.49	4.53	5.35
6	11 / CH_4 s	2.19	1.98	2.09	5.70	5.03	5.70
	12 /CH_4 w	2.03	1.78	1.89	5.78	5.05	5.76
7	13 / CO_2 s	2.07	1.86	1.94	5.87	5.31	6.24
	14 /CO_2 w	2.04	1.85	1.93	5.67	5.05	5.99
8	15 / NO w	2.05	1.86	1.96	5.40	4.83	5.79
	16 / NO s	2.04	1.82	1.99	4.42	4.42	5.36

The mean and standard deviation of the FWHM at the three operating temperatures are presented in Table 18.

Table 18. SOFIE FOV Mean FWHM and Uncertainty

Chan.	Band / Target	Elevation		Azimuth	
		Mean FWHM (arcmin) Req'd: 1.8	Uncer-tainty (arcmin)	Mean FWHM (arcmin) Req'd: 6.0	Uncer-tainty (arcmin)
1	1 / O_3 s				
	2 / O_3 w				
2	3 / PMC	1.83	0.09	5.35	0.42
	4 / PMC	1.82	0.09	5.35	0.83
3	5 / H_2O w	1.91	0.06	4.14	0.63
	6 / H_2O s	1.98	0.07	4.81	0.40
4	7 / CO_2 s	2.08	0.09	4.91	0.50
	8 / CO_2 w	2.05	0.12	5.57	1.06
5	9 / PMC	1.99	0.07	3.73	0.86
	10 / PMC	1.91	0.08	5.12	0.45
6	11 / CH_4 s	2.09	0.11	5.48	0.36
	12 / CH_4 w	1.90	0.13	5.53	0.42
7	13 / CO_2 s	1.96	0.11	5.81	0.44
	14 / CO_2 w	1.94	0.10	5.57	0.45
8	15 / NO w	1.96	0.10	5.34	0.57
	16 / NO s	1.95	0.12	4.73	0.66

The mean FOV vertical dimension ranges from 1.82 to 2.09 arcmin, and the horizontal dimension ranges from 3.73 to 5.81 arcmin. The average FOV dimensions for all bands 3 through 16 measured at nominal science temperature were 1.96 arcmin vertical by 5.10 arcmin horizontal (based on the high resolution azimuth scans). These values vary slightly from requirements of 1.8 arcmin in elevation and 6.00 arcmin in azimuth, but easily satisfy science requirements.

Off-axis data were used to calculate integrated FOV response. Off-axis FOV data were scaled to on-axis using the areas of the apertures used in each data collection. The integrated response over one FOV width from center was determined using the reported FWHM for each band as the FOV width. Table 19 summarizes the integrated contribution within the specified area for each band.

Table 19. Field-Of-View Off-Axis Contribution

Chan.	Band / Target	Total Vertical Width (arcmin) Required: 3.6 Nominal Science	Contribution within one FOV width from center Required: 99%
1	1 / O_3 s		
	2 / O_3 w		
2	3 / PMC	3.42	98%
	4 / PMC	3.41	98%
3	5 / H_2O w	3.71	98%

	6 / H_2O s	3.81	99%
4	7 / CO_2 s	3.89	99%
	8 / CO_2 w	3.85	99%
5	9 / PMC	3.78	99%
	10 / PMC	3.69	98%
6	11 / CH_4 s	3.95	99%
	12 /CH_4 w	3.55	98%
7	13 / CO_2 s	3.71	98%
	14 /CO_2 w	3.69	98%
8	15 / NO w	3.70	97%
	16 / NO s	3.58	96%

There are 5 channels with a the 99% contribution within the specified area requirement, while 9 channels each have a contributions slightly less than the 99% requirement. No significant off-axis contribution was found for any band 3-16. The response within the FOV width from center proved to be the only area of significant contribution. Figure 56 shows an example plot curve including the out-of-band contribution on a logarithic scale.

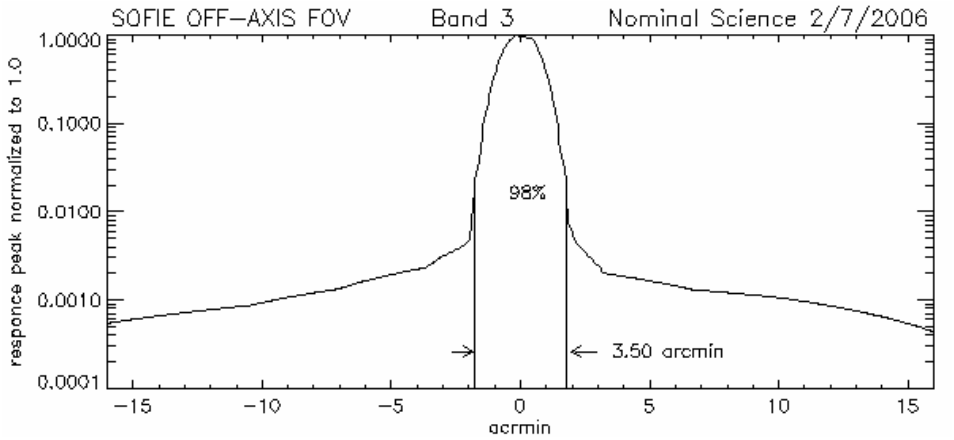

Figure 56. SOFIE Integrated FOV Contribution

5.1.3. Field of View Mismatch

Point source FOV data were also used to characterize field of view mismatch (FOVMM) between band pairs. While the SOFIE instrument was designed to minimize field-of-view mismatch, changes to the SOFIE instrument to reduce detector nonlinearity by overfilling the detectors caused an anticipated increase in FOVMM. Figure 57 shows the FOV elevation profile using horizontaly averaged data before the instrument changes. Figure 58 shows similar data following instrument changes to overfill the detectors.

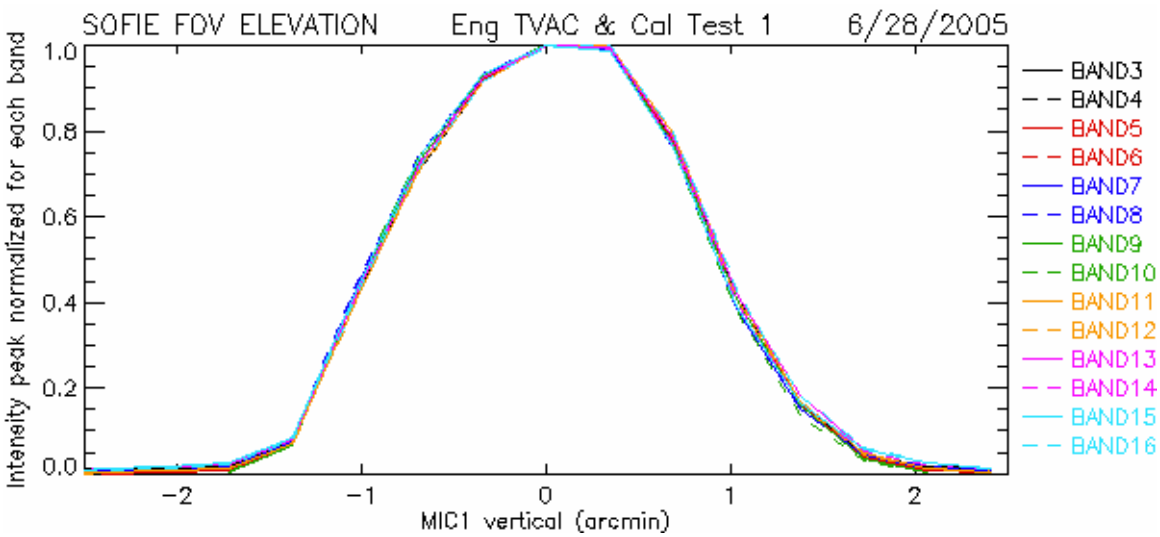

Figure 57. FOV Elevation Profile (Pre-Overfill)

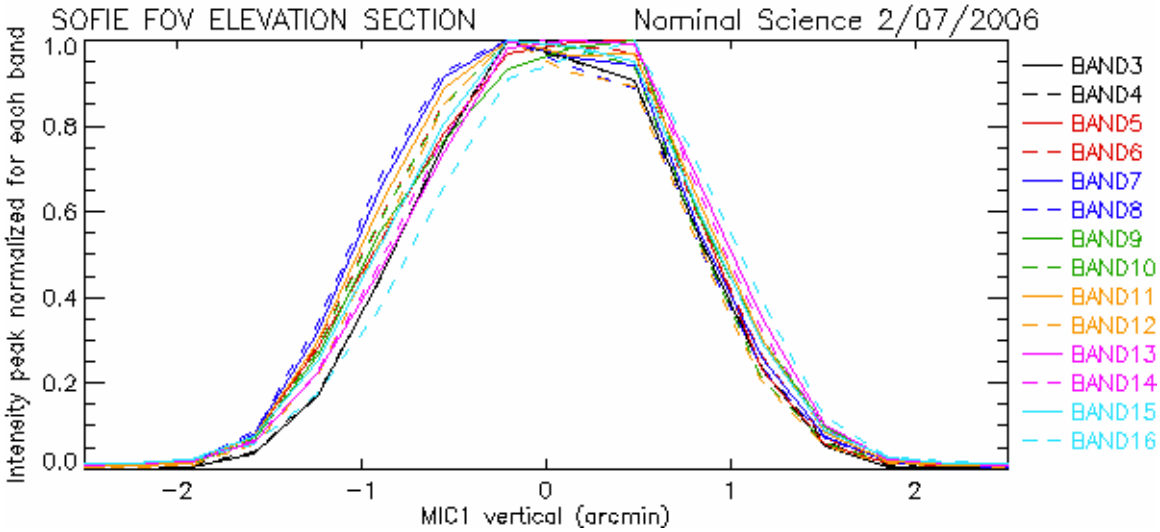

Figure 58. Field-Of-View Profile (Post-overfill)

The plots show the obvious increase in FOV mismatch introduced by positioning the detectors to be overfilled. Optical modeling has confirmed that the increased mismatch results from the changes in detector location to correct nonlinearity. Bands 3 and 4 of channel 2, which did not need to be corrected for nonlinearity, have minimal mismatch as will be shown later.

FOVMM for all bands is characterized by normalizing channel pairs to have equal integrated responses in elevation. For convenience the intensities are normalized so the band with the greatest maximum response is peak normalized to 1.0. The second band is subtracted from its channel companion to give the reported FOVMM.

Figure 59 to Figure 65 plot channel pairs and the FOVMM between pairs for channels 2 through 8 at nominal science temperature.

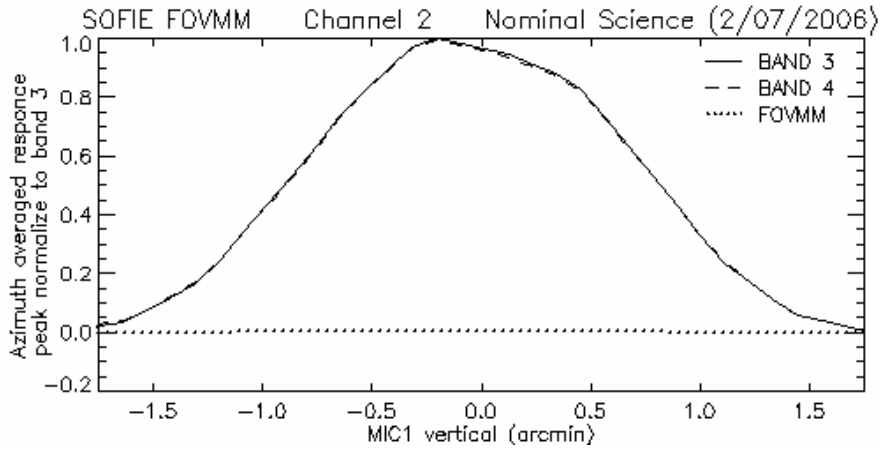

Figure 59. Field-Of-View Mismatch (Bands 3 & 4)

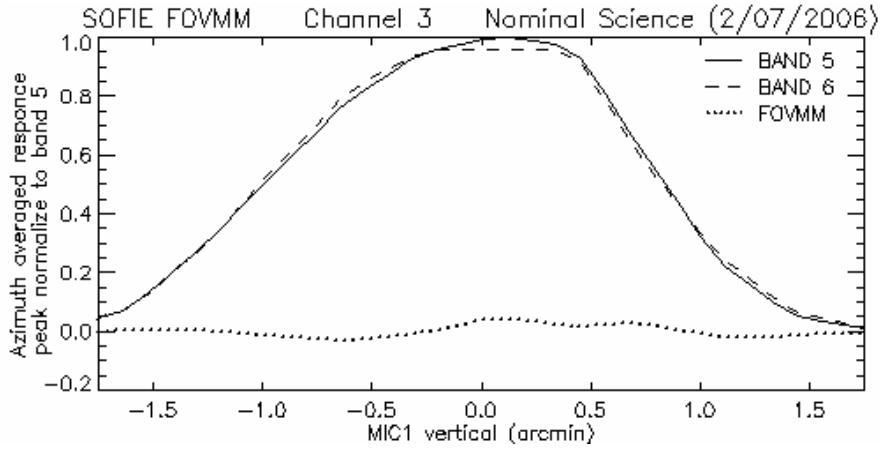

Figure 60. Field-Of-View Mismatch (Bands 5 & 6)

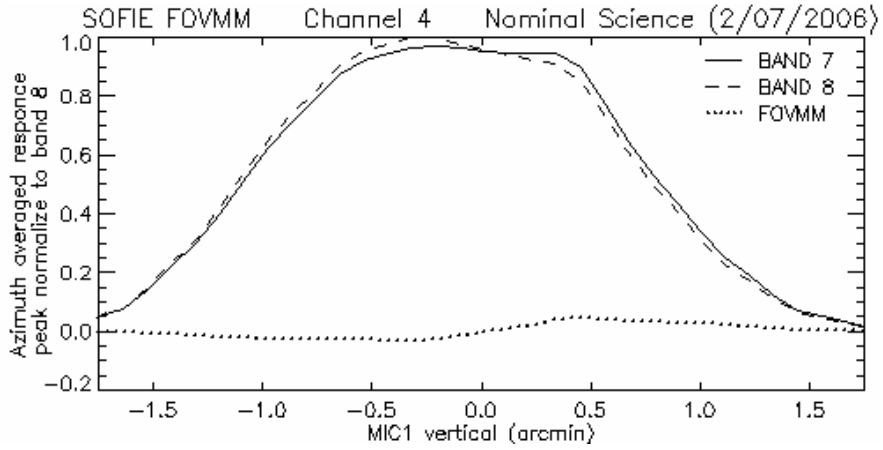

Figure 61. Field-Of-View Mismatch (Bands 7 & 8)

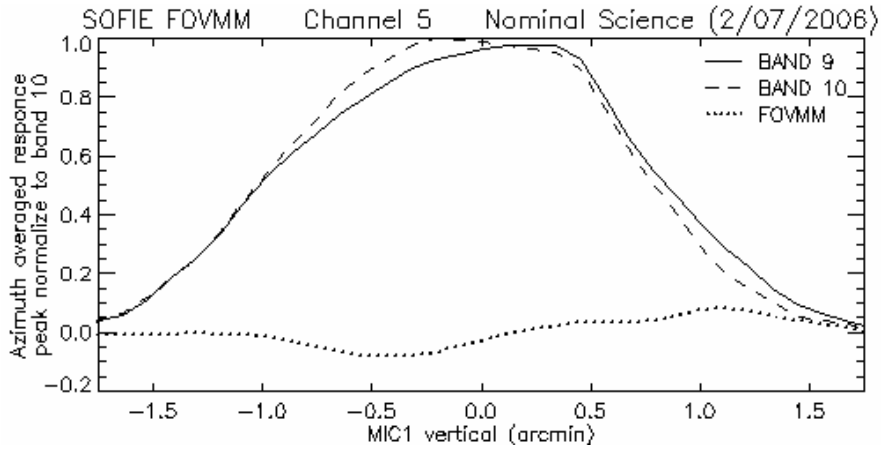

Figure 62. Field-Of-View Mismatch (Bands 9 & 10)

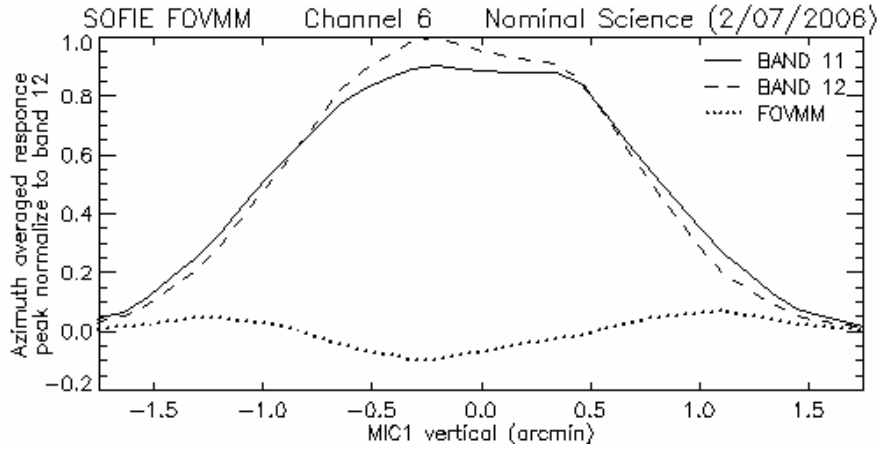

Figure 63. Field-Of-View Mismatch (Bands 11 & 12)

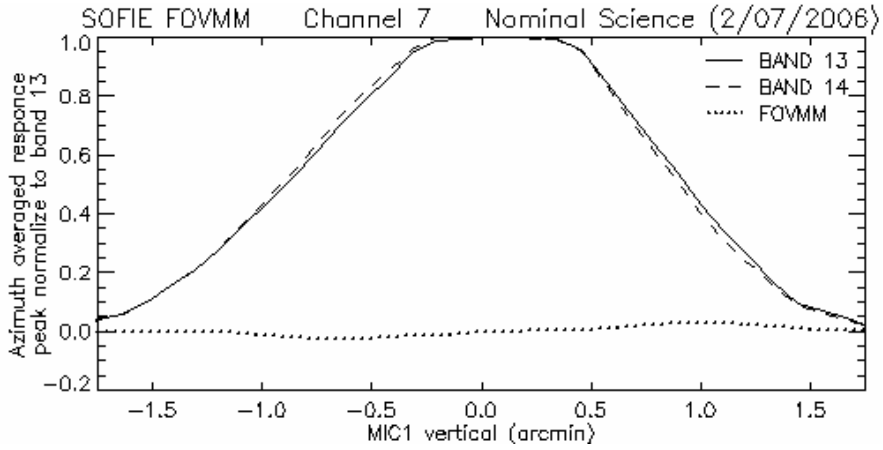

Figure 64. Field-Of-View Mismatch (Bands 13 & 14)

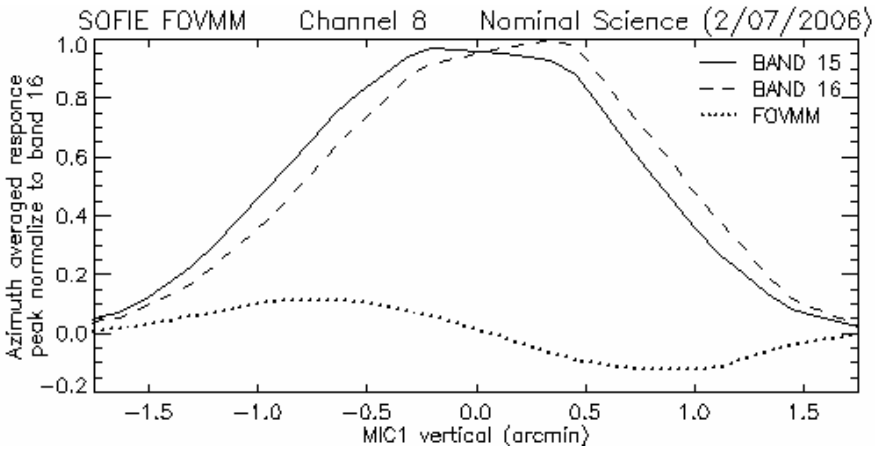

Figure 65. Field-Of-View Mismatch (Bands 15 & 16)

To investigate possible FOVMM dependencies on temperature, Figure 66 and Figure 67 show example FOVMM for bands 15 and 16 at cold and warm operating temperatures, respectivly, which can be compared to Figure 65 for the nominal case.

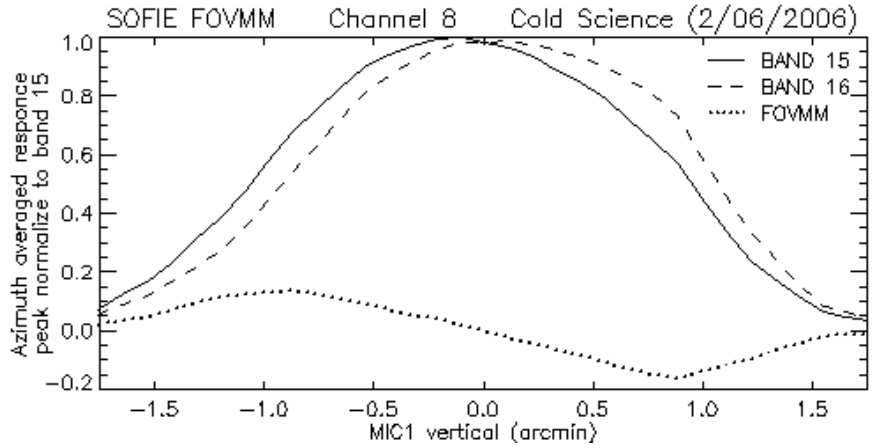

Figure 66. Cold Science FOVMM (Bands 15 & 16)

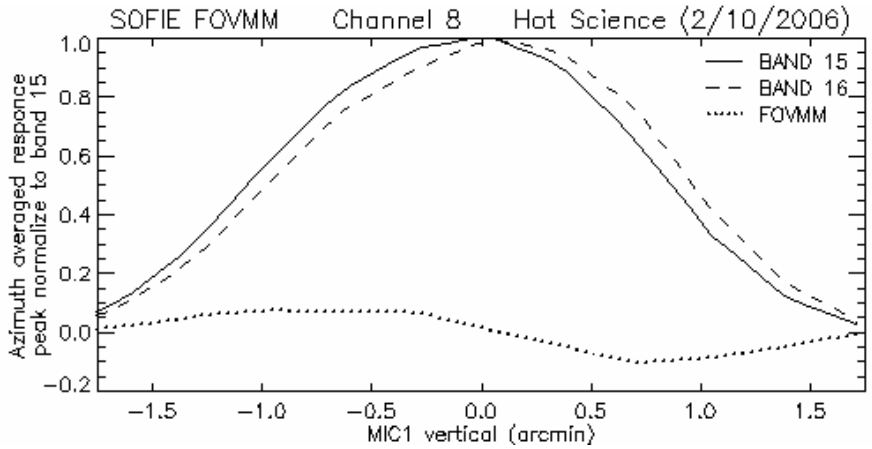

Figure 67. Warm Science FOVMM (Bands 15 & 16)

The shape and postion of the FOVMM appears to remain constant over cold, nominal, and warm science temperatures. Similar results were shown for all channels as summarized in Table 20, where the maximum FOVMM for each channel pair is shown.

Table 20. Field-Of-View Mismatch

Channel	Bands / Target	FOVMM Maximum Intensity (arcmin)		
		Cold	Nom	Warm
1	1, 2 / O_3			
2	3, 4 / PMC	0.00	0.01	0.00
3	5, 6 / H_2O	0.09	0.04	0.10
4	7, 8 / CO_2	0.03	0.05	0.05
5	9, 10 / PMC	0.05	0.09	0.10
6	11, 12 / CH_4	0.08	0.10	0.10
7	13, 14 / CO_2	0.04	0.03	0.03
8	15, 16 / NO	0.16	0.12	0.11

5.1.4. Knife Edge FOV

Field of view measurements were also attempted using a knife edge technique. A knife edge (step function) illumination profile moving across the SOFIE detectors was created using an opaque screen placed just in front of the SOFIE instrument, with MIC1 collimator and UV lamp sources. Knife edge test data were processed to look for detector misalignments as a lead or lag in the signal attenuation of one detector relative to the other.

5.1.4.1. MIC1 with SEBB Knife Edge FOV

For translation stage knife edge FOV tests, the SOFIE instrument was installed in the test chamber and cooled to nominal science temperature, and an opaque screen was mounted on a translation stage between the test chamber and the MIC1 collimator. The SEBB source was placed at the MIC1 entrance port. The SOFIE pointing mirror was fixed at nominal orientation, and the MIC1 pointing mirror was positioned to illuminate the detector under test. Measurements were made as the knifed edge was moved in 0.2 in increments in azimuth or elevation to block and then clear the collimated portion of the MIC1 output. A conceptual drawing of the MIC1 with SEBB source knife edge configuration is shown in Figure 68.

Figure 68. MIC1 with SEBB Knife Edge configuration

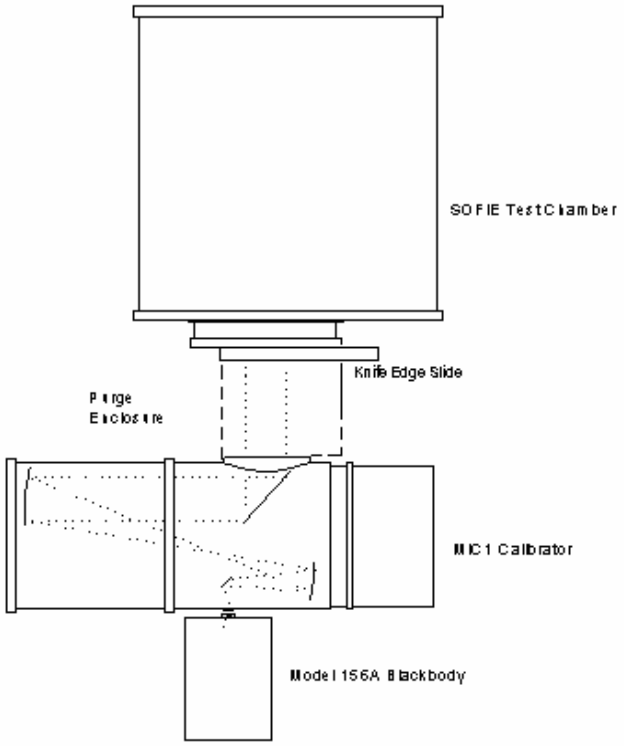

Field-of-view was determined by calculating the derivative of the raw data recorded as the knife edge blocked or cleared the SOFIE aperture. Knife edge FOV profiles for elevation and azimuth scans are shown in Figure 69 and Figure 70, respectively. The data are shown are the average of scans where the SOFIE aperture was both blocked and cleared.

Figure 69. Elevation Translation Stage Knife Edge FOV Profile

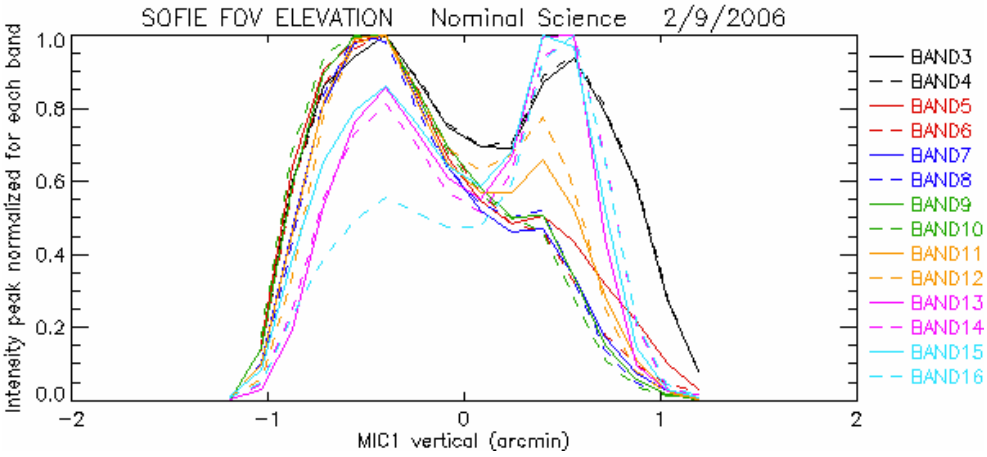

Figure 70. Azimuth Translation Stage Knife Edge FOV Profile

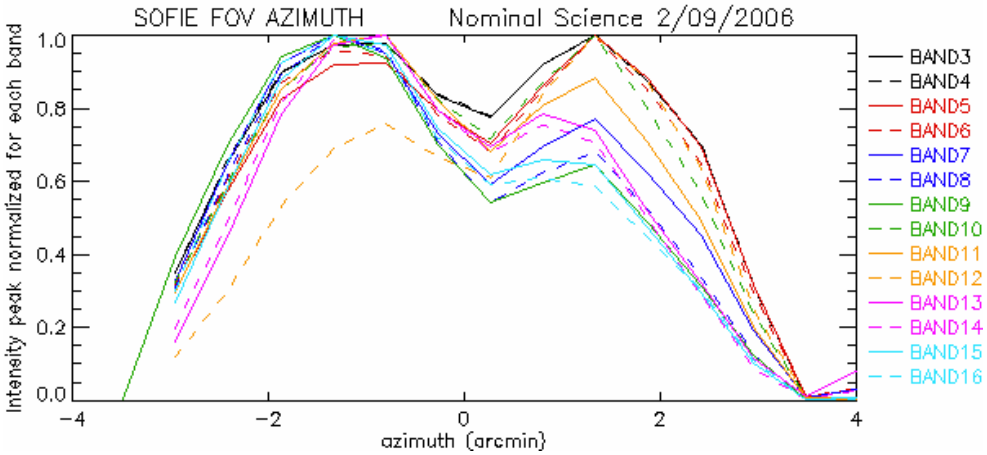

5.1.4.2. UV Knife Edge

The MIC1 collimator with the SEBB source did not provide enough UV throughput to stimulate bands 1 and 2 for FOV measurements. Further testing using a separate UV lamp was required to provide data for these bands. The lamp was placed to illuminate the SOFIE aperture, and an opaque screen was mounted on a translation stage between the lamp and the SOFIE aperture. Data recorded in Band 3 during the UV knife edge FOV measurements were used to relate UV knife edge measurements for bands 1 and 2, to the knife edge FOV measurements discussed in section 5.1.4.1, covering bands 3 to 16. Plots showing elevation and azimuth FOV contours measured during UV knife edge tests, for bands 1, 2, and 3, are shown in Figure 71 and Figure 72.

Figure 71. Elevation UV Knife Edge Profile

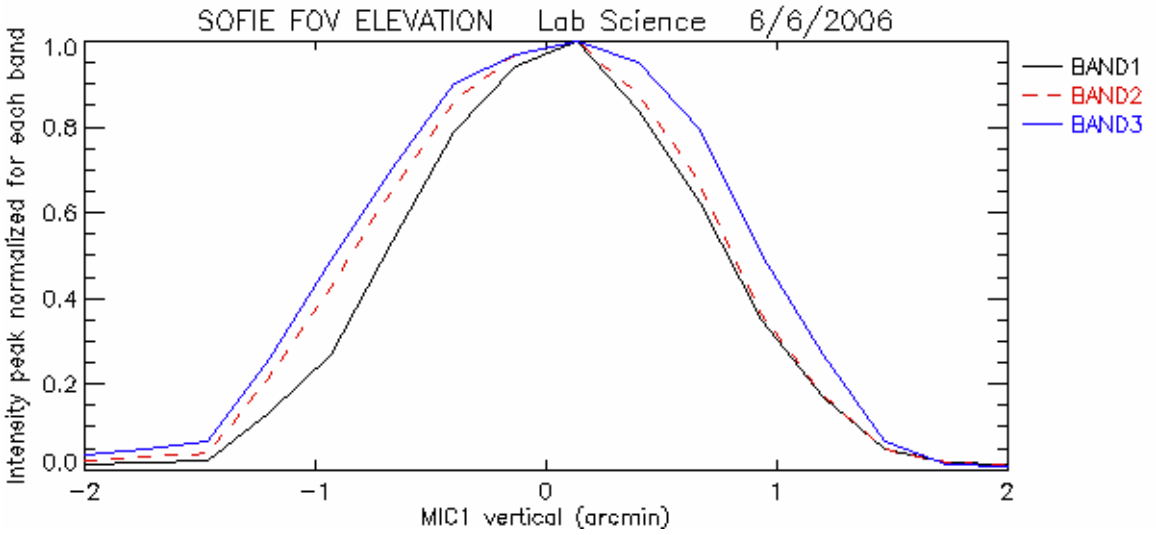

Figure 72. Azimuth UV Knife Edge Profile

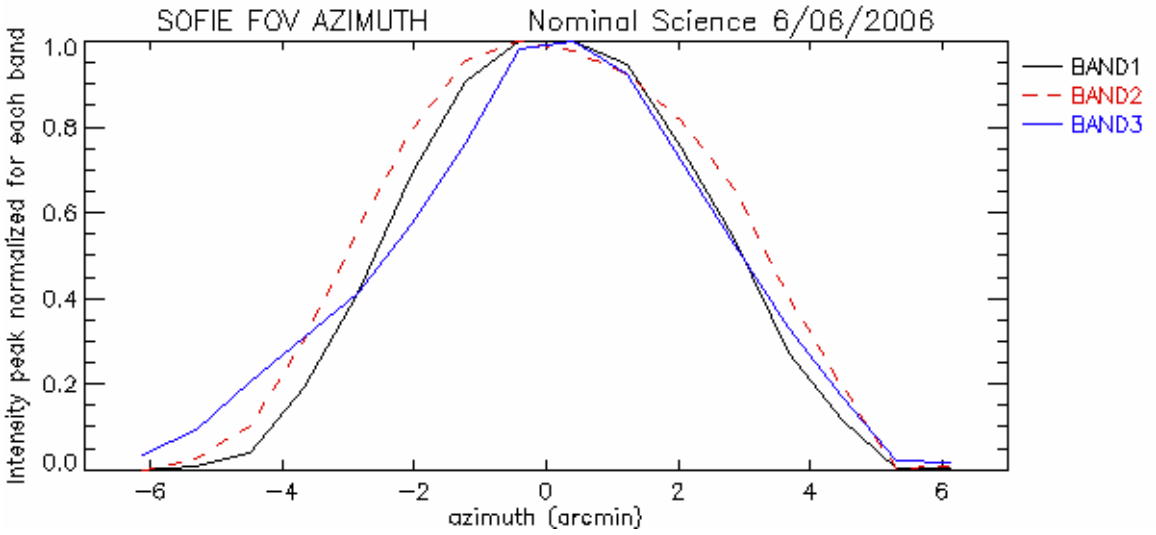

5.1.4.3. Knife Edge FOV Summary

FOV dimensions from knife edge data are tabulated in Table 21. The location of the FOV centroid, relative to band 3, from knife edge FOV data, is reported in Table 22.

Table 21. Knife Edge FOV Summary

Channel	Band / Target	Elevation FOV (FWHM, arcmin)	Azimuth FOV (FWHM, arcmin)
1	1 / O_3 s	1.44	7.16
	2 / O_3 w	1.63	8.93
2	3 / PMC	1.83	5.35
	4 / PMC	1.84	5.36
3	5 / H_2O w	1.38	4.62
	6 / H_2O s	1.57	5.12
4	7 / CO_2 s	1.46	5.15
	8 / CO_2 w	1.63	5.34
5	9 / PMC	1.61	4.00
	10 / PMC	1.59	5.02
6	11 / CH_4 s	1.78	5.49
	12 / CH_4 w	1.73	4.85
7	13 / CO_2 s	1.64	5.27
	14 / CO_2 w	1.80	5.34
8	15 / NO w	1.79	5.28
	16 / NO s	1.30	5.05

Table 22. Knife Edge FOV Offset Summary

Channel	Band / Target	FOV Elevation Offset (arcmin)	FOV Azimuth Offset (arcmin)
1	1 / O_3 s	0.04	0.24
	2 / O_3 w	0.02	0.19
2	3 / PMC	n/a	n/a
	4 / PMC	0.01	-0.02
3	5 / H_2O w	-0.19	0.15
	6 / H_2O s	-0.19	-0.13
4	7 / CO_2 s	-0.22	-0.41
	8 / CO_2 w	-0.22	-0.28
5	9 / PMC	-0.25	-0.82
	10 / PMC	-0.22	0.06
6	11 / CH_4 s	-0.11	-0.17
	12 / CH_4 w	-0.11	0.23
7	13 / CO_2 s	0.09	-0.19
	14 / CO_2 w	0.04	-0.20
8	15 / NO w	-0.07	-0.32
	16 / NO s	0.16	-0.46

5.1.5. Linearity Correction

Initial calibration of the SOFIE instrument revealed unacceptable nonlinearity in bands 5 - 16. This behavior was traced to nonlinear behavior in HgCdTe detectors when the irradiance (flux per area) on the detectors exceeds a certain level [12]. Changes to the instrument design were introduced to reduce the non-linearity to acceptable levels, and provide a means for expanded characterization of the remaining non-linearity. These changes involved reducing the irradiance on detectors 5 - 16 by adjusting the detector position so that the detectors are overfilled rather than underfilled, and adding a neutral-density (ND) filter in the optical path to further reduce flux on the detectors [13]. The ND filter provided the additional advantage that by testing before installation of the ND filter, measurements could be made at higher levels in the dynamic range.

SOFIE linearity characterization measurements were made for each individual spectral band at nominal instrument operating temperatures. The SOFIE pointing mirror was fixed at nominal orientation. Linearity characterization was performed prior to installation of the nonlinearity mitigation ND filter, to allow linearity characterization higher in the dynamic range than would be the case if these tests were performed after installation of the ND filter.

5.1.5.1. Small-Signal Nonlinearity Review

Initial nonlinearity characterization tests were performed using a small-signal method. This approach combines a chopped small signal of constant amplitude with a constant large signal, to measure the response to the small signal throughout the range of response provided by different levels of large signal. SEBB blackbody temperatures were chosen to provide the necessary large signal response levels using MIC1. The small signal was provided by a second blackbody, with a lens to expand and collimate the available beam, folded into the optical path using a flat fold mirror. A fold mirror was chosen to combine the signals, rather than the standard approach of an integrating sphere, to avoid the signal losses that would be introduced by an integrating sphere.

Data acquired with this approach were invalidated by varying irradiance distributions on the detectors, resulting from non-uniform combination of the small and large signals by means of the fold mirror. The non-uniform irradiance distribution on the detectors introduced additional nonlinearity effects in the non-linearity characterization data, and made the result inconsistent with other measurement data. The small signal approach was ultimately rejected in favor of a small-attenuator approach which yielded a more uniform irradiance distribution on the detectors.

5.1.5.2. Small Attenuator Nonlinearity Method

The nonlinear response of PV and PC MCT detectors in the infrared was recently investigated [12]. This work showed that response nonlinearity was a function of irradiance rather than total radiant power on the detector. Response nonlinearity was observed for irradiances greater than about 0.05 mW cm^{-2}. SOFIE detector irradiances after beam overfilling and installation of the ND filter are between 0.45 and 4.5 mW cm^{-2}, and thus still within the expected nonlinear regime.

The response of a nonlinear system to a given radiance level, I, can be written as the product of the linear response and a nonlinear term, f_{NL},

$$N_M = R\, I\, f_{NL}(I) \tag{8}$$

where N_M is the measured signal in counts, R is the response constant, and the response of a linear system is $N_L = R\,I$. Because a given radiance level, I_i, corresponds to the reading $N_{M,i}$, the nonlinear term expressed as a function of either $N_{M,i}$ or I_i are equivalent, $f_{NL}(N_{M,i}) = f_{NL}(I_i)$. Thus, (8) can be rewritten in terms of the linear response, N_L, and $f_{NL}(N_M)$.

$$N_M = N_L\, f_{NL}(N_M) \tag{9}$$

The goal of the linearity calibration is to determine $f_{NL}(N_M)$ and thus convert N_M to the response of an ideal linear system, $N_L = N_M / f_{NL}(N_M)$.

Response linearity is generally calibrated by stimulating a sensor over its dynamic range while causing a small signal change of known magnitude [12], [14]. At high radiance levels, departure of the measured response from that expected due to the induced small signal change is due to response nonlinearity. In the approach used for SOFIE calibration, a CaF_2 window (transmission $\tau_W \approx 0.93$) was chopped through the incoming beam from a blackbody source. The CaF_2 window reduces the incoming radiance by a constant fraction, τ_W, and the ratio of the attenuated (N_A) and un-attenuated (N_M) signals yields a measurement of τ_W,

$$\tau_{WM} = N_A / N_M \tag{10}$$

It can be shown that τ_{WM} versus N_M is linear to a very good approximation,

$$\tau_{WM} = C_1 + C_2 N_M \tag{11}$$

Manipulation of equations (8) – (11) yields

$$f_{NL}(N_M) = 1 - C_{NL} N_M \tag{12}$$

where $C_{NL} = C_2 / (1 - C_1)$. Thus interpretation of the linearity calibration measurements is accomplished through least squares fitting of τ_{WM} versus N_M. The uncertainty in f_{NL} is determined from the statistical uncertainty in the fit parameters C_1 and C_2.

$$\frac{\delta f_{NL}}{f_{NL}} = \frac{\delta C_{NL}}{C_{NL}} = \frac{\delta C_1}{C_1} + \frac{\delta C_2}{C_2} \tag{13}$$

which are calculated during the least-squares regression to measurements of N_M versus τ_{WM}.

Response nonlinearity can also be determined from the calibration data using a boot-strap numerical approach where vectors that relate the desired linear response , N_L`, to the measured nonlinear response, $N_M$`,

$$N_L` = [N_{A1}, N_{M1}, N_{A2}, N_{M2}, \ldots\ ]$$

$$N_M` = [N_{A1}, N_{M1}, N_{A2}, N_{M2}, \ldots\ ]$$

are constructed sequentially. N_A and N_M have linear counterparts, N_{AL} and N_{ML}. Assuming that the data are sampled such that $N_{Mi} > N_{Ai-1}$, then N_{AL} can be found by interpolation on N_L` versus $N_M$`. The linear system response for the un-attenuated signal, N_{ML} is then $N_{ML} = N_{AL} / \tau_A$. Again,

τ_A is the value of C_1 from (11) determined by a least squares fit to the measurements. The vectors N_L` and $N_M$` are then incremented by the new linear response values:

$$N_L\text{`} \text{`} = [N_{A1}, N_{M1}, N_{A2}, N_{M2},\ldots, N_{ALi}, N_{MLi},\ldots]$$

$$N_M\text{`} = [N_{A1}, N_{M1}, N_{A2}, N_{M2},\ldots, N_{Ai}, N_{Mi},\ldots]$$

and the process continues over the length of the data set. In practice, a linear fit to τ_M versus N_M will smooth the data set and allow interpolation to finer spacing if needed. The primary error source in the boot-strap method is in the interpolation of N_L` versus $N_M$` to find N_{AL}. Analysis of test data indicates that interpolation errors can be virtually eliminated by fitting a third degree polynomial to N_L` versus $N_M$` using the four points immediately surrounding a given N_A.

The nonlinearity correction is then simply provided by the vectors N_L` versus $N_M$`. Alternately, the nonlinear term can be determined by

$$f_{NL}(N_M) = \frac{N_M\text{`}}{N_L\text{`}} \tag{14}$$

The boot strap method gives nearly perfect results when using synthetic data. In practice, the propagation of errors could be significant, however, smoothing of test data using (11) should mitigate this issue.

5.1.5.3. SOFIE Nonlinearity Summary

SOFIE response linearity was calibrated using the small attenuator method by stimulating the instrument over as wide a dynamic range as possible while chopping a CaF_2 window through the incoming beam. The radiation source was a solar emulator blackbody (SEBB) which achieved an effective emitting temperature of ~3000K, which equates to roughly 33% of the radiance expected from an exoatmospheric solar view on orbit. Stimulating SOFIE with the SEBB and the flight ND filter removed thus generally achieved radiance levels expected for an exoatmospheric solar view with the ND filter installed. An example calibration data time series is shown in Figure 73. An example of the measured window transmission versus response is shown in Figure 74. These results indicate the expected linear relationship in τ_M versus N_M, and a linear fit was performed to determine C_1 and C_2 and thus C_{NL}. Comparing the analytic method to the nonlinearity derived using the boot-strap method shows negligible differences in the two approaches. The calibration results for bands 5-16 are summarized in Table 23.

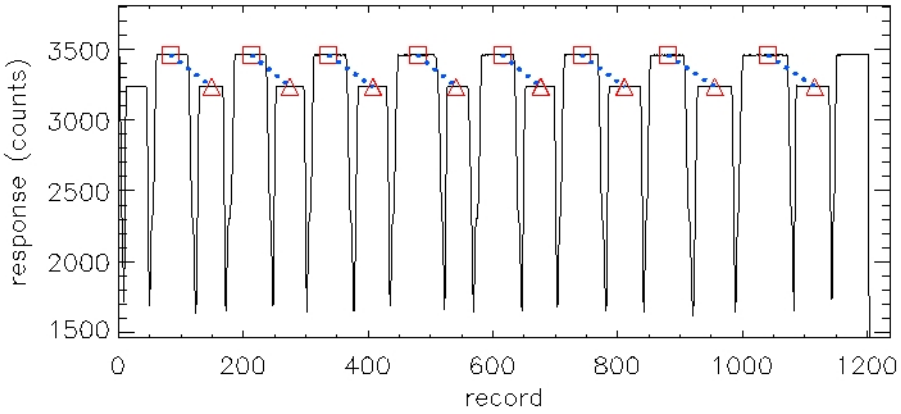

Collected in October 2005. Presence of the CaF_2 window is evident by a sharp signal reduction due to the window frame passing through the aperture followed by a plateau of lowered response. Triangles indicate the plateau-average attenuated response, N_A, and squares indicated the plateau-average un-attenuated response, N_M. Dotted lines connect pairs of N_A and N_M that were used to determine measured window transmission.

Figure 73. Small Attenuator Time Series

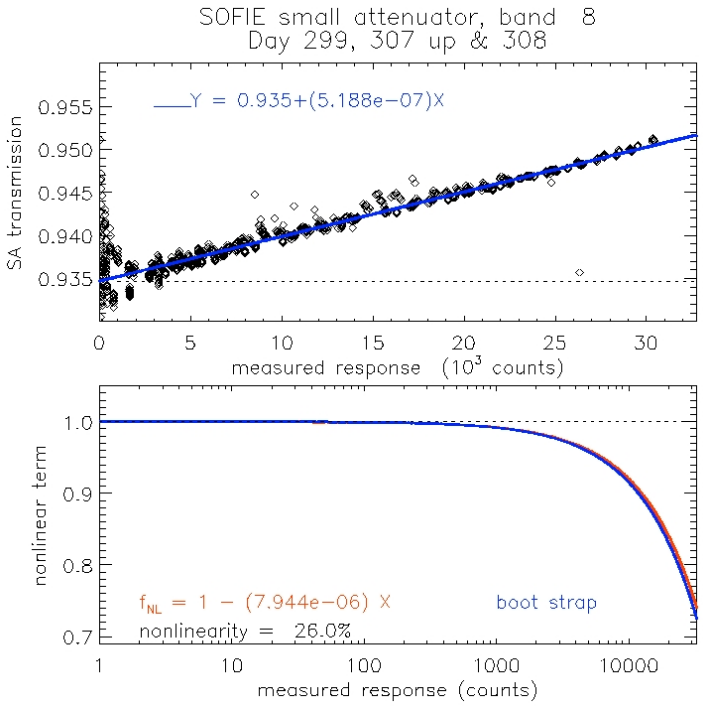

The data are for SOFIE without the flight ND filter installed using the SEBB as stimulus.

Figure 74. Linearity Calibration (band 8)

Table 23. SOFIE Nonlinearity Correction Constants

Channel	Band / Target*	Center λ (μm)	Detector	C_{NL} (counts-1) / error (%)	Nonlinearity (%) at 2^{15} counts / uncertainty (%)
1	1 / O_3 s	0.290	SiC, PV	0	0
	2 / O_3 w	0.328	SiC, PV	0	0
2	3 / PMC s	0.862	Ge, PV	0	0
	4 / PMC w	1.03	Ge, PV	0	0
3	5 / H_2O w	2.45	HgCdTe, PC	1.68 × 10-6 / 4.8	5.5 / 0.3
	6 / H_2O s	2.60		1.46 × 10-6 / 5.4	4.8 / 0.3
4	7 / CO_2 s	2.77	HgCdTe, PC	8.91 × 10-6 / 0.8	29.2 / 0.2
	8 / CO_2 w	2.94		7.94 × 10-6 / 0.7	26.0 0.2
5	9 / PMC s	3.06	HgCdTe, PC	6.63 × 10-7 / 9.3	2.2 / 0.2
	10 / PMC w	3.19		1.47× 10-6 / 4.7	4.8 / 0.2
6	11 / CH_4 s	3.37	HgCdTe, PC	1.46 × 10-6 / 4.0	4.8 / 0.2
	12 / CH_4 w	3.51		2.23× 10-6 / 2.9	7.3 / 0.2
7	13 / CO_2 s	4.25	HgCdTe, PC	4.83 × 10-6 / 4.7	15.8 / 0.7
	14 / CO_2 w	4.63		3.20 × 10-6 / 8.8	10.5 / 0.9
8	15 / NO w	4.98	HgCdTe, PC	1.75 × 10-6 / 3.0	5.7 / 0.2
	16 / NO s	5.32		2.26 × 10-6 / 3.7	7.4 / 0.3
*s denotes strong absorption band, w denotes weak band.					

The SOFIE signal conditioning electronics contain adjustable attenuators that can apply gain (G_A) from zero to one prior to digitization in each band. The response nonlinearity is a function of radiance, however, the calibration describes nonlinearity in terms of the measured response. Thus, application of the linearity calibration to real data must account for differences between G_A for a given measurement and the calibration configuration ($G_{A,cal}$):

$$f_{NL}(N_M) = 1 - C_{NL}\, N_M\, G_{A,cal} / G_A \tag{15}$$

In all laboratory calibration data presented here $G_{A,cal} = 0.83$.

The SOFIE difference signals, ΔV, are measured as $\Delta V = (V_W\, G_W - V_S\, G_S) G_{\Delta V}$, where V_W and V_S are the weak and strong band signals in volts, G_W and G_S are the weak and strong band balance attenuator settings ($0 \le G \le 1$), and $G_{\Delta V}$ is the ΔV gain. The ΔV will be corrected for nonlinearity by including nonlinearity in the modeled strong and weak band signals used to simulate ΔV.

In conclusion the response nonlinearity in SOFIE bands 5-16 exhibit response nonlinearity ranging from 2 to 30% at radiance levels consistent with an exoatmospheric solar view and was calibrated with uncertainties of less than 1%.

5.1.6. FPA / Detector Boresight Alignment

Focal plane array (FPA) to detector alignment was measured using the MIC1 collimator with the SEBB. The MIC1 open aperture was selected, and the pointing mirror was used to center the MIC1 output on the detectors, by finding limits of response in each direction and bisecting these positions. A picture of the MIC1 aperture was then recorded using an extended integration time to reveal the location of detectors relative to the FPA, as shown in Figure 75.

Figure 75. Image of MIC1 open aperture with Detectors Superimposed

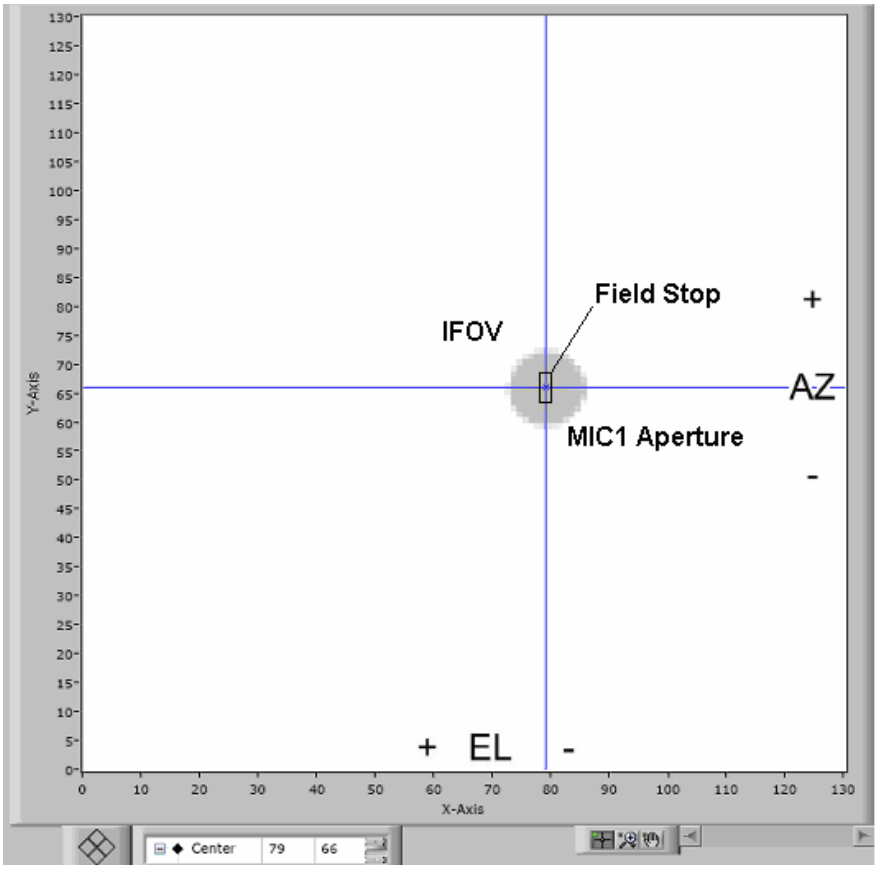

The picture indicates the detectors are located at FPA pixel coordinates of (79, 66). Relative to the center of the FPA located at (64, 64), the FPA to detector alignment is off by about 15 arcmin in negative elevation and 2 arcmin in positive azimuth. Detector dimensions are defined by the field stop with a reported average FOV size of 1.96 arcmin by 5.10 arcmin.

FPA to Detector coalignment uncertainty is determined by the size of the MIC1 aperture used to generate the source image. The procedure used to align the MIC1 collimator to the detector bore-sight lends some confidence that the detectors are centered in the collimator output spot. Assuming a triangular probability distribution for the location of the detector centroid in the output spot yields an uncertainty of 2.9 arcmin [5]. FPA boresight alignment is summarized in Table 24.

Table 24. FPA Boresight Coalignment

	FPA Boresight Offset (arcmin)	Uncertainty (arcmin)
Elevation (X-Axis)	-15	2.9
Azimuth (Y-Axis)	+2	2.9

5.1.7. Scan Algorithm Test

SOFIE scan algorithm tests were implemented while viewing the sun with the heliostat system shown in Figure 4. The SOFIE steering mirror was moved to scan the sun image across the focal plane, and the position of the solar image as reported by the scan system was monitored. Solar image top edge position is shown as a function of time in Figure 76. Solar image side edge positions are shown in Figure 77. The periodic variations in the plots of solar image side edge position are caused by movement of the heliostat as the sun moves across the sky.

Scan algorithm performance was characterized by analysis of noise in the sun edge position data shown. These results are compiled in Table 25.

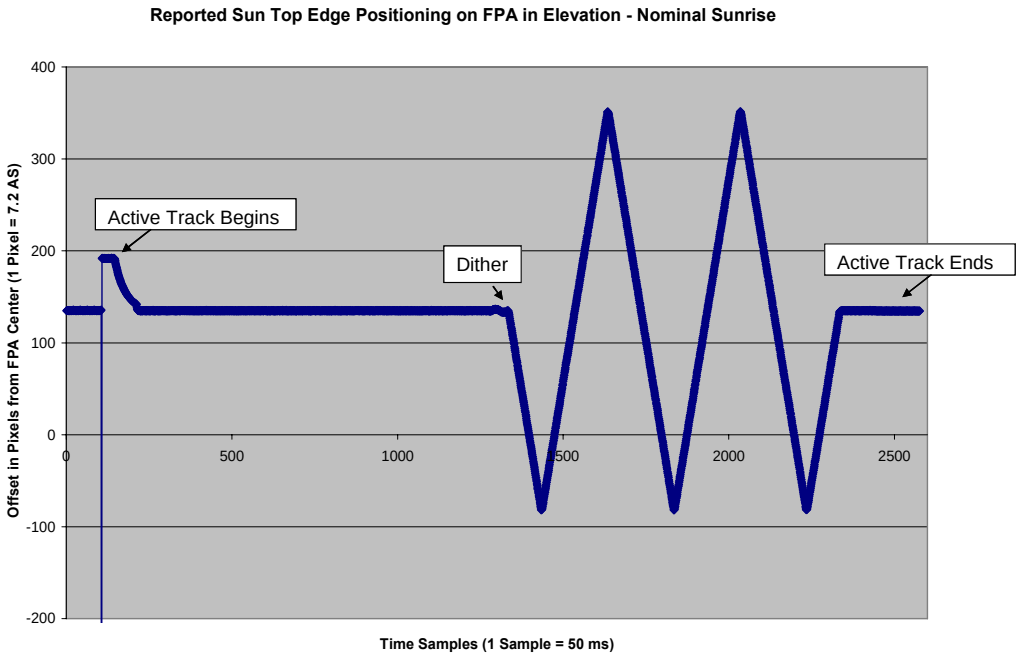

Figure 76. Scan Algorithm Verification - Elevation

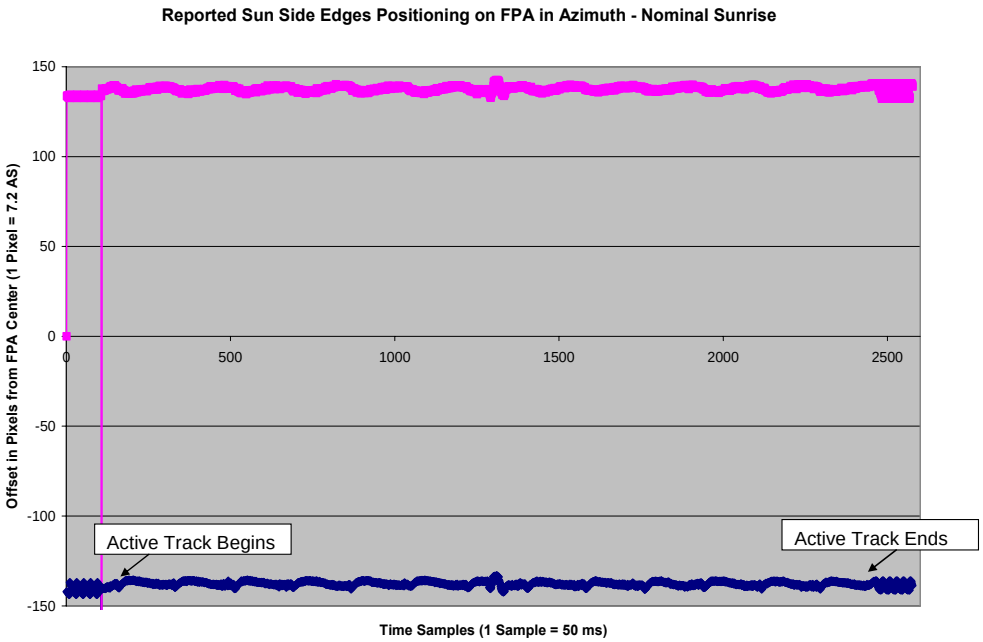

Figure 77. Scan Algorithm Verification - Azimuth

Table 25. Scan Algorithm Summary

Solar Image Position	Noise (pixels)	Noise (arcsec)
Top edge, standard deviation	0.22	1.6
Top edge, 2 Hz running standard deviation	0.053	0.38
Side edge, 2 Hz running standard deviation	0.48	3.5

5.1.8. Gain Characterization

Although SOFIE does not have an absolute radiometric accuracy requirement, SOFIE gain characterization measurements were conducted to verify instrument gain and responsivity specifications. Responsivity characterization measurements were made for each individual spectral band at cold, nominal, and warm science operating temperatures. The SOFIE pointing mirror was held fixed at nominal orientation.

Gain characterization measurements for bands 3 – 16 were performed using the SEBB configuration (see Figure 11). A range of SEBB temperatures were chosen to provide response over as much of the measurement dynamic range as possible. Measurements were acquired both before and after installation of the nonlinearity reduction ND filter. Sample plots from gain characterization measurements after installation of the ND filter are shown in Figure 78 and Figure 79.

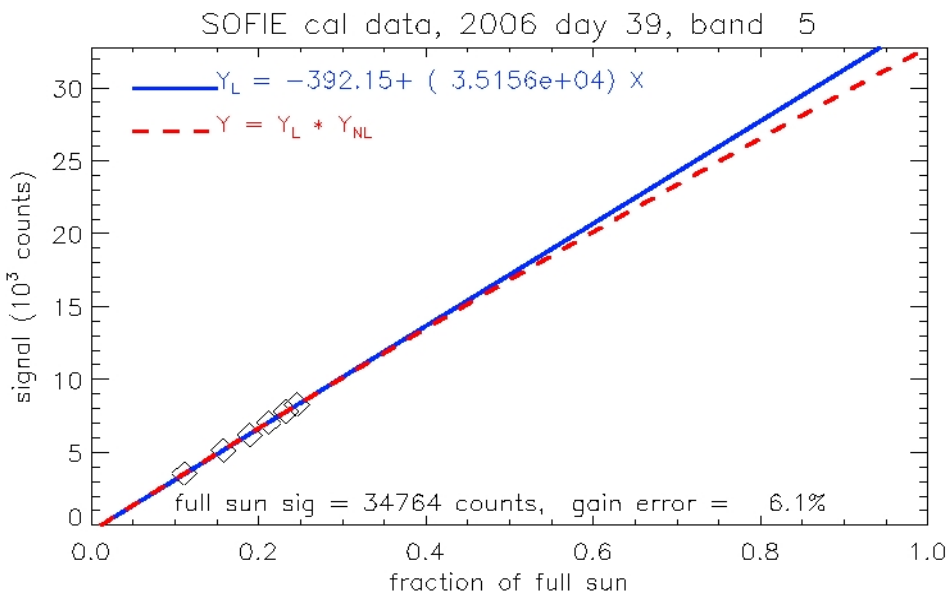

Figure 78. SEBB Response (Band 5)

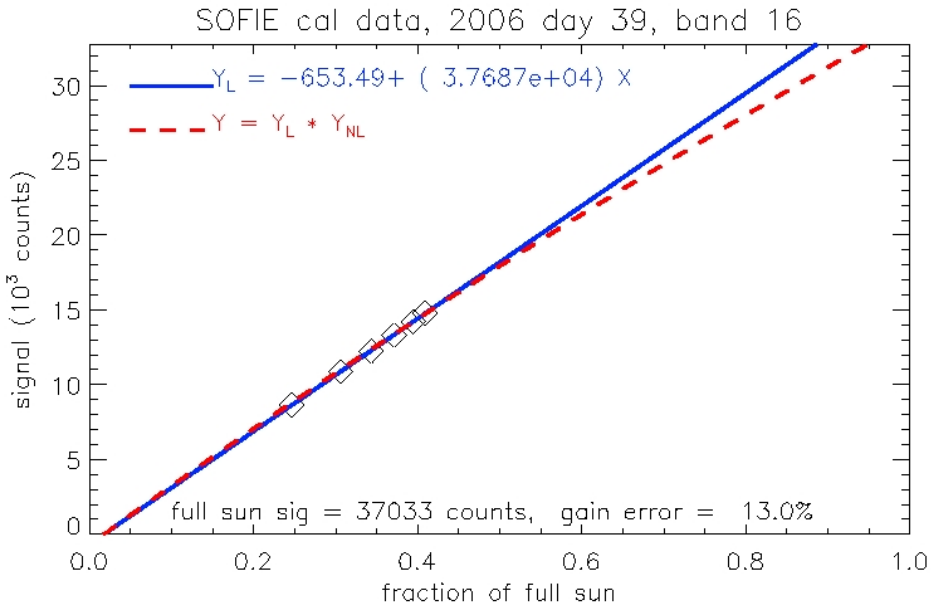

Figure 79. SEBB Response (Band 16)

System gains for bands 1 & 2 were based on solar observations combined with Beer's law analysis of atmospheric transmission. Results from this analysis are shown in Figure 80, demonstrating excellent agreement with theory. Band 1 was unable to observe the sun through the atmosphere, therefore band 1 system gain was extrapolated by analysis from band 2 measurements.

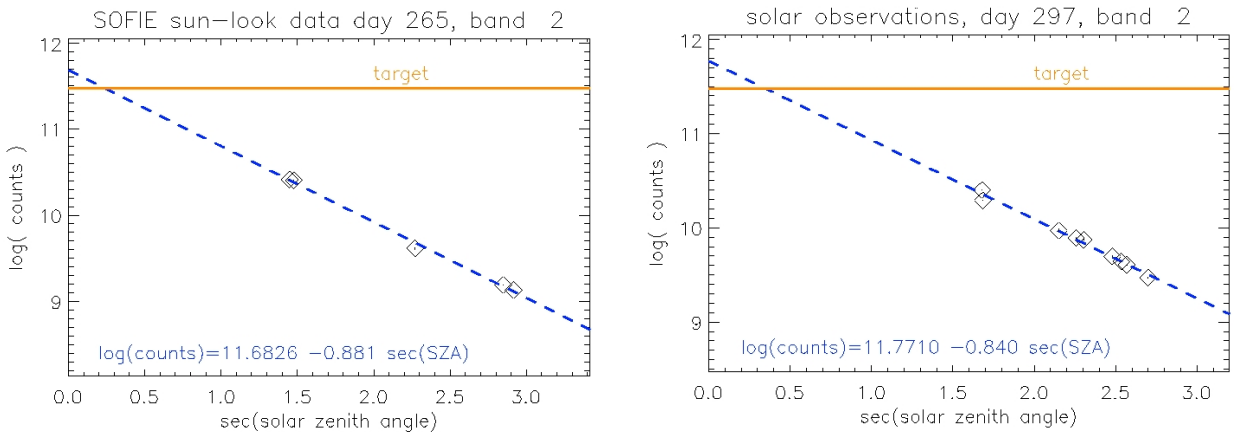

Figure 80. Beer's Law Analysis (Band 2)

Summary data for detector signal gain characterization measurements are shown in Table 26. Anticipated gain errors from this analysis show little or no change following ND filter installation. The errors observed are well within the margin available from balance attenuator adjustment. Final balance attenuator adjustments will be made on orbit to set detector signals and difference signals to requirements.

Difference signal gain characterization results are summarized in Table 27, with gain requirement values shown for comparison. Difference signal gain for each channel is close to the required value, differences from required values are not a concern.

Table 26. Detector Signal Gain Summary

Channel	Band/Target	Gain Error (%) Oct 2005 cold / nom / warm	Gain Error (%) Feb 2006 (days 43 / 39 / 41) cold / nom / warm
1	1 / O_3 s	23% – 34%	no change expected
	2 / O_3 w	23% – 34%	no change expected
2	3 / PMC	-1.1 / -3.2 / -6.1	-6.8 / -4.3 / -3.6
	4 / PMC	7.3 / 4.5 / 1.1	3.0 / 4.8 / 3.9
3	5 / H_2O w	12.5 / 8.5 / 4.4	1.4 / 0.0 / -7.2
	6 / H_2O s	17.6 / 9.4/ 4.5	11.4 / 8.5 / -0.8
4	7 / CO_2 s	-2.5 / -5.9 / -7.5	-9.7 / -10.7 / -14.5
	8 / CO_2 w	1.0 / -2.2 / -2.6	-4.8 / -5.5 / -8.8
5	9 / PMC	11.7 / 9.2 / 6.3	2.6 / 0.9 / -3.1
	10 / PMC	6.7 / 4.4 / 2.6	13.0 / 12.8 / 8.5
6	11 / CH_4 s	7.1 / 4.9 / 2.5	8.6 / 7.7 / 3.8
	12 / CH_4 w	-7.8 / -9.7 / -11.8	-12.1 / -12.2 / -16.1

7	13 / CO_2 s	5.9 / 1.4 / -6.9	2.1 / 1.3 / -3.1
	14 / CO_2 w	8.1 / 2.8 / -4.9	6.7 / 4.9 / -6.8
8	15 / NO w	11.0 / 3.6 / -4.9	10.0 / 6.3 / -7.6
	16 / NO s	11.8 / 4.1 / -4.8	9.2 / 4.8 / -9.4

Table 27. Difference Signal Gain Summary

Chan.	Band / Target	ΔV Gain 7 Feb 2006 (Spec / Measured)
1	**1 / O3 s**	**30 / 39.7**
	2 / O3 w	
2	**3 / PMC**	**300 / 303.4**
	4 / PMC	
3	**5 / H2O w**	**96 / 96.6**
	6 / H2O s	
4	**7 / CO2 s**	**110 / 109.4**
	8 / CO2 w	
5	**9 / PMC**	**120 / 120.0**
	10 / PMC	
6	**11 / CH4 s**	**202 / 202.8**
	12 / CH4 w	
7	**13 / CO2 s**	**110 / 110.3**
	14 / CO2 w	
8	**15 / NO w**	**300 / 297.3**
	16 / NO s	

5.1.9. Stability Characterization

SOFIE stability characterization measurements were performed to understand difference signal drift. These measurements were performed in the MIC1 collimator with SEBB configuration (see Figure 11), while viewing a warm blackbody through an open position in the MIC1 aperture slide. Sample stability characterization time-series plots are shown in Figure 81. Difference signal drift for each channel is shown in Table 28, in terms of counts per minute, and in terms of limiting noise multiples per minute. Difference signal drift predictions are also shown for comparison.

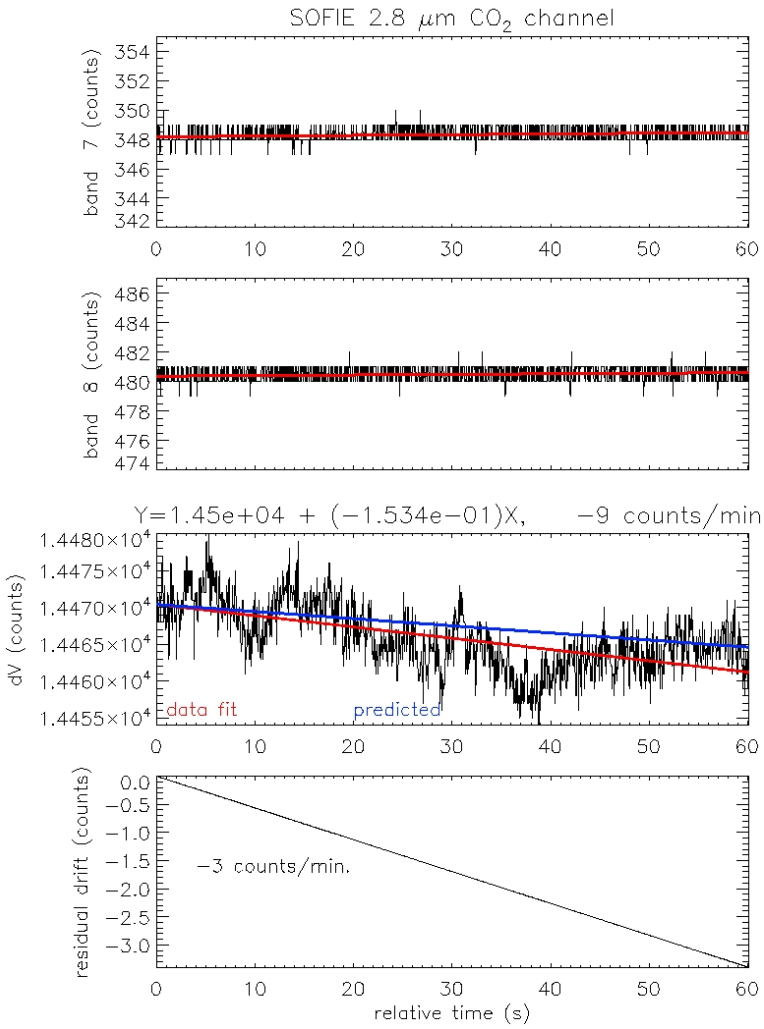

Figure 81. Stability (Channel 4)

Table 28. Difference Signal Stability Summary

Chan.	Band / Target	ΔV Drift (counts minute-1) Measured / predicted	ΔV Drift (noise units s-1) Measured
1	1 / O3 s	-2.5 / -3.9	-2.15
	2 / O3 w		
2	3 / PMC	-1.0 / -41.6	-0.40
	4 / PMC		
3	5 / H2O w	-8.1 / -5.6	-0.08
	6 / H2O s		
4	7 / CO2 s	-9.2 / -5.8	-1.01
	8 / CO2 w		
5	9 / PMC	-10.5 / -16.2	-0.35
	10 / PMC		
6	11 / CH4 s	-9.2 / -36.5	-0.77
	12 / CH4 w		
7	13 / CO2 s	39.5 / 45.0	5.75
	14 / CO2 w		
8	15 / NO w	18.6 / 8.3	0.82
	16 / NO s		

5.1.10. Background and Noise Characterization

SOFIE background and noise measurements were performed to understand system signal-to-noise ratio (SNR) and background offset. These measurements were performed in the MIC1 collimator with SEBB configuration (see Figure 11), while viewing a closed position in the MIC1 aperture slide. Sample background signal time-series plots are shown in Figure 82. System background given by average response under these conditions is shown in Table 29, for tests prior to and following installation of the system ND filter. Difference signal SNR is shown in Table 30, in terms of SNR margin, given by

$$M_{SNR} = (2^{15} \times G_{\Delta V} / \sigma_{\Delta V}) / SNR_{Req} \quad (16)$$

where

M_{SNR} = SNR margin

$G_{\Delta V}$ = difference signal gain

$\sigma_{\Delta V}$ = background signal standard deviation (noise)

SNR_{Req} = SNR requirement

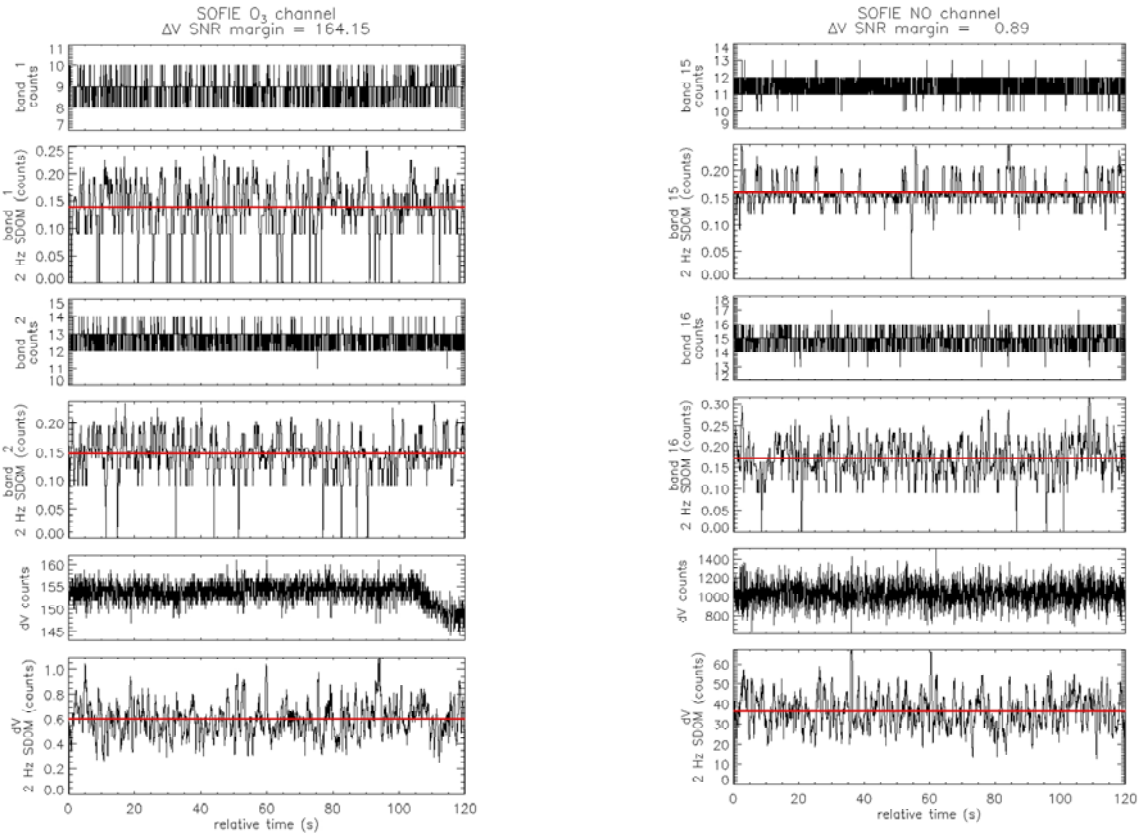

Figure 82. Background Signal Time-Series

Table 29. Background Summary

Channel	Band / Target	Background (counts)	
		October 2005 (Nominal)	Feb 2006 (Cold / nominal / hot)
1	1 / O3 s	11.3	8.9 / 2.4 / 10.9
	2 / O3 w	11.6	12.8 / 12.5 / 14.0
2	3 / PMC	16.2	16.0 / 16.0 / 17.2
	4 / PMC	14.0	13.3 / 13.5 / 15.0
3	5 / H2O w	17.6	16.6 / 17.0 / 18.7
	6 / H2O s	17.0	16.1 / 16.3 / 17.6
4	7 / CO2 s	17.7	17.6 / 17.6 / 18.8
	8 / CO2 w	16.7	16.3 / 16.4 / 17.7
5	9 / PMC	19.2	18.9 / 19.2 / 20.4
	10 / PMC	18.9	19.0 / 19.0 / 20.1
6	11 / CH4 s	19.0	19.1 / 19.2 / 20.6
	12 / CH4 w	18.8	18.5 / 18.6 / 20.1
7	13 / CO2 s	16.4	14.6 / 15.0 / 16.4
	14 / CO2 w	18.1	15.3 / 15.9 / 17.0
8	15 / NO w	15.2	11.4 / 12.0 / 12.6
	16 / NO s	20.1	14.9 / 15.9 / 15.6

Table 30. SNR Summary

Channel	Band / Target	ΔV SNR Margin	
		Oct 2005 (Nominal)	Feb 2006 (Cold / Nominal / Hot)
1	1 / O3 s	146.2	164.1 / 148.1 / 180.6
	2 / O3 w		
2	3 / PMC	5.2	5.8 / 5.8 / 5.9
	4 / PMC		
3	5 / H2O w	15.7	16.3 / 17.4 / 16.9
	6 / H2O s		
4	7 / CO2 s	1.3	1.0 / 1.4 / 1.3
	8 / CO2 w		
5	9 / PMC	3.0	3.0 / 3.0 / 3.0
	10 / PMC		
6	11 / CH4 s	1.2	1.3 / 1.3 / 1.3
	12 / CH4 w		
7	13 / CO2 s	1.5	1.7 / 1.7 / 1.8
	14 / CO2 w		
8	15 / NO w	0.9	0.9 / 0.9 / 1.0
	16 / NO s		

5.1.11. Temporal Response Characterization

SOFIE temporal response characterization measurements were conducted to understand instrument response within the limits of the SOFIE data sample rate. Temporal response characterization measurements were performed in the MIC1 collimator with SEBB configuration (see Figure 11). The SOFIE instrument observed the SEBB through an open MIC1 aperture-slide position, so that the SOFIE detectors were overfilled, while a step-function change in detector illumination was produced. Two methods of interrupting the detector illumination were tried. In the first the SOFIE pointing mirror was held fixed at nominal orientation and a knife edge (solid plate) was dropped in front of the SEBB aperture, and in the second, the SOFIE pointing mirror was moved to interrupt the illumination reaching the detectors.

Detector signal data were processed to remove sample order offset (detector channels are sampled at 12.5 millisecond intervals) and peak normalized. Sample temporal response profiles using

knife edge data are shown in Figure 83, while response profiles using SMA movement data are shown in Figure 84.

Calculated RC time constants for bands 3 – 16 are shown in Table 31. The variations in time constant between test methods, and between detectors, are a result of the uncertainty in illumination step-function position, relative to the 20 Hz SOFIE data sample rate. Within this uncertainty, the temporal response of each band is identical, with a time constant that is less than the 50 millisecond data sample spacing.

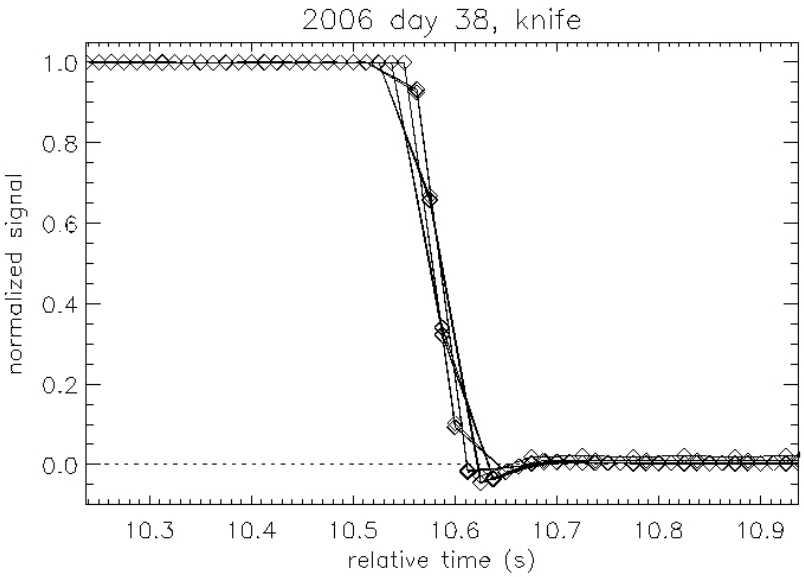

Figure 83. Temporal Response (Dropped Plate)

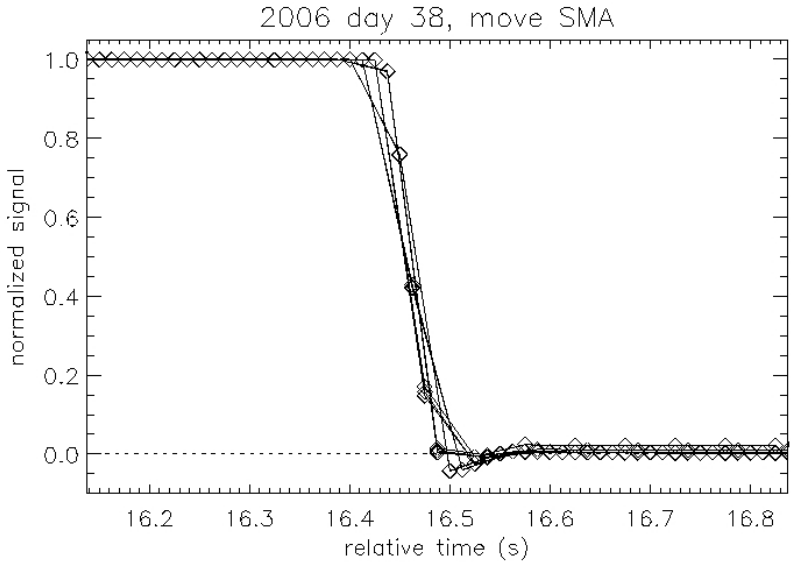

Figure 84. Temporal Response (SMA movement)

Table 31. Temporal Response Summary

Channel	Band / Target	RC Time Constant (ms)	
		SMA Movement	Knife Edge
1	1 / O3 s		
	2 / O3 w		
2	3 / PMC	22	52
	4 / PMC	67	26
3	5 / H2O w	56	19
	6 / H2O s	30	65
4	7 / CO2 s	20	51
	8 / CO2 w	66	26
5	9 / PMC	56	19
	10 / PMC	29	64
6	11 / CH4 s	20	50
	12 / CH4 w	66	25
7	13 / CO2 s	56	19
	14 / CO2 w	29	64
8	15 / NO w	20	50
	16 / NO s	66	25

6. REFERENCES

1. SDL/04-113, SOFIE Specification and Verification Database.
2. SDL/04-046, SOFIE Integration and Test Plan.
3. SDL/04-052, SOFIE Ground Calibration Plan.
4. Gordley, L, Personal Communication, August 2005.
5. Wyatt, C. L., V. Privalsky, and R. Datla, NIST Handbook 152, 1998.
6. SOC-R1446MP-001-0904, Hemispherical Direction Reflectance (HDR) Measurements on Two (2) SDL Sample Coupons, 2004.
7 . NIST 844/270662-04, Report of Calibration, NIST Test # 39077C, 2004.
8. Kemp, J., E. R. Huppi, and M. Madigan, "Measurements of High Out-of-Band Filter Rejection Characteristics," Proc. of SPIE 1112:433-441, 1989.
9. Peterson, J., Personal Communication (e-mail), March 2005.
10. SDL/05-056, On-Axis Field-Of-View Calibration Data Collection Procedure.
11. SDL/05-057, Off-Axis Field-Of-View Calibration Data Procedure.
12. Theocharous, E., J. Ishii and N. P. Fox, "Absolute linearity measurements on HgCdTe detectors in the infrared region," Applied Optics Vol. 43, No. 21, 4182-4188, July 2004.
13. SDL/05-909, SOFIE Radiometric Transfer Function Non-linearity Response Verification and Characterization Effort from the 1st SOFIE Engineering TVAC and Calibration Campaign.
14. Eppeldauer, G., A. L. Migdall, and C. L. Cromer, Characterization of a high sensitivity composite silicon bolometer, *Metrologia, 30,* 317-320, 1993.